Title
Dynamics in Helium Nanodroplets Induced via Multiphoton Absorption in the XUV and X-ray Regimes

Author
Saladrigas, Catherine A.

Publication Date
2022

Peer reviewed|Thesis/dissertation

Dynamics in Helium Nanodroplets Induced via Multiphoton Absorption in the XUV and X-ray Regimes

By

Catherine A. Saladrigas

A dissertation submitted in partial satisfaction of the

requirements for the degree of

Doctor of Philosophy

in

Chemistry

in the

Graduate Division

of the

University of California, Berkeley

Committee in charge:

Professor Daniel M. Neumark, Chair
Professor Stephen R. Leone
Professor David Attwood

Summer 2022

Dynamics in Helium Nanodroplets Induced via Multiphoton Absorption in the XUV and X-ray Regimes

by

Catherine A. Saladrigas

Abstract

Dynamics in Helium Nanodroplets Induced via Multiphoton Absorption in the XUV and X-ray Regimes

by

Catherine A. Saladrigas

Doctor of Philosophy in Chemistry

University of California, Berkeley

Professor Daniel M. Neumark, Chair

Upon formation, helium nanodroplets evaporatively cool to 0.37 K and thus are in a superfluid state. The ultracold droplets have a very low binding energy and are optically transparent. In contrast, when exposed to extreme ultraviolet (XUV) and x-ray radiation, a variety of complex relaxation and disintegration dynamics may ensue. This dissertation explores dynamics induced in droplets via multiphoton absorption in the XUV and x-ray regimes. In the XUV regime, helium droplets become electronically excited, with two broad absorption features originating from atomic helium states. The lower absorption feature at 21.6 eV originates from n=2 atomic helium states, while the upper feature centered at 23.7 eV arises from higher-lying atomic Rydberg states. After single photon absorption, a variety of relaxation mechanisms have been observed, such as ejection of Rydberg atoms, interband relaxation and He_n^* formation. Multiphoton absorption leads to additional deexcitation pathways as a result of interactions between excited helium atoms. At higher photon energies, in the soft x-ray regime, individual atoms in the droplet are ionized via single photon ionization. With high intensity x-ray free electron laser (X-FEL) light sources, droplets can become highly ionized. The ionized droplet may disintegrate from the Coulomb repulsion between ions. Alternatively, if the droplet is sufficiently ionized, the freed electrons are trapped by the collective Coulomb potential of the parent ions, resulting in nanoplasma formation. The quasineutral nanoplasma can then disintegrate via hydrodynamic expansion. The simple electronic structure of atomic helium and uniform density of liquid helium make helium droplets an excellent system for studying complex energy transfer, relaxation, and charging dynamics common to condensed phase media.

Energy transfer and relaxation following multiphoton absorption into the lower, n=2 helium droplet absorption feature is studied by femtosecond time-resolved photoelectron spectroscopy in combination with XUV intensity-dependent ion yield measurements. With many photoexcited helium atoms in the droplet, resonant interatomic Coulombic decay (ICD) emerges as a possible deexcitation mechanism. In ICD, an excited atom relaxes by transferring its energy to a neighboring excited atom, resulting in ionization with freed electron carrying away the excess energy. This process is common in van der Waals clusters and condensed phase media, such as biological systems. Previous experiments have revealed that beyond ICD between two excited atoms, with high excitation densities, ICD can occur between many excited atoms leading to a host

of inelastic processes as well. Here, measurements are performed in a lower XUV intensity regime than previous studies, such that ICD is limited to interactions between two excited atoms. A high-order harmonic pulse at 21.6 eV in the XUV, resonant with the lower droplet absorption feature, is used to electronically excite the droplet. Relaxation dynamics are then measured using a 3.1 eV UV probe pulse at various XUV-UV pump-probe delays. Ion yield measurements reveal a quadratic dependence on the XUV intensity in smaller droplets (~10^4 atoms/droplet) and a linear relationship in larger droplets (~10^6 atoms/droplet). The ICD lifetime is measured to be ~1 ps and found to be a competitive mechanism by which the droplet relaxes, even at low excitation densities.

The charging and disintegration dynamics of helium droplets exposed to intense (~10^{16} W/cm^2), soft x-ray pulses at 838 eV photon energy are explored via single shot coincidence measurements of ion time of flight spectra and small angle x-ray scattering patterns. Experimental conditions encompass an extended range of ionization conditions in droplets, from the pure Coulomb explosion regime to the formation of nanoplasmas. Interpretation of these ionization dynamics is important for better understanding of a host of complex processes initiated by intense x-ray pulse light—matter interactions, both intentionally and as unavoidable byproducts of X-FEL based experiments. Ion time-of-flight spectra are used to determine the maximum ion kinetic energy resulting from the x-ray—droplet interaction, while scattering images encode the droplet size and absolute photon fluence. In correlating the droplet size, x-ray fluence, and maximum ion kinetic energy, a continuous relationship between the degree of ionization and ion kinetic energy is observed across the transition from weakly to strongly ionized droplets. Across all experimental conditions, results indicate that the maximum ion kinetic energy is governed by Coulomb repulsion from unscreened cations. Additionally, the results are consistent with the emergence of a spherical shell of unscreened ions around a quasineutral plasma core with the onset of frustrated ionization by electron trapping. The thickness of this shell is reduced to less than 2% of the droplet radius at the highest degrees of ionization frustration.

Contents

List of Figures

List of Tables

Acknowledgements

I would first like to thank my advisors, Oliver Gessner and Dan Neumark. I am grateful for all the opportunities and support they've both provided during my time at Berkeley. I've benefited greatly from the different approaches they bring to problem solving. Oliver has enabled a variety of opportunities for me to grow as a scientist, from developing the ability to think quickly on my feet under the time pressure of a beamtime to thoughtful and thorough process of analyzing data. Dan has provided valuable insight over the years that has helped me grow as an experimentalist.

I'd like to thank the former and current members of the Gessner group, who I have worked with over the course of my time at LBNL. Camila Bacellar was a great mentor when I was first getting my footing in the lab. Ben Toulson and Mario Borgwardt were great labmates who helped expand my troubleshooting toolbox. It was always a pleasure chatting with Johannes Mahl, whether discussing our respective research projects or the latest show we had watched on Netflix. Felix Brausse was a wonderful office mate. I appreciate our many conversations about data analysis, comparisons of life in Berlin and Berkeley, and adventures in the Bay Area. Matthew Fraund has been a colleague and friend, particularly when there were very few group members due to COVID. I'd like to thank the current group members, Lars Hoffmann, Sahan Neelakanni Mudiyanselage, and Zach Donnellan for group lunches on the patio, insightful research discussions, and coffee breaks as I've worked on this thesis. I'm also grateful for my other colleagues who have worked in Building 2—Kirk Larsen, Richard Thurston, Niranjan Shivaram, Erika Warrick, Yen-Cheng Lin, James Gaynor, and Nicki Puskar. I'd especially like to thank Ashley Fidler for her mentorship and friendship. I appreciate all our conversations about our laser systems, navigating grad school, and Star Wars.

I've also enjoyed the many opportunities I've had to collaborate with Andrey Vilesov and his group both at beamtime experiments and working on papers together. A big thanks to Sean O'Connell for teaching me valuable experimental skills at our first beamtime and for the many shenanigans that made beamtime so fun. It was great when Allie Feinberg joined the team and I've enjoyed working together on data analysis and publications.

It's been a great pleasure to mentor a number of undergrad and post-bac researchers during my time at Berkeley. First, I would like to thank Tahiyat Rahman, for helping me figure out how to be a mentor. Charlie Cummings was both an excellent student and a great labmate. Nathan Helvy and Christian Claudio have been a delight to mentor and work with over the last three years. From a late-night run to Home Depot (and a pitstop at In-N-Out) for an urgently needed puller to our first photoelectron measurements, it has truly been a wild and fulfilling ride to work together. Nathan worked tirelessly in the final mad dash to collect data, both providing assistance in the lab and keeping morale high. I will miss turkey watching at LBL while we waited for the helium droplet source to cool down.

As an undergraduate, I received a lot of support from my research advisor, Bob Field. I am thankful for the opportunities Bob gave me to discover my passion for working in a lab, fostering my creativity, and encouraging me to pursue graduate school. I also learned so much about science, research, grad school and lab skills from the graduate students who were my mentors Jun Jiang and Tim Barnum. They both taught me so much about how fun lab work can be, and perhaps more importantly, how to persevere on the most trying days of grad school.

There are many friends and family who have also supported me throughout my graduate career. First, I'd like to thank my family. My parents, Carrie and Stephen, and my brother, Ethan, have always been incredibly supportive of my dreams and ambitions. I'd like to thank Hannah Kenagy and Trevor Roberts, my first friends in the Chemistry department. From many late nights working on problems sets in the chalkboard room, navigating choosing research groups, and support during the ups and downs of research, your friendship made the challenges of grad school more manageable. Many thanks to my friend Rachael Devlin, for getting me out of the lab to go on hiking and dining adventures around the Bay Area. Last, I'd like to thank my partner, Matt Ware. All his love, encouragement, support, and patience these last few years, especially in the home stretch of grad school, has helped to make this possible.

Chapter 1

Introduction to Helium Nanodroplets

This work focuses on collective effects induced in helium nanodroplets via multiphoton absorption from ultrashort pulses in the extreme ultraviolet and x-ray regime. This chapter will introduce helium nanodroplets and highlight their unique properties, provide an overview of their importance in the literature, and introduce relevant physical mechanisms that will be further explored in chapters 4 and 5. Chapter 2 will introduce theoretical concepts to the experimental techniques utilized to study dynamics of helium droplets. The experimental and data processing methods will be presented in Chapter 3. In Chapter 4, time-resolved results are discussed in the study of interatomic Coulombic decay as an efficient relaxation mechanism following the excitation of multiple atoms in the droplet. Last, Chapter 5 will discuss results of charge dynamics in helium droplets exposed to intense ultrashort x-ray pulses, in which the transition from a Coulomb explosion to nanoplasma formation and hydrodynamic expansion is explored.

1.1 Helium Nanodroplets

1.1.1 Noble Gas Clusters

Noble gas clusters, weakly bound aggregates of noble gas atoms, exhibit both gas phase and condensed phase properties [1]. As such, noble gas clusters serve as an excellent bridge between atomic systems, which are comparably well understood, and condensed phase systems, which are an active area of interest. Due to the full valence shells of its constituents, these clusters are held together by weak van der Waals forces and have very low chemical reactivity. Inherently, they are finite systems. Their size distribution can be carefully controlled to transition between a regime where gas phase properties dominate into a bulk phase regime. Modelling the complexity of hundreds to billions of atoms and the resulting many electron interactions provides an interesting ongoing theoretical challenge. Helium droplets, a special case of noble gas clusters, are the focus of this work. The unique properties of helium have interesting consequences and can in some instances simplify the interpretation of experimental results.

1.1.2 Helium Nanodroplets

Atomic helium, with a closed shell structure composed of two *s* electrons, has the highest atomic ionization potential, a small radius, an extremely small polarizability, and weak interatomic interactions. Helium has a relatively large thermal deBroglie wavelength

$$\lambda_{td} = h/\sqrt{2\pi m k_b T}, \tag{1.1}$$

for Plancks constant, h, mass of helium, m, Boltzmann constant k_b, and temperature T, especially with respect to the closest distance between particles. For example, at 0.4 K, the average separation between any two atoms in bulk liquid helium is 3.6 Å, while the $\lambda_{td} \sim 14$ Å. As a result of this

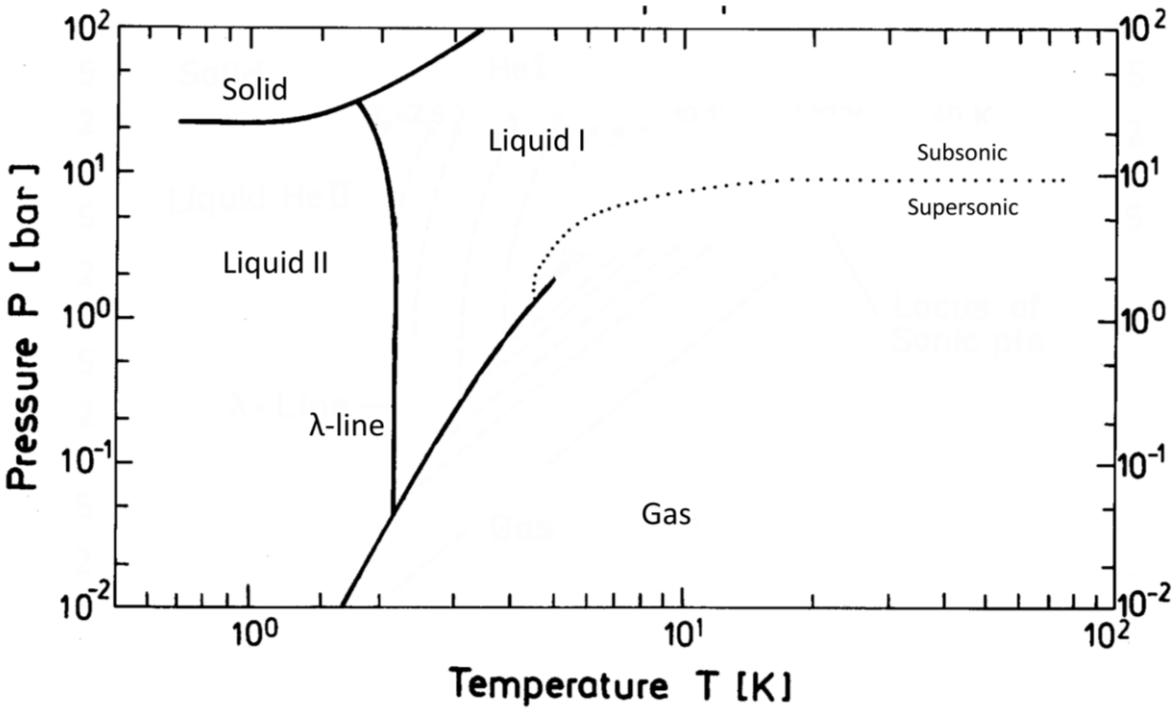

Figure 1.1. ^{4}Helium phase diagram. Adapted from [39]

long wavelength and its zero-point motion, it does not freeze at normal pressures, as is displayed in Figure 1.1 [2]. Instead, as helium is cooled below the so called λ-point, it undergoes a transition into a superfluid phase [3]. Thus, helium has properties distinct from other noble gases from its electronic simplicity and unique phase diagram. Helium has only two stable isotopes, ^{4}He and ^{3}He, with a substantially higher abundance of ^{4}He (99.9998 %). Unique differences arise from the bosonic nature of ^{4}He vs the fermionic natures of ^{3}He, however, unless otherwise specified, all helium droplet work presented here is assumed to be ^{4}He.

Helium droplets, as well as other noble gas clusters, are formed by expanding high pressure gas through a small, cold nozzle into vacuum [4]. Uniquely, due to the extremely low binding energy of helium, all ^{4}He droplets—regardless of size—evaporatively cool to 0.37 K, below the 2.17 K transition to the superfluid phase [5]. As such, they are one of the smallest manifestations of superfluidity and can be described as a macroscopic quantum system. This leads to a host of unique angular momentum properties. Above a threshold angular moment, quantum vortices emerge [6], [7]. As a superfluid, helium droplets have a miniscule viscosity and a heat conductivity that exceeds that of copper by a factor of 30 [8], [9]. Sizes can range from ~10's -10^{10} helium atoms per droplet, or nanometers to microns in diameter.

Helium droplets can pick up dopant species, with the probability described by a Poisson distribution [10]. Earlier understanding of doped droplets assumed that heliophilic dopants, which include all closed shell atoms and molecules, that reside in the center of the droplet, while heliophobic species, such as alkali metals, reside on the surface of the droplet leading to dimple-like distortions. Electrons and excited atoms behave uniquely, in that they can form bubbles and exist in a metastable state. In reality, through x-ray imaging measurements, it has been revealed that rotational excitations of the droplets are unavoidable as they are created naturally. Therefore,

closed shell dopants aggregate in the vortices formed in the droplet. Additionally, when heavily doped, the dopant can form filament shaped clusters in the vortices [7], [11].

1.1.3 Absorption in the XUV and X-Ray Regimes

Different regimes of the electromagnetic spectrum can be utilized to give different types of insights into atoms and molecules. Microwaves and infrared radiation probe molecular rotations and vibrations, respectively. The visible and ultraviolet regimes give access to electronic excitations of valence electrons. Moving into the extreme ultraviolet (XUV), photons have sufficient energy to surpass the first ionization potential in atoms and molecules. In the case of atoms, this corresponds to removing a valence electron. In the x-ray regime, in many electron systems, one gains access to core shell electrons. In creating a core shell vacancy via photoexcitation or photoionization, the system can consequently undergo Auger decay, in which a higher lying electron relaxes to fill the vacancy and another electron is ejected to carry away the excess energy.

Helium droplets are optically transparent, not interacting with light below ~20 eV. In contrast, in the XUV regime, droplets become strongly absorbing, leading to a host of complex relaxation dynamics. Broadly, the droplets have two absorption features between 20 – 25 eV, which were first observed via fluorescence measurements with a tunable synchrotron radiation light source [12]. Because the size of the droplet can be tuned, so can the absorption features. As the droplets increase in size, the absorption features broaden. The lower absorption feature corresponds to the n=2 atomic helium level, which has an absorption cross section of 25 Mb [13]. The upper absorption feature roughly corresponds to higher lying atomic helium states. Figure 1.2 shows the absorption spectrum for droplets with 10^4 atoms and the absorption spectrum of dense gaseous helium for reference. For reference, blue dashed lines in Figure 1.2 correspond to the energy of select Rydberg states in isolated helium atoms. While the lower absorption feature corresponds to photoexcitation in the droplet, interestingly, above 23 eV, in addition to photoexcitation, there is evidence of autoionization, in the form of zero electron kinetic energy (ZEKE) signal [14]. As seen in Figure 1.2, the droplet absorption features are both broad and blue shifted relative to the atomic transitions. This results from repulsion between the excited Rydberg states and the surrounding ground state atoms.

Unlike the XUV regime, atomic helium has no very weak absorption in the x-ray regime and is far from any atomic resonances. By extension, the same is true of helium droplets. At 838 eV, the photon energy used in some of this work, the cross section for single photon ionization is $6\text{x}10^{-4}$ Mb [15] and the probability of double ionization is 3% of that. Because the photon energy is far from any resonances, x-ray absorption in the droplets can be approximated by photoionization of atomic helium. Collective effects arise from the production of many ions in a single droplet. Consequences of this will be discussed below. This weak absorption is in strong contrast to other noble gas clusters, for which the constituent atoms have high cross sections for the ionization of core shell electrons due to the resonances in the soft x-ray regime. Because of the core electron ionization and high absorption cross section, other noble gas clusters become highly ionized both from the x-ray pulse and from the subsequent Auger cascades that follow. The implications of this will be discussed further in section 1.3.

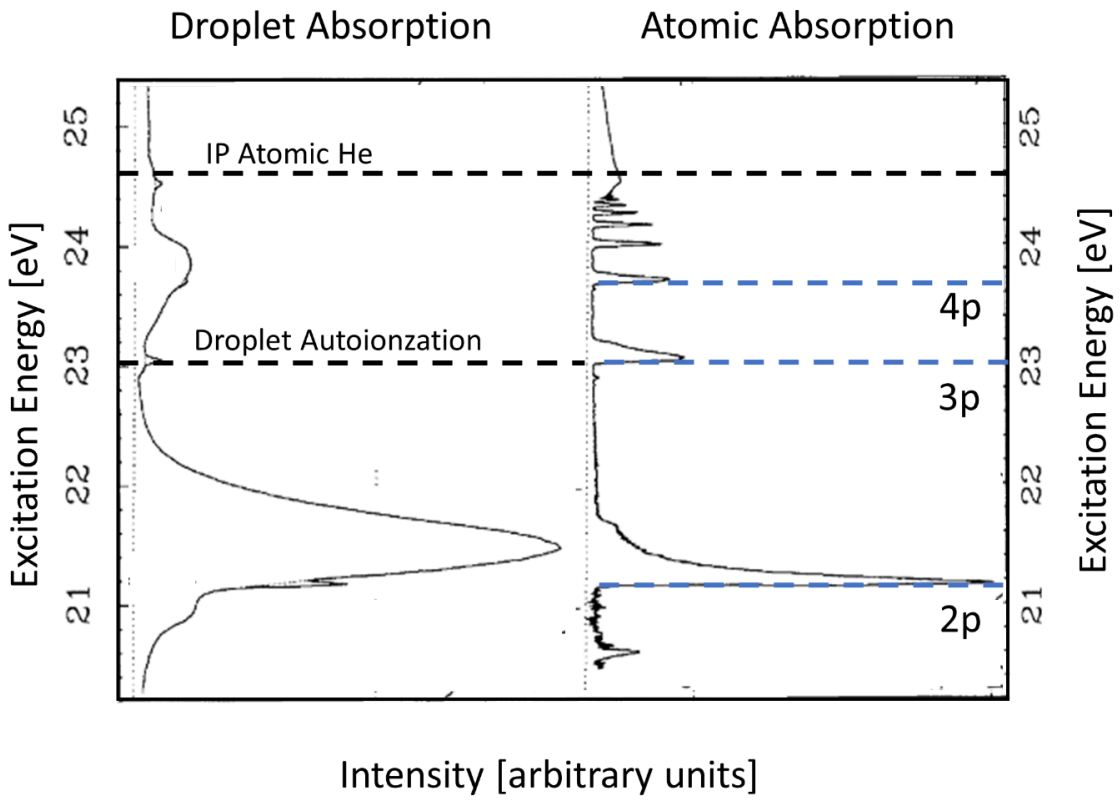

Figure 1.2. The left shows the helium droplet absorption spectrum as measured via fluorescence measurements. This spectrum corresponds to droplets with 10^4 atoms per droplet. On the right, the absorption spectrum of dense gaseous atomic helium is shown for reference, with the energy of key Rydberg states of isolated atoms denoted with blue dashed lines. The atomic helium ionization potential is marked for reference. The threshold for autoionzation is also noted, which correlates with the production of slow electrons. The above figure is modified from [12].

1.1.4 Broader Context for Helium Droplet Research

Helium nanodroplets have a wide range of interesting properties and applications in research [6], [10], [16], [17]. There is a long-standing history utilizing droplets as a spectroscopic matrix due to their ultracold temperature and weak interaction with dopants, in addition to being optically transparent [10]. A recent example is seen in Verma et. al., in which the authors demonstrate a technique for studying ions embedded in helium nanodroplets [18]. Thanks to the high ionization potential of helium, electron impact ionization can be used to form ionic species that are embedded in the droplet. Then, IR spectra are measured for water and Zundel cations ($H_5O_2^+$).

Helium droplets also serve as an excellent environment in which to control dopant atoms and molecules. They have been used as cryogenic nanolabs. Newer work has also leveraged the

droplet environment to spatially align dopant molecules, which is important for maximizing the information content of observables. More specifically, it enables studying the orientational dependence of chemical reactions and in molecular frame measurements it reduces blurring from averaging over randomly oriented molecules. Stapelfeldt's group has demonstrated full 3D molecular alignment by a nonresonant 160 ps laser pulse to align a molecule and a fs pulse to strong field ionize for Coulomb explosion imaging [19]. They find that by aligning the molecule in a helium droplet, they can achieve better alignment than in more traditional techniques of aligning isolated molecules in cold molecular beams. The droplet environment also gives access to large molecules and clusters that would otherwise be hard to form, and the molecular dynamics can be studied in a dissipative environment.

Due to their well-defined density and electronic simplicity of atomic helium, helium droplets make an excellent test system. With the development of single shot coherent diffraction imaging (CDI), helium droplets have been an invaluable tool as they can be used for sample delivery while also acting as a reference x-ray scatterer, to allow for a more straightforward analysis of the recorded diffraction. Single shot x-ray CDI has become a powerful technique developed at free electron lasers, with short pulse durations and a high degree of spatial coherence [20]. In x-ray CDI, short wavelength coherent light is scattered by the object to be imaged and the resulting diffraction pattern is recorded. From the diffraction pattern, assuming the light source is spatially coherent and the wavelength is known, the object can be reconstructed through an iterative algorithm. Reconstruction requires both phase and intensity as a function of position. Although phase information is lost in the 2D diffraction measurement, a variety of algorithms have been developed to reconstruct the images. The general idea consists of providing initial random phases to correspond with the measured intensities, which are then transformed between the object and detector plane via Fourier transforms. While these algorithms do not have a single unique solution, methods can be run with different initial randomized guesses, to find a most common solution, or different solutions can be averaged together.

With helium droplets acting as a medium to contain a sample, a robust and comparably fast technique can be employed to reconstruct the system being imaged, in which the helium can serve as a reference x-ray scatterer [21], [22]. The droplet coherent diffractive imaging (DCDI) technique leverages the known liquid helium density in the droplet as well as it's scattering response, and thus the helium acts as a reference scatterer. CDI is being extended to tabletop high harmonic generation (HHG) sources. Nominal shortcomings of a HHG source for CDI arise from lower pulse energy compared with FELs and the generation of multiple harmonics. Rupp *et al*. have demonstrated the feasibility of implementing a source with sufficient intensity, ~1% of an FEL [23]. By recording scattering images of helium droplets exposed to an HHG XUV source, they developed a scattering analysis that can account for the presence of multiple photon energies, tested on spherical helium droplets. Additionally, they were able to uniquely identify prolate droplet shapes.

Beyond furthering the capabilities of CDI, imaging experiments with droplets have been the interest of many experiments. Multiply charged helium droplets can be used as a physical realization of the Thomson problem [24]. This is the quest to identify configurations of point charges on a sphere that minimize the Coulombic energy. X-ray scattering with charged droplets and Xe as a contrast agent indicate that quasi-free charges form a lattice near the surface, with this first experiment indicating that droplets are a promising venue for studying the unsolved Thomson problem. Furthermore, properties of droplets themselves have been the topic of interest in a number of scattering experiments. DCDI has been an invaluable tool in studying shape and angular

momentum properties in helium droplets [6], [7], [11], [25], [26]. Because dopant species aggregate in quantum vortices if they are present, this technique was used to provide the first direct imaging of quantum vortices in helium droplets [7]. The first direct comparison between angular momentum and shapes of rotating superfluid droplets and classical fluids was performed combining experimental scattering images with theory [25]. This study looked at the interplay of quantum vortices and capillary waves in superfluid droplets, which emulate classical-like shapes. Further studies have compared the aggregation of dopants in bosonic ^{4}He droplets with fermionic ^{3}He droplets, revealing a high degree of spatial confinement within both isotopes resulting from the droplets' rotation, each with distinct morphologies [11]. While ^{4}He has quantum vortices in which the dopants aggregate and form filaments, ^{3}He is devoid of such vortices. Consequently, it is observed that the dopants migrate near the surface, along the equator, as they obtain the same angular velocity as the droplet.

The experiments described above focus on ground state properties of helium droplets. In contrast, the work presented in this thesis explores dynamics in electronically excited or ionized helium nanodroplets. As will be motivated in the following, a variety of complex collective electronic and charging dynamics are initiated by photoabsorption in these shorter wavelength regimes. As was discussed in section 1.1.3, in the XUV regime, photoabsorption leads to electronic excitations. The subsequent relaxation dynamics are heavily influenced by the droplet environment. In the x-ray regime, helium droplets are multiply ionized, leading to collective charging and disintegration effects. Helium droplets in particular make an interesting system for exploring these complex processes, which are relevant to other van der Waals and condensed phase systems, thanks to the electronic simplicity of atomic helium.

Electronic excitations in helium nanodroplets exhibit a variety of complex collective effects and relaxation dynamics, often occurring on ultrashort timescales [17], [27]. Section 1.2 will further describe these collective effects. Recently, a tabletop HHG source was optimized to target the lower absorption feature of the droplets (see Chapter 4). Expanding on the variety of experiments exploring relaxation dynamics following one photon droplet absorption (summarized in section 1.2), time-resolved photoelectron measurements demonstrate that interatomic Coulombic decay (ICD) is a competitive mechanism following multiphoton absorption into the lower droplet absorption feature. ICD is a mechanism in which an excited atom or molecule releases energy by transferring it to a neighboring atom or molecule. ICD is found in a variety of systems, particularly in loosely bound condensed phase media. Results indicate that the ICD occurs with ~ 1 ps lifetime. The results also indicate that not all excited atoms undergo ICD, likely relaxing via the mechanisms found following one photon absorption. Last, complementary ion yield intensity dependent measurements reveal a quadratic relationship between ion yield and intensity in smaller (~10 diameter nm) droplets and a linear relationship in larger (~40 nm diameter) droplets.

Helium droplets, along with other noble gas clusters, also have been of interest in the nanoplasma community. When a cluster is highly ionized by a laser pulse, the ions lead to a Coulomb potential. Below a certain number of ionization events (which will be quantified in section 1.3), the ions explode via a Coulomb explosion. Above this threshold, the Coulomb potential is sufficiently strong, resulting in many of the freed electrons remaining trapped in the cluster, thus creating a quasineutral nanoplasma. Nanoplasmas can either be induced via strong field ionization driven by a NIR pulse or with a high photon flux from an XUV or x-ray light source. With increasing availability of high intensity ultrashort NIR, XUV and x-ray sources, understanding the dynamics of highly ionized systems is easily achieved and is an expanding

experimental field. The evolution of a nanoplasma induced by strong field ionization using an intense NIR pulse was time resolved via single shot x-ray scattering images revealing an anisotropic surface softening and nanoplasma disintegration [28]. Nanoplasma formation in the x-ray regime is appreciably different, particularly in helium nanodroplets. Far from any atomic helium resonances, the degree of ionization is substantially lower, and typical FEL conditions span from weakly ionized droplets in which Coulomb explosion dominates beyond the threshold of nanoplasma formation. This is also distinct from many electron noble gas clusters, which do have resonances in the soft x-ray regime leading to highly ionized nanoplasmas. This results in a relatively straightforward analysis of the degree of ionization and ionic species present. The relationship between ion ejection energy and the degree of ionization in helium droplets has been studied across the transition from a Coulomb explosion regime without any electron trapping into the nanoplasma regime. This will be discussed in greater detail in Chapter 5.

1.2 Relaxation and Energy Transfer Dynamics induced in Helium Droplets via XUV pulses

Electronic excitation into one of the absorption features of a helium droplet has been studied both in the upper and lower absorption features revealing a host of complex relaxation dynamics. The initial excitation is usually assumed to be delocalized across multiple atoms within the droplet, followed by relaxation into isolated excited He* atoms and He_n* excimers. A series of XUV pump – NIR (or UV) probe time-resolved experiments have elucidated a variety of relaxation mechanisms following excitation into the upper absorption feature [29]–[33]. The

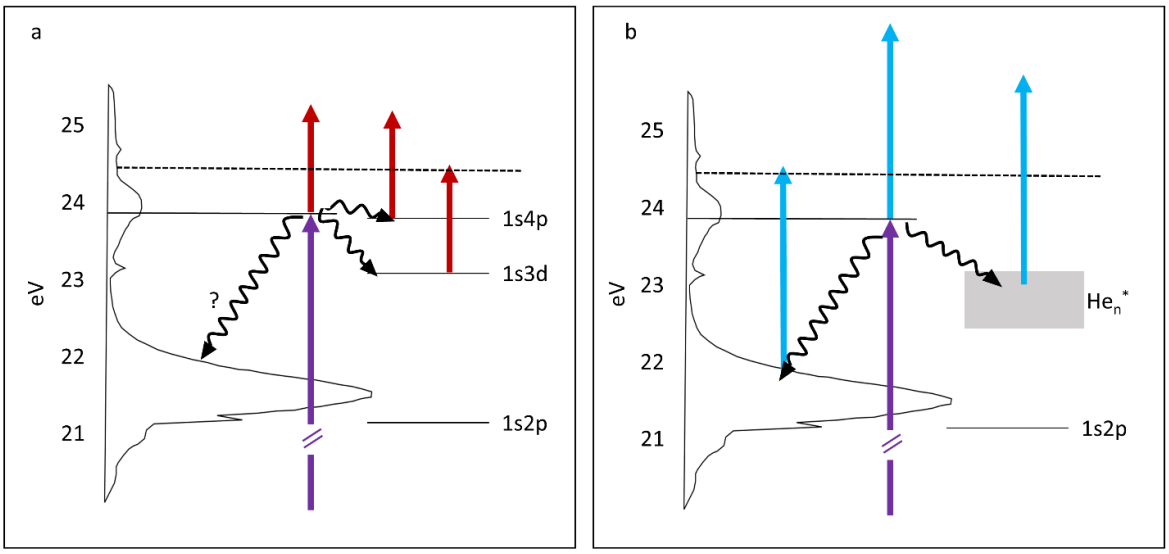

Figure 1.3. A schematic summary of the various relaxation mechanisms following an excitation of the upper absorption feature. Panel a and b show the various relaxation mechanisms that could be elucidated by a NIR and UV probe, respectively. Following a delocalized excitation, near the surface of the droplet, 4p Rydberg atoms are ejected from the outer surface while 3d atoms are ejected from the inner surface region. Excitation can also lead to $He^*_{n\geq 2}$ clusters. Last, the excited droplets can also undergo interband relaxation.

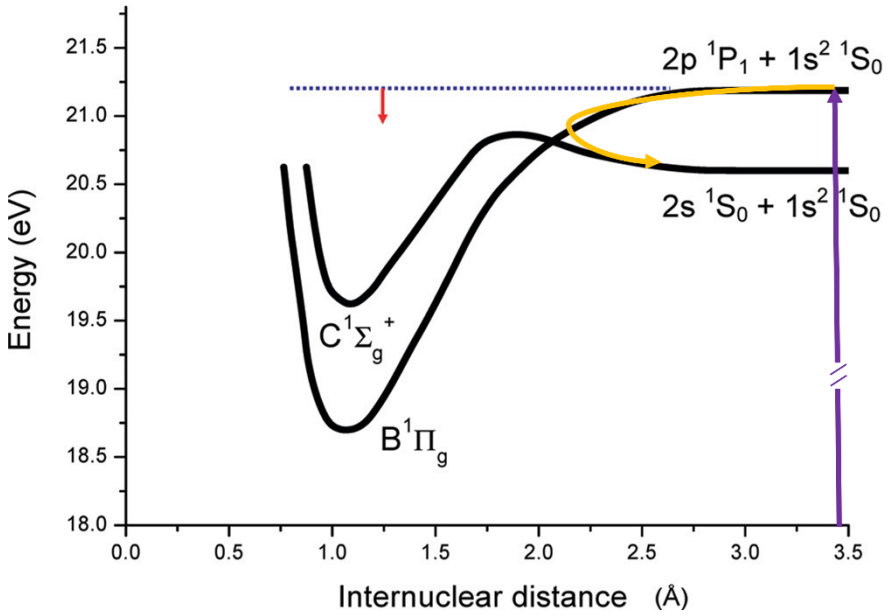

Figure 1.4. Potential energy curves of excimers resulting from n=2 Rydberg states interacting with neutral helium atoms. Following an excitation into the atomic 2p level (denoted in purple) in a helium droplet, the 1s – 2p excimer that results from the proximity of the excited atom with the bulk liquid helium can undergo an ultrafast relaxation to the 1s—2s excimer, (denoted by the yellow arrow). Adapted from [34], [124].

various relaxation mechanisms are summarized in Figure 1.3. Photoelectron imaging with NIR probe pulses reveals a transition from a broad isotropic to sharp anisotropic photoelectron angular distribution corresponding with initial excitation relaxing via ejection of Rydberg atoms near the surface of the droplet. Excited atoms on the outer surface are ejected as 4p excited atoms, as deduced by the prompt emergence and orbital alignment observed in the photoelectron signal. Inner surface excitations lead to the ejection of unaligned 3d excited atoms, which rise in more slowly than the 4p, over 220 fs. Two complementary experiments also give evidence of relaxation from the upper to lower absorption feature, which in fact suggest that the upper absorption feature can be repopulated from the lower feature via a NIR pulse.

Relaxation mechanisms are further studied in the lower absorption feature, as will be the focus of Chapter 4. Through a combination of experimental and theoretical work, it has been revealed that when the excitation energy is in the 2p band, the He* atom undergoes an ultrafast relaxation into the 2s state in less than 250 fs, followed by the formation of a void bubble surrounding the He* in about 0.5 ps. The ultrafast relaxation of 2p to 2s can be explained by considering the potential energy curves of the corresponding 1s-2p and 1s-2s excimers. Prior to the formation of the void bubble, the average interatomic spacing is ~3.6 Å, allowing for excimer character between an excited atom and a neighboring ground state atom. The 1s2p can rapidly relax to the 1s2s via internal conversion through a curve crossing [34], which is pictured in Figure 1.4. Following this ultrafast relaxation, a void bubble begins to form around the He*. If it is sufficiently close to the surface of the droplet, the void collapses and an excited He atom is ejected from the droplet. Alternatively, if the He* is further from the surface, the void bubble can live in

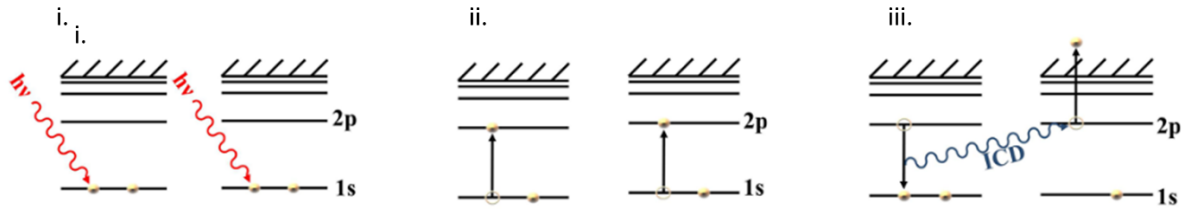

Figure 1.5. An illustration of energy levels involved in interatomic Coulombic decay between two excited helium atoms. In the first step, two helium atoms absorb an XUV photon and are excited to an n=2 level. Then, one of the atoms relaxes back to the ground state and the energy released is transferred to the neighboring excited atom. The result is a ground state helium atom and a helium ion. Adapted from [87]

the droplet on the order of picoseconds. Eventually, the void bubble makes its way to the surface and the excited atom is ejected from the droplet.

In a static frequency domain measurement, it has also been observed that an alternative efficient deexcitation mechanism is present, particularly in smaller droplets, when a dopant species is introduced to the excited droplet environment. Photoelectron spectra were measured of single atom noble gas doped droplets exposed to narrow bandwidth synchrotron radiation tuned to 21.6 eV, centered at the lower droplet absorption feature. In the case of Xe and Kr dopants, whose respective ionization energies (14 and 12 eV) are lower than the excitation energy, the dopant species are indirectly ionized via energy transfer from the droplet to the dopant. This mechanism was observed to be competitive with the 2p to 2s relaxation, with evidence of energy transfer from both states.

Expanding on the previous conditions, the picture becomes more complex in the case of multiple photoabsorption events per droplet. In this case, the possibility of interaction between two excited He atoms leads to another avenue of relation via energy transfer. Although the static photoelectron spectrum between ICD and Penning ionization would look similar, based on the timescales at which this process occurs, it is more likely to be interatomic Coulombic Decay (ICD). In ICD, an excited atom transfers its energy to a neighboring atom, whereby the excited atom relaxes back to its ground state and the neighboring atom is ionized. This can be seen as an interatomic analogue to Auger decay. Often, the neighboring atom is in its ground state. In the case of the droplet, ICD occurs between two excited atoms and is facilitated when two void bubbles merge, thus bringing the excited atoms in close proximity.

In the excited helium droplet, when two excited He* atoms interact, the net result can be a ground state He atom and a He^+ ion in which the electron kinetic energy is equal to the sum of the excited state energy of both atoms, less the ionization potential of helium. A schematic of the ICD, specific to the He* mechanism in droplets, is illustrated in figure 1.5. As the density of He* increases in the droplet, this leads to many excited atom interactions. This has been described as "collective autoionization" (CAI), resulting in lower kinetic energy electrons. There are a variety of steps through which collective autoionization may proceed, described in greater detail in [35]. Briefly, the electron kinetic energy is decreased due to a variety of inelastic processes that become increasingly likely with multiple excited atoms. After autoionization, the free electron may further excite or ionize other nearby excited atoms.

Chapter 4 will describe recent results exploring ICD in helium droplets with relatively few excitations in the droplet compared with previous FEL studies. Using a high harmonic generated XUV pulse to excite the lower absorption feature, the regime in which ICD only occurs between two excited atoms without CAI is studied using femtosecond time-resolved photoelectron spectroscopy and intensity and size dependent ion yield measurements. The combination of these measurements may give insight into the relationship between the initial excitation density and the efficiency of ICD, in particular reflecting the threshold at which ICD may occur. This complements previous works performed with a higher excitation density in the droplet.

1.3 Charging Dynamics induced by Intense X-ray pulses

X-ray free electron lasers have enabled ultrashort and intense x-ray pulses. For many atoms, molecules, and clusters that have relatively high absorption cross sections at these photon energies, the interaction leads to a host of complex ionization and nanoplasma dynamics. Experimental results can prove challenging to interpret theoretically. Helium droplets are an interesting system to study in this regime due to the relatively low absorption cross section and the absence of core electrons. Despite the low absorption cross section, with the high fluence of an FEL, droplets can still achieve a moderate charge state. Conditions span a regime both below and above the threshold for nanoplasma formation, while offering a more straightforward approach to model the underlying physics.

When an intense x-ray pulse interacts with a helium droplet, or any noble gas cluster, initially, the photons vertically ionize the constituent atoms of the cluster, such that electrons are freed with a kinetic energy, $E_{kin,\,e^-}$, equal to the photon energy $h\nu$ less the IP. The freed electrons leave the droplet, and the resulting ions remain. This is referred to as "outer ionization". The remaining ions result in a Coulomb potential in the droplet. After the x-ray pulse has passed, the remaining ion formation then expands via a Coulomb explosion due to the repulsion amongst the ions [36], [37].

If, however, there are a sufficient number of photons for a particular size of droplet, it is possible to create enough ions that lead to a sufficiently strong Coulomb potential so that eventually, the electrons that result from ionization no longer have enough kinetic energy to escape the Coulomb potential of the droplet. These electrons, while free from the parent ions, remain trapped in the droplet. This corresponds to a frustration of outer ionization and is referred to as "inner ionization". With the onset of electron trapping, the charged cluster system begins forming a nanoplasma. The hot, trapped electrons thermalize with the ions, and the nanoplasma expands via a hydrodynamic expansion [38].

When the ions are created, initially they are assumed to be homogeneously distributed. Before the onset of electron trapping, the Coulomb potential experienced by an electron in the charged cluster can be modelled as that of a homogenously charged sphere. The potential is plotted in Figure 1.6a. As can be seen from this figure, at the onset of trapping, electrons tend toward the center of the droplet. On average, each trapped electron screens one ion. Because trapped electrons move towards the center, screening neighboring ions, once ionization is frustrated, the center of the charged system is quasineutral. As such, the system would be better described as hollow charged spherical shell for which the potential is shown in Figure 1.6b.

With the onset of electron trapping, the charged system can be referred to as a nanoplasma. Subsequently, trapped electrons can cause electron impact ionization, increasing the average

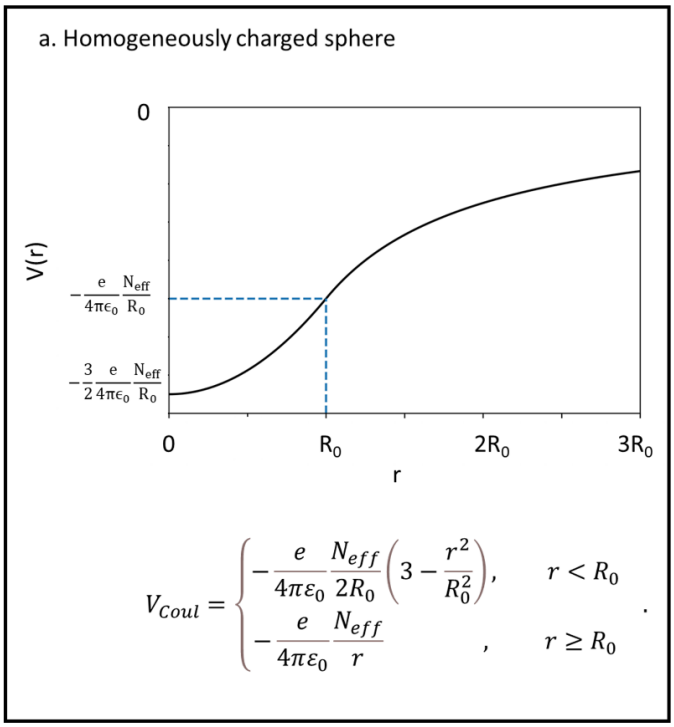

Figure 1.6. a. Coulomb potential of a homogenously charged sphere, with radius R_0 and eN_{eff} charge. b. Coulomb potential of a homogeneously charged spherical shell with a hollow center, for an ion density, ρ_{ion}. and R_{el} as the radius of the hollow center. Note that because ions are assumed to be initially homogeneously distributed in the droplet, the ion density can be simply defined as the number of ions per the droplet volume. Fundamental constants are charge of an electron *e* and permittivity of free space ε_0.

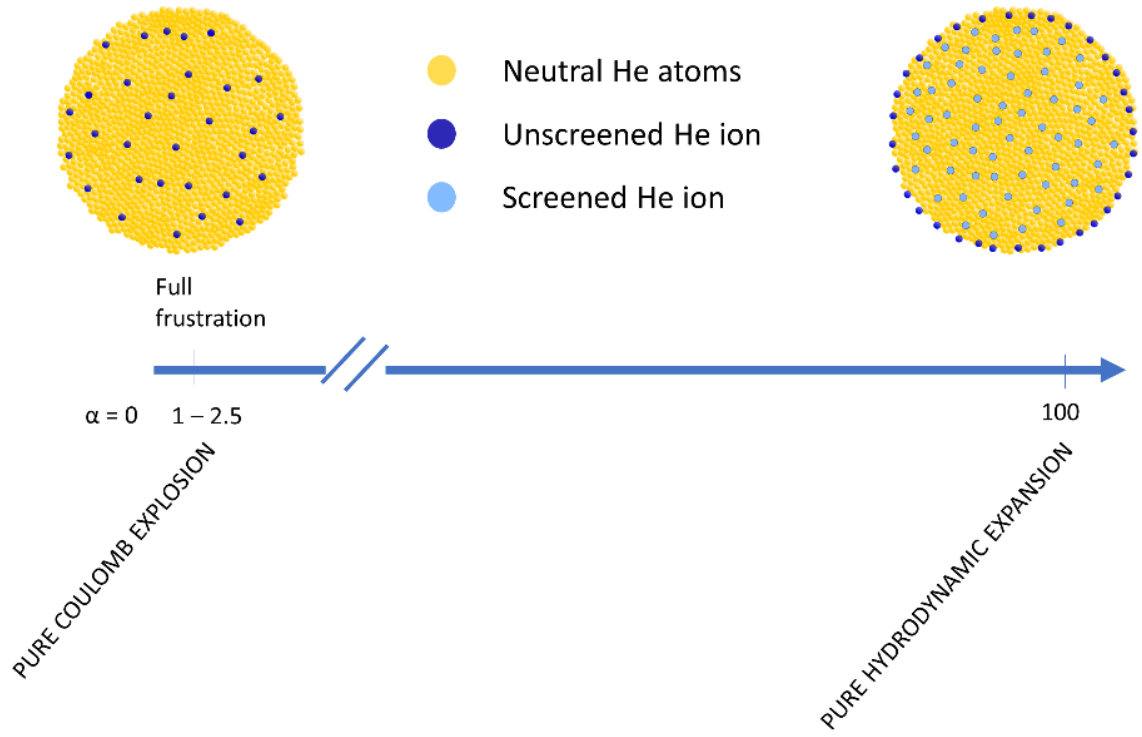

Figure 1.7. Illustration of the relationship between the degree of ionization, quantified by frustration parameter, α, and the expansion regime the charged cluster is expected to undergo.

picture of the nanoplasma quickly becomes very complicated. It can however be both convenient and insightful to quantify the degree of ionization according to the initial conditions imparted by the x-ray pulse and correlate this information with other observables, for instance ion kinetic energy. The initial ionization conditions can be used to learn about the degree of frustration imparted on the system. The degree of frustration depends on both the x-ray fluence (which dictates the number of photoionization events) and the size of the droplet, which influences the Coulomb potential created by the ions. The corresponding so-called frustration parameter, α, is the ratio of the number of ions created via photoionization N_{ion} and the threshold number of ions N_{frust} needed for a cluster of a particular size in order to create a sufficiently strong potential to trap any additionally freed electrons[37]. More specifically, the frustration parameter is defined as:

$$\alpha = \frac{N_{ion}}{N_{frust}} \tag{1.2}$$

N_{frust} corresponds to the number of ions that would need to be created for a sufficiently strong Coulomb potential for frustration, i.e., electron trapping. For this to be satisfied, the Coulomb potential energy, U_{Coul}, would be equal to the electron kinetic energy. The Coulomb energy, for a given droplet radius, R_0, can be related to N_{frust} by:

$$U_{Coul} = E_{kin,\ e-} = \frac{e}{4\pi\varepsilon_0}\frac{e \cdot N_{frust}}{R_0} \tag{1.3}$$

Thus, we can see that N_{frust} can be expressed as $N_{frust} = \frac{4\pi\varepsilon_0}{e^2} E_{kin}(e^-)R_0$. If N_{ion} is less than N_{frust}, for $\alpha \lesssim 1$, this means there are insufficient ionization events for electron trapping and nanoplasma formation and the charged droplet will explode via Coulomb repulsion. In contrast, if N_{ion} is much larger than N_{frust}, for $\alpha \sim 100$, substantial electron trapping is expected, leading to a quasineutral plasma, and hydrodynamic expansion. For $\alpha \sim 1$ (a full discussion of this is provided in Chapter 5), the onset of frustration is achieved and serves as the transition from Coulomb explosion to hydrodynamic expansion regimes. Figure 1.7 is an illustration of the relationship between the frustration parameter and ionization conditions.

In atomic helium, with only two s electrons and no core electrons so to speak, the ionization process is relatively straightforward. In contrast, other noble gas clusters have strong absorption cross sections for core electrons. Not only is the photoionization probability substantially higher, following the creation of a core hole, subsequent ionization occurs in the form of Auger cascades. As such, it is possible to achieve highly charged nanoplasma systems. In large helium droplets exposed to typical FEL pulse intensities of $\sim 10^{16}$ W/cm^2 average droplet charges range from $\sim 10^{-4}$ to $\sim 10^{-3}$, while in other noble gas clusters, typical average charges are greater than 1.

As will be the focus of Chapter 5, the correlation between degree of ionization and maximum ion ejection energy is studied across the transition from a Coulomb explosion regime into the nanoplasma/ hydrodynamic expansion regime. This is achieved by correlating ion time of flight spectra, which contain information about the ion kinetic energies, with x-ray diffraction images, which encode the droplet size and the x-ray pulse fluence, on a shot-by-shot basis. The degree of frustration is quantified according to both the droplet size and the intensity of light to which it is exposed. Results reveal a continuous relationship between degree of frustration and maximum ion kinetic energy, across the transition from a weakly ionized regime into the regime of nanoplasma formation. Results are consistent with a model in which the unscreened ions form a shell around quasineutral nanoplasma core, with decreasing shell thickness as frustration increases.

Chapter 2

Fundamentals of Experimental Techniques

This chapter will present a theoretical basis behind the experimental techniques employed for the experiments described in this work. First, details behind helium droplet generation will be discussed. Then, the working principles behind high-order harmonic generation (HHG) for the production of ultrashort pulses of XUV light and the basic concepts of x-ray Free Electron Lasers (FELs) will be presented. Last, sections 2.3 and 2.4 delve into the various detection schemes for the light—matter interactions employed.

2.1 Helium Droplet Generation

Generally, helium droplets are formed by expanding high pressure helium gas or liquid through a small, cryogenically cooled nozzle, into vacuum. Specific details are presented below. Helium droplets are formed from an adiabatic expansion of the helium along isentropes, with all droplets evaporatively cooling to 0.37 K, well below the so-called lambda transition to the superfluid phase [4], [10], [39].

The droplet size distribution is governed by the nozzle backing pressure, temperature, and aperture size used. There are three different regimes of droplet generation: condensation of gas, fragmentation of liquid, and the Rayleigh break-up of a liquid jet [10]. These three regimes are governed by the initial temperature and pressure, as this dictates whether the droplets are formed starting in the gas phase (subcritical droplet formation) or the liquid phase (supercritical droplet formation). Helium droplets formed from a subcritical regime, i.e., condensation of gas, have a log-normal size distribution. The supercritical regime, i.e., fragmentation of a liquid, results in an exponential size distribution $P(N) = \frac{1}{\langle N_{He} \rangle} e^{N/\langle N_{He} \rangle}$. If droplets are formed via the Rayleigh breakup of liquid helium, a narrow size distribution of large droplets is expected. An overview of the expansion regimes is presented in Figure 2.1, along with the relationship between backing pressure, nozzle temperature and droplet size.

The average droplet size can be tuned according to the nozzle temperature and backing pressure. As the initial helium temperature decreases, the evaporative cooling process becomes less violent, thus resulting in a larger final droplet size. Similarly, the droplet size increases with increasing backing pressure. For the experiment described herein, backing pressures used range from 20-80 bar, nozzle temperatures are between 5.8 and 16 K, and a 5-micron nozzle is used. It is necessary to use 99.9999% high purity helium to prevent contamination of the droplet source, with particular concern for the nozzle. Impurities can freeze, thereby clogging and damaging the nozzle orifice.

Helium droplets can be doped by passing through a cell of dopant gas. Doping depends on the pressure of the dopant gas, the length of the cell, and the size of the droplet. Because doping is determined by collisions between the droplet and the dopant gas, each doping event is independent, and the probability of picking up a dopant can be described by a Poisson distribution.

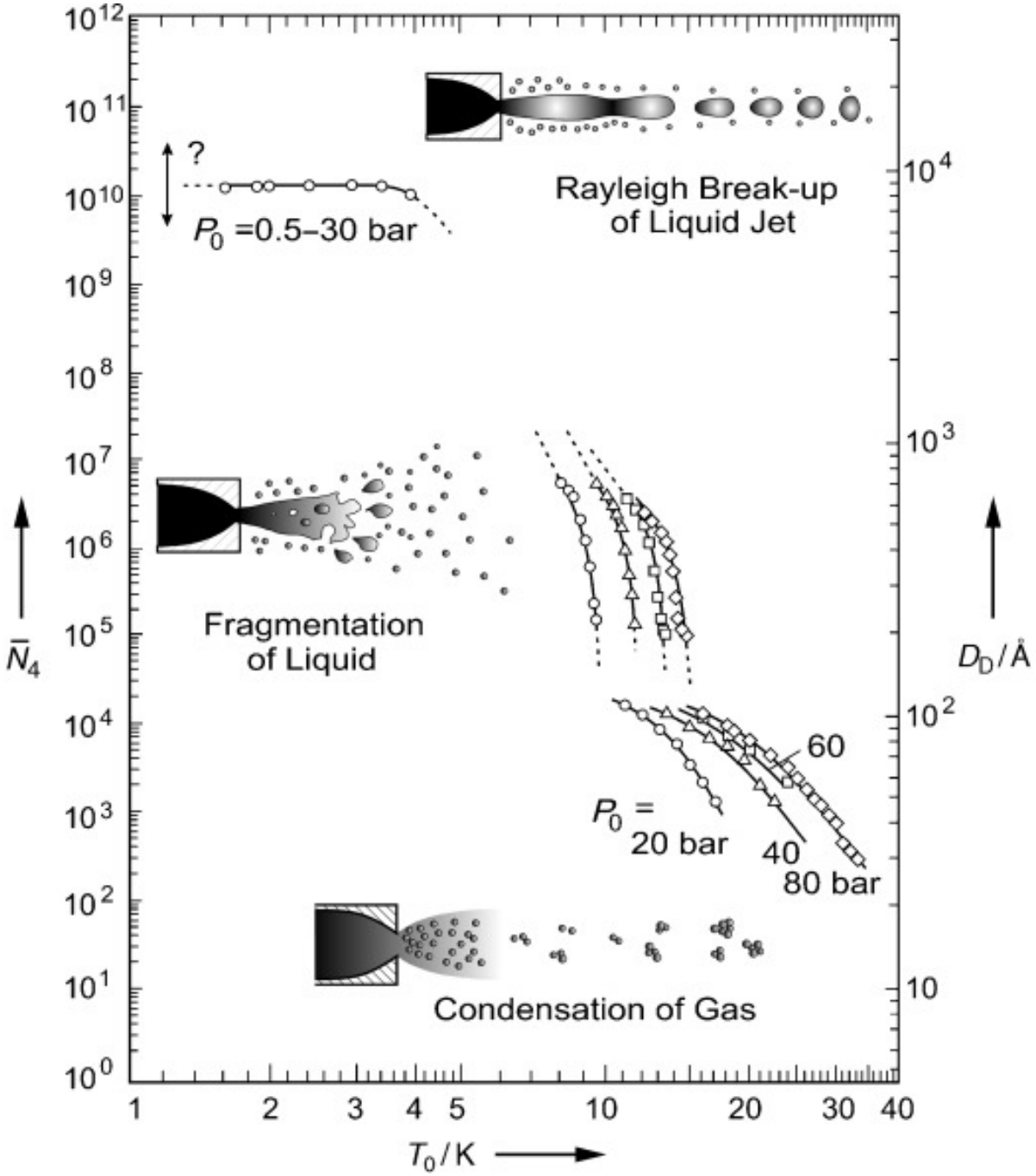

Figure 2.1 This figure provides an overview of the relationship between nozzle temperature, backing pressure, and the resultant expansion regime and average droplet size. Figure reproduced from [10].

2.2 Light Sources

2.2.1 Tabletop light sources

Ultrafast Laser Pulses

Ultrafast lasers refer to lasers with pulse durations in the picosecond to femtosecond regime. Due to the uncertainty relationship between time and frequency, the pulse duration is inversely related to the spectral bandwidth of the pulse if the spectral frequencies are in phase. The relationship of the different frequency components and the resulting temporal profile are illustrated in Figure 2.2. Therefore, a laser medium that supports a large bandwidth is necessary. Ti:Sapphire crystals, with a broad emission around 780 nm, are a very attractive choice for femtosecond systems [40].

Due to the short pulse duration, high peak intensities are easily achieved in ultrafast lasers. In order to amplify to high powers without damaging the lasing medium and other optics in the system, chirped pulse amplification is utilized, a technique pioneered by Donna Strickland and Gérard Mourou [41]–[43], who received the Nobel Prize in Physics for this invention in 2018 (together with Arthur Ashkin who was honored for the invention of optical tweezers). An oscillator generates a low power "seed" pulse, which goes through a pair of gratings that stretch the pulse temporally by introducing a difference in path length as a function of wavelength, so that the different frequency components are separated in time, also known as temporal chirp. The stretched pulse is then amplified by pumping a Ti:Sapphire crystal with an ~532 nm laser and the stretched seed pulse drives stimulated emission. After amplification, the pulse then travels through

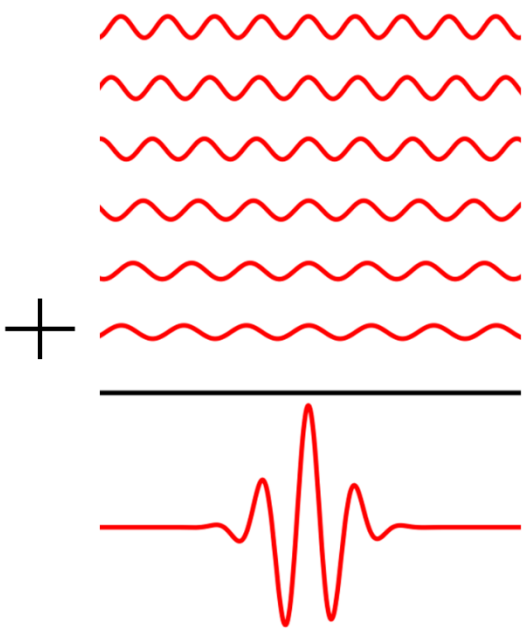

Figure 2.2. Illustration of the superposition of multiple frequencies to obtain a spectrally broad, temporally short pulse.

another set of gratings thatß serve to reverse the effect of the stretcher and temporally recompress the pulse.

The first stage of amplification is achieved either through a multipass amplifier [44] or via a regenerative (regen) amplifier [45], [46]. In both cases, for a given pump pulse, the amplifying seed passes through the crystal ~10 times to maximize the gain from the crystal. In a multipass, multiple trips through the crystal are achieved by physically routing the beam with each trip taking a slightly different path. In a regen amplifier, a mirror cavity with a single beam path is defined and the pulses travel along that beam path, back and forth, making multiple round trips before being released from the cavity. A pair of Pockels cells – a device with an electrooptic crystal – control when light is let into and out of the cavity, by acting as a waveplate to change the polarization. To achieve more amplification, additional stages are configured as single or two pass amplifiers. In this case, typically, the green pump beam and amplified seed travel through the crystal once, or a second pump can be added and the seed travels through the crystal twice, though the number of pump pulses need not necessarily equal the number of passes. As a rule of thumb, this additional amplification can give about a factor of two to three increase in amplification.

Special considerations must be made when working with ultrashort pulses [47], [48]. For one, with ultrashort pulses comes a higher peak intensity. Most unique implications arise from the wide bandwidth of frequencies of which the pulse is composed, in order to achieve the short pulse duration. Because the index of refraction in all materials is frequency dependent, ultrashort pulses undergo dispersion, i.e., the different frequency components travel at different speeds through any medium. This effect is even true in air. However, it is most pronounced in traveling through condensed media, namely, in traveling through transmissive optics (e.g., beam splitters, lenses, nonlinear crystals, waveplates, vacuum windows, etc.). This requires use of thin optics on the order of millimeters or less.

Second Harmonic Generation

A special case of sum frequency generation, second harmonic generation (SHG) is effectively the addition of two photons of the same frequency in a nonlinear medium, resulting in a photon of double the frequency [49]. Nonlinear refers to a nonlinear polarizability response in a medium in response to an electric field. When an electric field, *E(t)* interacts with a medium, it can induce a polarizability *P(t)*, which can be described as a superposition of linear and nonlinear components:

$$P(t) = \epsilon_0\left(\chi^{(1)}E(t) + \chi^{(2)}E(t)^2 + \chi^{(3)}E(t)^3 + \cdots\right). \tag{2.1}$$

In order to support a $\chi^{(2)}$ second order nonlinear susceptibility (and in general all even order terms), which is responsible for SHG, the medium must lack inversion symmetry. When a crystal lacks inversion symmetry, it can support an asymmetric polarization wave, which results from the superposition of the fundamental + second harmonic. The response function of a symmetric medium would inherently only support a symmetric potential. Common choices for nonlinear crystals used in SHG are a beta phase barium borate (β-BBO) and lithium triborate (LBO).

In practice, SHG is not a perfectly efficient process. Because the process is driven by a coherent light source and the resulting second harmonic light is coherently added, it is important to optimize phase matching. Namely, one wants to minimize the phase mismatch, Δk, between the driving light and the second harmonic light, i.e., $\Delta k = k_2 - 2k_1$. Phase mismatch results from a similar origin to dispersion in ultrashort pulses. Due the difference in refractive index of the

fundamental and second harmonic, there is a nonnegligible difference in the refractive index experienced by the two frequencies. This can be circumnavigated by tuning the angle of the crystal to optimize the phase matching. Sensitivity to the angle arises from birefringence in the crystal material, i.e., if the crystal's refractive index is dependent on polarization and the direction of propagation of the beams. Thus, the crystal angle can be adjusted so that the fundamental and second harmonic experience the same index of refraction.

Because this is a second order nonlinear affect, there is also a nonlinear conversion efficiency with respect to the intensity of the driving light. Up to a point, increasing the thickness of the crystal can yield a higher conversion efficiency. However, at some threshold, phase mismatch becomes too great and added length does not help and in fact can decrease efficiency. Additionally, in the case of generating second harmonic with an ultrashort pulse, traveling through an excess of materials can of course have repercussions for pulse duration.

High Harmonic Generation

High harmonic generation (HHG) has revolutionized ultrafast experiments with the creation of ultrashort XUV or x-ray pulses in a tabletop setup. As a short wavelength light source with femtosecond or even attosecond pulse durations, HHG has enabled a new regime of ultrafast studies of electron dynamics in gas phase and condensed phase systems. A description of HHG can be found in many publications [20], [50], [51]. HHG is conventionally a strong field interaction between an intense, short laser pulse and a gas medium, which results in the production of higher order harmonics in the XUV and soft x-ray regime. This has been expanded to generation in condensed phase media, however, this discussion will focus on gas phase HHG. A general setup consists of focusing an ultrashort laser pulse into a noble gas filled cell. The atom–light interaction in gas phase HHG can be described by a three-step model, as outlined in Figure 2.3, though early descriptions explain HHG as a two-step process [52], [53]. Briefly, the strong laser field frees a valence electron via tunnel ionization. The freed electron then propagates in the strong field, gaining kinetic energy. When the field changes direction, the electron is accelerated back towards the parent ion, and with some probability can recombine with the parent ion. This results in the emission of photons with energy equal to the ionization potential (IP) of the atom in addition to the kinetic energy the electron gained as it propagated in the laser field. Because this process can occur every half cycle of the laser pulse t/2 in the temporal domain, the Fourier transform into the frequency domain corresponds to a frequency spacing of 2f. Thus, HHG yields odd order harmonics. At each recollision, bursts of attosecond pulses are generated, leading to an attosecond pulse train. The overall duration is then shorter than the driving pulse, why is typically in the range of ~10's of fs, due to the high intensities that are required to drive HHG. Attosecond pulse generation has been achieved by driving the harmonic process with few-cycle femtosecond pulses. Spatial coherence is controlled by the driving light, as harmonic emission is coherently driven in the forward direction. Temporal coherence, however, is appreciably different for the harmonics than it is for the driving light, as the coherence length is related to wavelength λ and bandwidth $\Delta\lambda$ of the light by $l_{coh} = \lambda^2/2\Delta\lambda$.

Tunnel ionization is one of many possible strong field interactions, depending on the intensity of the driving light. It is useful to define the Keldysh parameter.

$$\gamma = \sqrt{IP/2U_p} \tag{2.2}$$

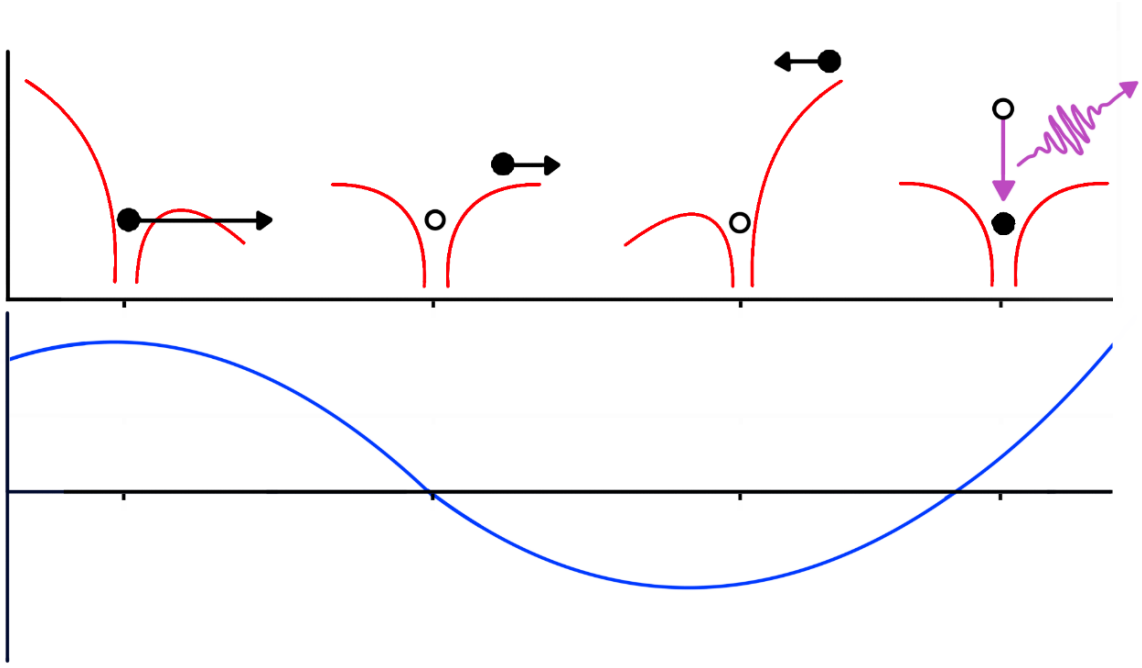

Figure 2.3. A schematic of the three-step model to describe high harmonic generation on the single atom scale. i. electron is freed via tunnel ionization. ii. The electron is accelerated in the laser field. iii. The electron is accelerated back to the parent ion, with recombination resulting in the emission of harmonics.

which gives insight into which regime the strong field interaction falls within. U_p is the ponderomotive potential and can be described as:

$$U_p = e^2 I \lambda^2 / 2\pi c \tag{2.3}$$

The ponderomotive potential describes the cycle averaged oscillatory energy of a free electron in a laser field. The Keldysh parameter gives insight into the ionization regime achieved by the driving light, with $\gamma << 1$ in the strong field ionization regime and $\gamma >> 1$ in the multiphoton ionization regime. In addition to giving insight about the strong field regime, the maximum kinetic energy a freed electron can gain in the high harmonic generation process is related to the ponderomotive potential by the following relationship:

$$h\nu_{max} = IP + 3.17U_p. \tag{2.4}$$

The actual kinetic energy gained corresponds to the birth of the free electron with respect to the phase of the driving laser pulse. If the electron is freed at the peak of the pulse, it will return with zero kinetic energy. If it is born before the peak of the pulse, the electron will not return to recombine with the parent ion. If, however, the electron is born after the peak of the pulse, recombination with a nonzero kinetic energy will occur. The maximum kinetic energy occurs in electrons born at θ = 18 and 198 degrees relative to the fundamental.

From the definition of the maximum photon energy, one can immediately see that a variety of factors can be controlled to affect the high harmonic generation process. For one, the choice of noble gas can affect the cutoff energy. Xenon and krypton, with corresponding IPs of 12 eV and 14 eV, are the natural choice for low order harmonics while helium, with an IP of 24.6 eV is the best option for pushing to a higher cutoff energy. The wavelength of the driving light also impacts the cutoff energy. As such, in efforts to push tabletop HHG sources to the Carbon K-edge, optical parametric amplifiers (OPA's) are used in conjunction with Ti:Sapphire lasers to achieve longer wavelengths for driving the high harmonic process. Conversely, if the goal is to produce discrete, lower order harmonics, one can go to shorter wavelengths. The driving wavelength also affects the efficiency, with longer wavelength sources decreasing the likelihood of recombination and shorter wavelength drivers yielding a higher efficiency. Generally, the HHG efficiency ranges between 10^{-5}-10^{-8} [20]. The efficiency has been found to scale as λ^{-6} for λ= 0.8 - 2μm. For shorter driving wavelengths at λ = 400 nm and 267 nm, the efficiency has been found to surpass a NIR driver [54]. Furthermore, in going to shorter driving wavelengths, one achieves a sparser harmonic spectrum, thus allowing for ease in isolating a single harmonic, as well as a narrower bandwidth. In this work, the second harmonic of a Ti:Sapphire laser is the primary driver for HHG.

Phase matching in HHG requires consideration of additional factors beyond that discussed for SHG. The general description of phase matching of the nth order harmonic can be expressed as $\Delta k = nk_1 - k_n$. In addition to phase matching mismatch from dispersion due to the frequency dependence of the medium's index of refraction, plasma dispersion and geometric dispersion must also be accounted for. Due to the low efficiency of HHG, many of the freed electrons never recombine, thus generating a plasma in the HHG medium. The plasma has a polarizability and refractive index that are frequency dependent. Because the driving light must be focused into the medium used for HHG to achieve sufficiently high intensity, this also contributes to phase mismatch.

The development of high order harmonic generation has enabled a variety of ultrafast experiments in the XUV and soft x-ray regime [55]. The high photon energy gives access to inner shell transitions. In molecules, this enables element specificity in polyatomic dynamics. With few cycle NIR driving pulses and the ability to isolate a single burst of HHG, attosecond dynamics can be monitored in real time. Experiments with HHG sources have been performed to track processes such as avoided crossings and conical intersections in real time [56], [57]. HHG is particularly valuable, as these experiments can be performed in a laboratory setting and do not require large scale user facilities, which are a limited resource.

2.2.2 Free Electron Lasers

The development of XUV and x-ray free electron lasers (FELs) has opened the door for many new experiments due to their short pulses, high power output, and high spatial (transverse) coherence, in addition to their with short wavelengths. This allows for high resolution imaging experiments, in which x-rays are scattered by the object of interest, enabling nanometer-scale spatial resolution due to the short radiation wavelength. The scattered x-rays form a diffraction pattern in the far field, which can be detected, potentially containing enough information to reconstruct the object. Although the FEL pulses are strong enough to destroy the object being imaged, the pulses are also short enough such that phase information from the object is imparted in the scattered light before destruction [58]. High transverse coherence is crucial to achieve high

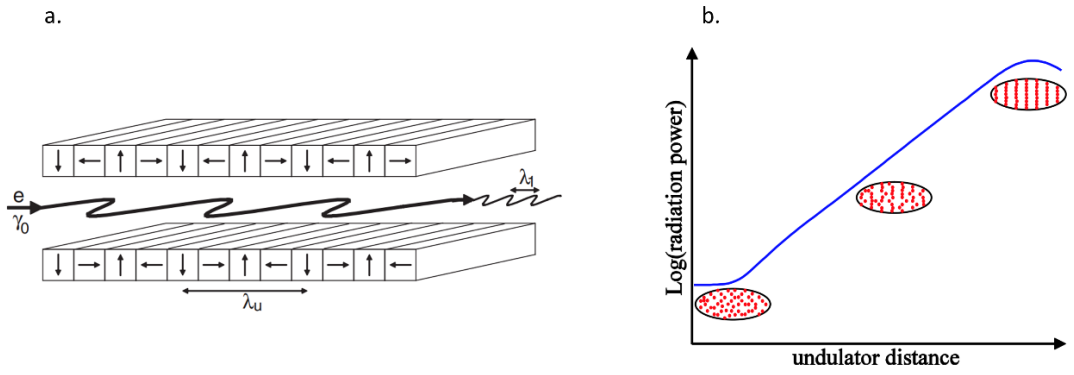

Figure 2.4. a) A schematic of an undulator, which is comprised of a series of magnets. The oscillating electron beam is shown, as well as the emitted radiation. b) the progression of light amplification as a function of undulator distance is sketched in the blue curve. Additionally, the progression of electron microbunching is illustrated in the red bunches. Adapted from [59].

spatial resolution in diffractive imaging experiments because it allows phase information to be extracted from the diffraction images, which is important in the reconstruction process.

FELs build on the undulator technology developed at synchrotron XUV and x-ray light sources, producing shorter, more intense XUV or x-ray pulses with a higher degree of spatial coherence [17], [52]. These light sources make use of radiation emitted from accelerated electrons at relativistic speeds. After electrons are accelerated in a linear accelerator, or linac, the electrons are subjected to undulators, a device composed of a periodic structure of magnets. As electrons travel through the undulator, the magnetic fields force the electrons to oscillate and consequently radiate. An undulator is illustrated in Figure 2.4a. FELs can either be seeded, in which a driving laser is used to impose phase coherence to the electrons [60], or the length (~100 m) of the undulators is utilized to achieve spatial coherence via SASE (self-amplified spontaneous emission) [59]. In the latter case, initially the electrons are random and incoherent. However, as they traverse the undulators, the electrons begin to form microbunches, driven by the radiation they produce as the oscillate. As the electrons become more ordered and the emitted radiation more coherent, the amplification increases from linear to exponential power growth. Eventually, the electrons become fully ordered into a well-defined electron wave, based on the self-amplification from the x-ray radiation, which typically occurs with saturation in power gain. Figure 2.4b is an illustration of the power gain and electron microbunching evolution as they traverse the undulators. Although advances have been made to implement seeded XFELs, giving increased control over the final FEL pulse properties, the FEL utilized for experiment described in this work operated via SASE.

For the purpose of this dissertation, there are a few attractive properties of FELs that are worth discussing. The long undulator path, higher peak current, and finer control of the electron bunches as compared with a synchrotron, which affords the opportunity for microbunching and self-amplification, leads to shorter pulse durations (femtoseconds rather than picoseconds), high peak energies, and improved spatial coherence. Additionally, these light sources are available at short wavelengths. Thanks to the electrons microbunching over the course of the undulators, short x-ray pulses are achieved by the end of the FEL. The short pulse duration enables scattering experiments that reflect the sample structure before the sample is destroyed by the x-rays, the so

called “diffract before destroy” principle. This is particularly powerful in single shot imaging of a replenishing sample, such as an atomic of molecular cluster target or biological systems such as viruses. The high peak power ensures ample photon fluences for these scattering measurements. Additionally, the high fluence and resulting x-ray induced sample “damage” is alternatively a feature for studying x-ray induced nanoplasmas. Even helium droplets, with a low absorption cross section in the soft x-ray regime (~10^{-4} Mb at ~840 eV) can achieve plasma conditions with an FEL source. Last, a high degree of spatial coherence is achieved as a result of the SASE process. The electron microbunching leads to increased coherence in the electrons and consequently increased phase coherence in the emitted radiation. Furthermore, higher order beam modes that may arise from the initial random, statistical electron distribution have less spatial overlap with the main electron beam that forms as the beam becomes increasingly ordered. Therefore, by the end of the undulator, most of the amplified light lies in one spatial mode. Because of the short wavelength radiation achieved by the radiation of the relativistic electrons, imaging experiments have nanometer-scale spatial resolution.

For the discussion of coherence, it is useful to look at the phase space product, i.e., the product of the source size d and the radiation divergence angle θ. For a given source size, there is a lower bound on the divergence angle, depending on the radiation wavelength λ, corresponding to the diffraction limit. In other words, the diffraction limit is defined as:

$$d \cdot \theta = \lambda/2\pi \tag{2.5}$$

Diffraction limited radiation approaches full transverse coherence. To quantify spatial coherence of radiation, a common technique is to perform a series of Young’s double slit experiment, in which the light is sent through a set of slits or apertures, resulting in an interference. These interference patterns can be fit to a product of an airy function and γ, the complex degree of coherence. Upon determining γ as a function of slit separation, the transverse coherence length can be extracted [61]. At the LCLS, the soft x-ray regime approaches the diffraction limit while hard x-rays have a larger phase space than the diffraction limit.

In the above discussion of free electron lasers, key differences in the properties of FELs and synchrotrons are highlighted. It is worth noting that FELs can be considered a complement to synchrotrons. In particular, because synchrotrons can simultaneously support many experiments, they are far more accessible than FELs and thus for measurements that do not need femtosecond pulses, they may be a preferred light source. That being said, FELs have enabled a variety of experimental advantages from single shot imaging, probing atomic and molecular dynamics, cluster physics, and biological studies of systems like viruses and proteins [7], [62]. With the high pulse intensity and short duration, samples that would otherwise be destroyed by continuous exposure to synchrotron sources, can be imaged with a single FEL pulse. The high photon fluence can be used to study multiphoton x-ray absorption in atomic, molecular, and cluster systems [63], [64]. Despite the comparable accessibility of high harmonic sources and the extension into the soft x-ray regime, FELs are a complementary light source with higher pulse energies and energies extending into the hard x-ray regime.

2.3 Photoionization and Photoelectron Spectroscopy

Photoabsorption can either directly or indirectly lead to ionization of an atom or molecule. In the simplest case, if the photon energy hv exceeds the binding energy or ionization potential IP

of an electron, the electron is freed, carrying away the excess energy, E_e- = $h\nu$ - IP. More complex ionization dynamics can arise from autoionization, Auger decays, or ICD. Particularly when studying molecules and clusters, it is also interesting to look at the subsequent ionic species formed and their kinetic energy distributions. A variety of experimental techniques have been developed to characterize photoelectrons and ions [65]. Techniques can encode electron kinetic energy, photoelectron angular distributions, mass-to-charge ratio of ionic species, and ion kinetic energy. Two techniques are used to obtain the results described in chapters 4 and 5. First, ion time of flight spectroscopy will be presented, which provides access to the ionic species present as well as their kinetic energies, followed by velocity map imaging, which is used to study photoelectron energy and angular distributions.

2.3.1 Ion Time of Flight Spectroscopy

In the simplest case of time-of-flight measurements, a voltage difference ΔV is applied across the interaction region to accelerate ions towards the detector followed by a field free drift region of length d. Assuming the ions have zero initial kinetic energy, the time of flight, *t*, through the drift tube can be expressed as:

$$t = \frac{d}{\sqrt{2\Delta V}}\sqrt{\frac{m}{z}} \tag{2.6}$$

Thus, the time-of-flight spectrum encodes the ion mass to charge ratio, *m/z*.

The picture becomes more complex when the ions are born with a nonzero kinetic energy. With a broad distribution of kinetic energies or a given ionic species, there is no longer a one-to-one mapping between *t* and *m/z*. In a Wiley McLaren spectrometer voltages and spectrometer geometry are carefully chosen to ensure that the times of flight have minimal dependence on the starting positions along the flight axis [66]. As a consequence of these conditions, within limits, the time-of-flight differences between ions ejected backwards or forwards relative to those initially at rest scale linearly with the initial ion momenta along the flight axis. Without Wiley McLaren conditions, however, such a clean mapping between time-of-flight and ion kinetic energy is not guaranteed. In fact, it is possible for spectrometer conditions that lead to backwards ejected ions arriving at the detector before ions of the same *m/z* (as is the case for the spectrometer discussed in more detail in Chapters 3 and 5). In this case, for a given ion species, the forward and backward ejected ion time-of-flight distributions overlap, and it is more complex to disentangle the full momentum distribution. Analysis of such spectra can be aided with the use of software to calculate electric fields and the trajectories of charged particles in those fields. By calculating the electric fields based on the spectrometer geometry and voltages used, the time of flight of stationary, forwards ejected, and backwards ejected ions of a given initial kinetic energy can be determined and compared to the measured time-of-flight spectra.

2.3.2 Velocity Map Imaging

Following photoionization, the electrons and ions form a “cloud” of expanding, nested spheres, resulting from the initial distribution of velocities imparted by the photoionization

process. This "cloud" is referred to as a Newton sphere. Velocity Map Imaging (VMI) is an electron or ion momentum imaging technique that preserves the information about the Newton sphere by recording a 2D projection of the Newton sphere on a detector with spatial sensitivity [67]. In other words, all electrons (or ions) of the same initial velocity (and mass) are mapped to the same spatial location on the detector. This concept is demonstrated in Figure 2.5. Imagine photoionization results in two isotropic electron distributions, with different initial kinetic energies. Electrons with a higher kinetic energy (denoted in blue) will radially expand further in time, than the lower kinetic energy distribution (denoted in purple). In order for the 3D distribution to be mapped onto the 2D detector, it is necessary to have cylindrical symmetry about the axis parallel to the detector. Furthermore, VMI proves to be a valuable tool, as the electrostatic optics ensure mapping of all charged species with the same initial momentum to the same point on the detector, regardless of the initial position (within typical interaction volume dimensions), so that the natural spatial distribution of the interaction region does not cause smearing in the recorded images.

To achieve this, a standard VMI spectrometer consists of a repeller, extractor, and ground electrostatic optics followed by a drift region. This leads to a voltage difference across the interaction region from the repeller and extractor, followed by another voltage difference between the extraction and the entrance to the field free region. These are referred to as "optics" because the effects of the plates can be modelled using a transfer matrix, analogous to the transfer matrix formalism used in conventional optics [68]. Nominally, this can be modelled as the product of four transfer matrices corresponding to the approximately uniform field region between the repeller and extractor, the inhomogeneous "kink" in the field at that extractor opening that acts as a lens, the approximately uniform field region between the extractor and ground plate, and lastly from the kink in the field ground plate aperture before the drift tube. In practice, the first region is better approximated by a kinematic equation. The field lines are shown in Figure 2.5 for reference.

In practice, the repeller with voltage V_R controls how large of a kick the Newton sphere receives, thus the time-of-flight t scales as

$$t \propto \frac{1}{\sqrt{V_R}} \sqrt{\frac{m}{z}} \tag{2.7}$$

while the extractor voltage V_E is tuned to ensure the Newton sphere projection focuses on the detector. The ratio V_R/V_E is fixed for a given distance between the interaction region and detector, and the aperture size in the extractor and ground plate on the time-of-flight tube. With higher magnitude voltages, the Newton sphere is given a larger velocity towards the detector and thus has less time to expand in its time of flight, allowing for larger kinetic energies to be measured. In contrast, to "zoom in" on lower kinetic energy features, lower magnitude voltages are used, resulting in more time for the Newton sphere to expand before reaching the detector. The relationship between the radius r of the ring of a given kinetic energy relates to an empirically determined magnification M, the velocity v, and t in the following relation:

$$r = Mvt. \tag{2.8}$$

From this relation, it follows that the kinetic energy scales as r^2 in the recorded VMI images.

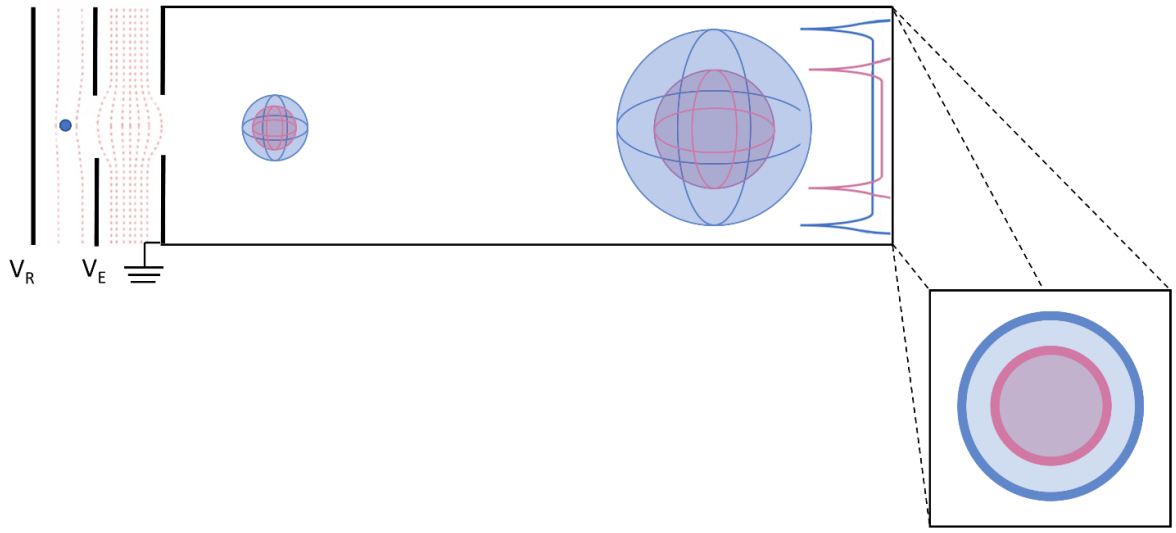

Figure 2.5 Sketch of a VMI spectrometer. Representative field lines are shown in the interaction region. The progression of the Newton sphere is pictured. The blue and purple spherical shells correspond to higher and lower kinetic energy electrons. At the end of the detector is an intensity line out of the projection on the 2D detector from the two kinetic energy distributions and an illustration of the resultant image of the 2D projection.

2.4 X-Ray Scattering

In soft x-ray scattering, x-rays are elastically redirected following interaction with the electrons in the target object. When a plane wave interacts with a medium, oscillations are induced in the electrons due to the polarizability of the medium. These oscillating electrons then radiate resulting in scattered light. A variety of special cases to describe scattering exist. Here, we focus on the Rayleigh-Gans approximation [69]. In this case, the object is "optically thin" or transparent, corresponding to a small object with respect to the radiation wavelength, or an index of refraction similar to the surrounding medium. This has the implication that each volume element can be treated as an individual Rayleigh scatterer.

While this description can be applied to an object of arbitrary shape, herein droplets are applied as spheres, so the criterion for the Rayleigh-Gans approximation is satisfied if:

$$\frac{2R_0|n-1|}{\lambda} \ll 1 \tag{2.9}$$

for a scattering object radius R_0, index of refraction n, and x-ray wavelength λ. The index of refraction for liquid helium at 1.48 nm is $n = 1\text{-}4.32\times10^{-5}\text{+}1.75\times10^{-7}i$. Given that this is close to 1, the index of refraction of vacuum in which experiments are performed, the Rayleigh-Gans approximation is an appropriate treatment for the x-ray scattering images.

With the Rayleigh-Gan approximation, the scattering amplitude for a given angle θ can be expressed as:

$$S(\theta) = \frac{3}{4\pi} k^3 \left(\frac{n^2-1}{n^2+2}\right) \int e^{i(\vec{q} \cdot \vec{d})} dV \tag{2.10}$$

with the x-ray wavevector k, change of wavevector $q = 2k \sin(\theta/2)$, and real space coordinate d. From the scattering amplitude, the intensity of scattered photons can be used to determine the photon fluence F experienced by the droplet in the x-ray focus:

$$I_{total} = \frac{8\pi^3 R_0^4 |n-1|^2}{\lambda^2} F \tag{2.11}$$

The scattering profile can also be used to determine the size of the droplet following the relation:

$$\Delta\Theta \approx \frac{\lambda}{2R_0} \tag{2.12}$$

in which $\Delta\Theta$ is the difference in scattering angles between rings. Thus, in x-ray scattering by a larger droplet corresponds to a closer scattering ring spacing, and conversely smaller droplets have a larger ring spacing.

The work herein focuses on neat helium droplets, relying on the analysis described above to extract droplet size and photon fluence from diffraction images. However, helium droplets can be utilized in single pulse coherent diffractive imaging measurements. In CDI measurements, phase information is lost in the recorded scattering images because intensity is measured, rather than the field. Challenges lie in retrieving a unique solution through iterative Fourier analysis algorithms. However, because helium droplets can be doped, they may serve as a medium to deliver other objects to the x-ray focus, while also serving as a reference scatterer. In particular, measurements have explored doping droplets with Xe which is a many-electron atom, in contrast to He, providing high contrast between the dopant and surrounding liquid environment [7], [21]. Because the Xe aggregates in the vorticities in the droplets, early experiments were used to image the vorticity structure in the droplets.

Chapter 3

Experimental and Data Processing Methods

The helium droplet studies described herein were performed with two different experimental setups. Helium droplet dynamics in the XUV regime are studied with a tabletop high harmonic generation (HHG) source at LBNL. Charging dynamics in helium droplets induced in the x-ray regime are studied using the free electron laser—Linac Coherent Light Source (LSLC)—at SLAC National Accelerator Laboratory. This chapter describes in detail each experimental setup and general methods for analysis.

3.1 LBNL Lab

An overview of the lab based experimental apparatus is presented in Figure 3.1. Following a brief description, further details will be presented in sections 3.1.1 – 3.1.6. Attached to the main

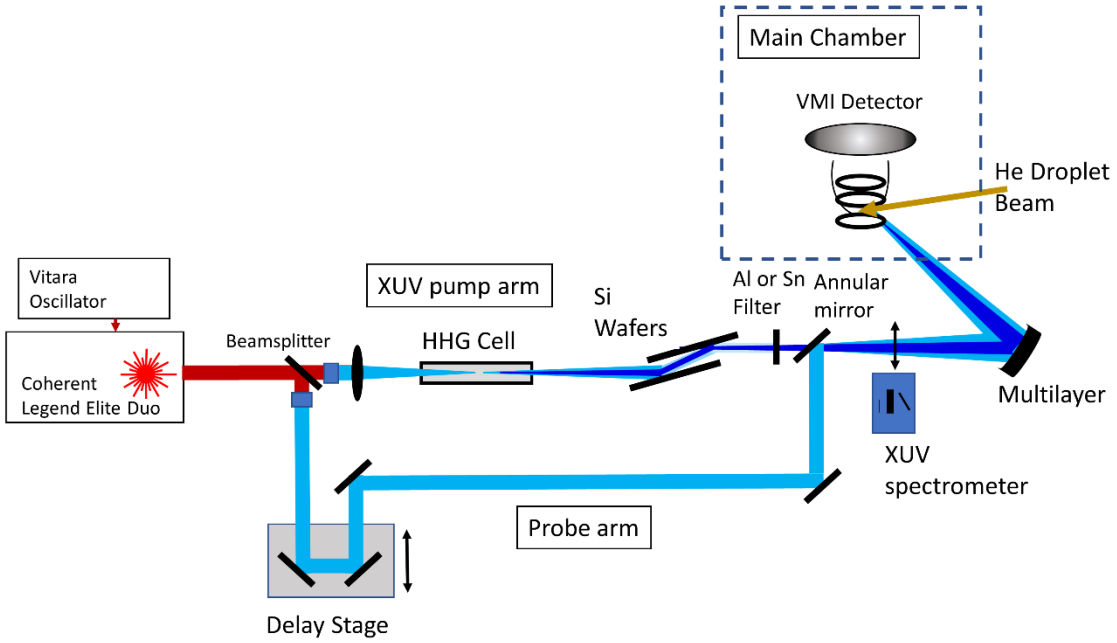

Figure 3.1. Experimental overview. A Ti:Sapphire laser beam is split into a pump arm (which is used to generate XUV) and a probe arm (which is used to generate 402 nm light). The pump and probe are recombined after the probe is routed over a delay stage and focused into the interaction region. There, they intersect the helium droplet jet. Photoelectrons are detected via a velocity map imaging spectrometer.

interaction vacuum chamber is a continuous helium droplet source, capable of producing droplets up to 10^8 atoms. From a Ti:Sapphire femtosecond laser system, ~6 mJ of 40 fs NIR light is used. A beam splitter is used to split the light into a "pump" and a "probe" arm for time-resolved experiments. The majority is used to drive HHG. The resulting XUV pulse serves as a pump to initiate dynamics in helium droplets. The rest of the light is used as a probe (either 800 nm or 400 nm). The probe beam is routed to a delay stage, which is used to control the time delay between the pump and probe with fs resolution. The pump and probe are then recombined using an annular, or "holey mirror". The two beams are focused using a spherical multilayer mirror into the interaction region where they intersect the helium droplet jet. The interaction region is centered between repeller and extractor ion optics of a velocity map imaging (VMI) spectrometer, which can measure electrons or cations, depending on the polarity of voltages used. Surrounding the interaction region is a liquid nitrogen cold trap that reduces the ambient vacuum chamber pressure and therefore lowers the background signal. For time-resolved data acquisition, at each pump-probe time delay, a VMI image is recorded with the XUV pump only, and with XUV pump + UV probe. The XUV only image can be used for background subtraction or normalization, which can account for long-term drifts in the experimental setup. Typical image acquisition times range from 30 – 120 seconds.

3.1.1 Helium Droplet Source

The helium droplet source used in the laser lab at LBNL was designed by Darcy Peterka and is described in detail in his dissertation [70]. The helium source, which can support up to 80 bar as a backing pressure, is precooled with liquid nitrogen lines. The helium travels from high pressure into vacuum through a cryogenically cooled 5 μm diameter nozzle. This nozzle consists of a platinum aperture that is sandwiched in a copper housing and is sealed with a gold gasket. It is cooled by a closed loop liquid helium compressor with temperatures as low 13.5 K achieved herein. The helium expands through the nozzle into a chamber with a base pressure ~10^{-8} Torr with the liquid nitrogen cold trap. However, when in operation, the chamber base pressure can reach 4x10^{-4} Torr, depending on the size of the droplets. The droplet jet passes through two 2 mm

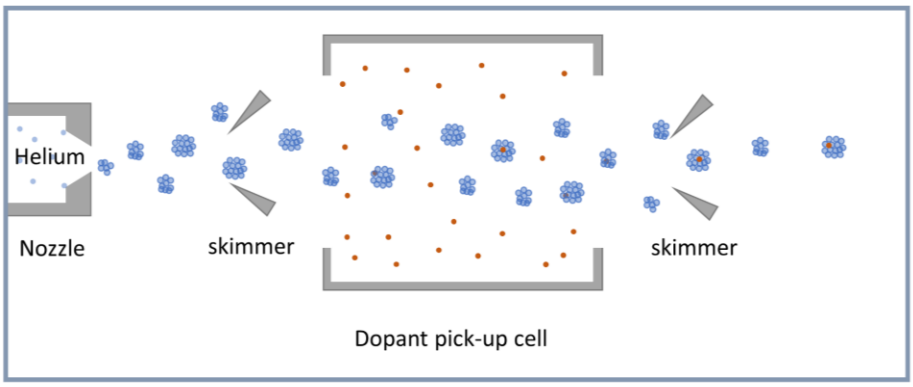

Figure 3.2. Schematic of helium droplet generation. Following the expansion of the cooled helium into vacuum, the droplets that form pass through a pair of skimmers to select for a collimated beam of droplets. In between the two skimmers is a pick-up cell which can be filled with a gaseous dopant species, for the purpose of doping droplets.

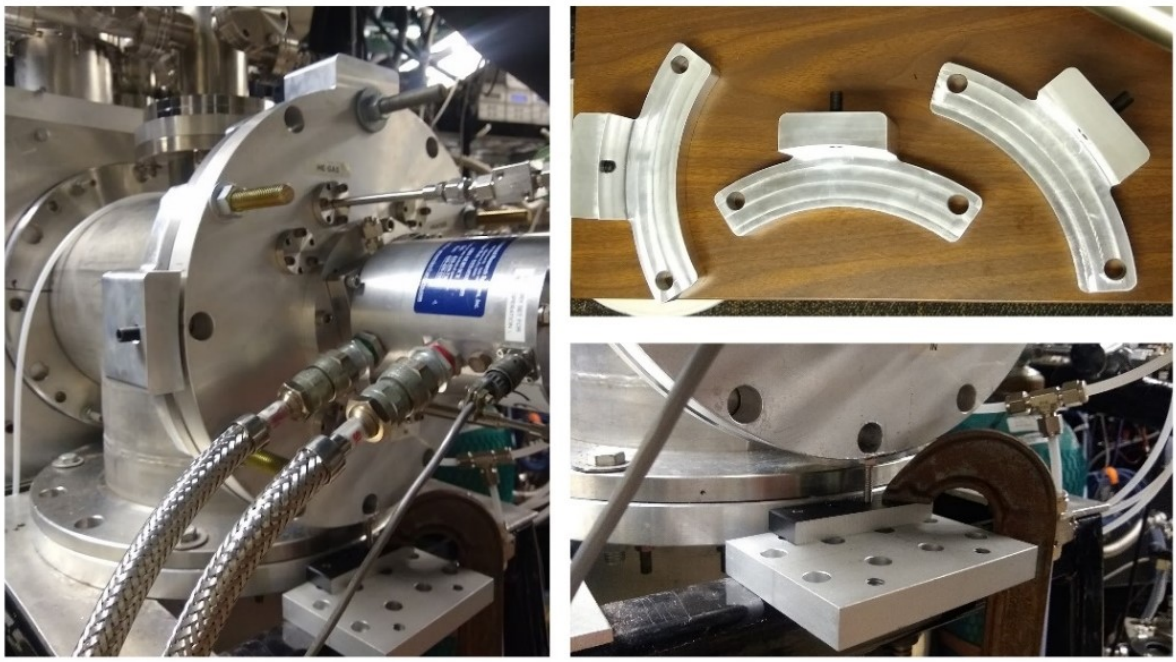

Figure 3.3. Helium droplet source alignment tool. Works by mounting to the source chamber, with bolts applying pressure to the conflat flange on which the droplet source assembly is mounted.

diameter skimmers, to ensure a well collimated droplet jet in the interaction region, with the first skimmer ~1.5 cm away from the droplet nozzle. The droplets then terminate on a residual gas analyzer (RGA), which is used for diagnostics of the helium droplet source.

In between the two skimmers, a 5 cm long gas pick-up cell is installed for doping the droplets with gas phase dopants, as depicted in Figure 3.2 (not to scale). Each end of the cell has 2.5 mm diameter apertures. The base pressure of this cell is also 10^{-8} Torr, so the probability of doping or attenuating the jet unintentionally is low. Pressure of the dopant gas in the pick-up cell is controlled by a high precision leak valve, making it possible to achieve single atom doping regime. Figure 3.2 shows a schematic of the droplet source, with respect to the skimmers and doping cell.

Due to the cold nozzle temperatures and small aperture size of the nozzle, it is possible for the droplet source nozzle to clog, in which case it would need to be replaced. This involves replacing both the platinum nozzle and a gold gasket. The previous supplier of the gold gaskets no longer manufactures them, necessitating a creative alternative. To make the gold gaskets in house, a 1 mm hole is drilled along the center axis of a 2 mm diameter gold wire (Sigma Aldrich, 265802-600MG), and the hollow wire is cut into 0.5 mm thick slices, producing multiple gaskets.

The helium droplet jet must be aligned through the two skimmers, which are separated by ~20 cm. This requires precision control of the droplet source to ensure that the center of the jet is indeed making it to the interaction region. Following the replacement of the nozzle, as described above, the droplet beam needs to be realigned through the skimmers. To improve control of alignment, a set of manual alignment manipulators were designed and added to the flange on which the droplet nozzle is attached. The flange is flat and sits against a Viton gasket, which is greased

with Apiezon-L vacuum grease. Machined aluminum parts were installed on the top, left and right of the source and a breadboard with a bolt underneath, to work with the geometric constraints of the apparatus (see Figure 3.3). By tightening/ loosening the bolts in the alignment manipulators, the droplet flange can be walked around in a controlled fashion. Tightening and loosening the bolts on the flange then allow for further control by adjusting the pointing of the source. Alignment is optimized by minimizing the pressure in the source chamber and maximizing He_n^+ ($n \geq 2$) signal on the residual gas analyzer (RGA). If the droplet jet is going through the skimmers poorly, the RGA in the main chamber mostly detects atomic helium, and a lack of larger He_n^+ features, due to the droplets breaking up before making it to the interaction region.

While experiments herein explore dynamics in neat helium droplets, doping droplets can still serve as a useful diagnostic for helium droplet size determination, in combination with the RGA. Dopant species in the doping cell are at room temperature, while the binding energy between helium atoms in large helium droplets is 7.6 K [71]. When introduced to the ultracold droplet environment, due to the weak binding energy of helium atoms in droplet, the addition of every dopant atom causes the droplet to evaporatively cool, thereby decreasing the total number of atoms. As such, the He_n^+ signal measured by the RGA can be measured as a function of the pick-up cell pressure. A titration has been developed and is described by Gomez *et al*. for size determination of large helium droplets (i.e., droplets with more than 10^4 atoms/droplet), based on the attenuation of the He_n^+ signal as the doping pressure is increased [72].

3.1.2 Laser System

Experiments described in Chapter 4 are performed with a Coherent Legend Elite Duo HE+ Ti:Sapphire laser system. This system was upgraded to provide a higher pulse energy and with a custom central wavelength for experiments herein. The system is seeded by a Vitara oscillator and comprises of two stages of amplification, each pumped by a Coherent Revolution diode-pumped, intra-cavity doubled, Q-switched, Nd:YLF laser. The first stage is a regenerative amplifier bringing the ~500 mW seed up to ~8 W. The second stage is a single pass amplifier yielding ~16 W uncompressed light. After passing through the compressor gratings, the resulting output is a 40 fs, 13 W pulse train at a 1 kHz repetition rate. In comparison with the previous ~4 mJ/pulse of the earlier laser system, the new system affords a substantially higher pulse power and can be used to drive a HE Topas optical parametric amplifier (OPA). For the work described herein, 50% of this laser output is used for the pump and probe.

As will be discussed in the following section, in order to achieve the desired photon energy in high harmonic generation, extensive work has been done to redshift the output of the laser to 804 nm, corresponding to a photon energy of 1.54 eV. To achieve this requires a balancing act of shifting the oscillator spectrum, while maintaining sufficient bandwidth to safely amplify and preserve the compressed pulse duration. The unseeded regen cavity naturally centers at ~785 nm. To achieve a longer wavelength in the amplified light, the oscillator must be redshifted to beyond the desired wavelength. The oscillator is tuned to 840 nm with a bandwidth of 65 nm. After the stretcher, the pulse maintains a 60 nm bandwidth, which is sufficiently broad for safe amplification.

Beyond monitoring the laser power and beam mode, it is important to monitor the profile of the amplification build-up as another diagnostic. Figure 3.4 shows an example of an optimal build-up where the last two round trips of amplification are roughly equal in intensity. In the

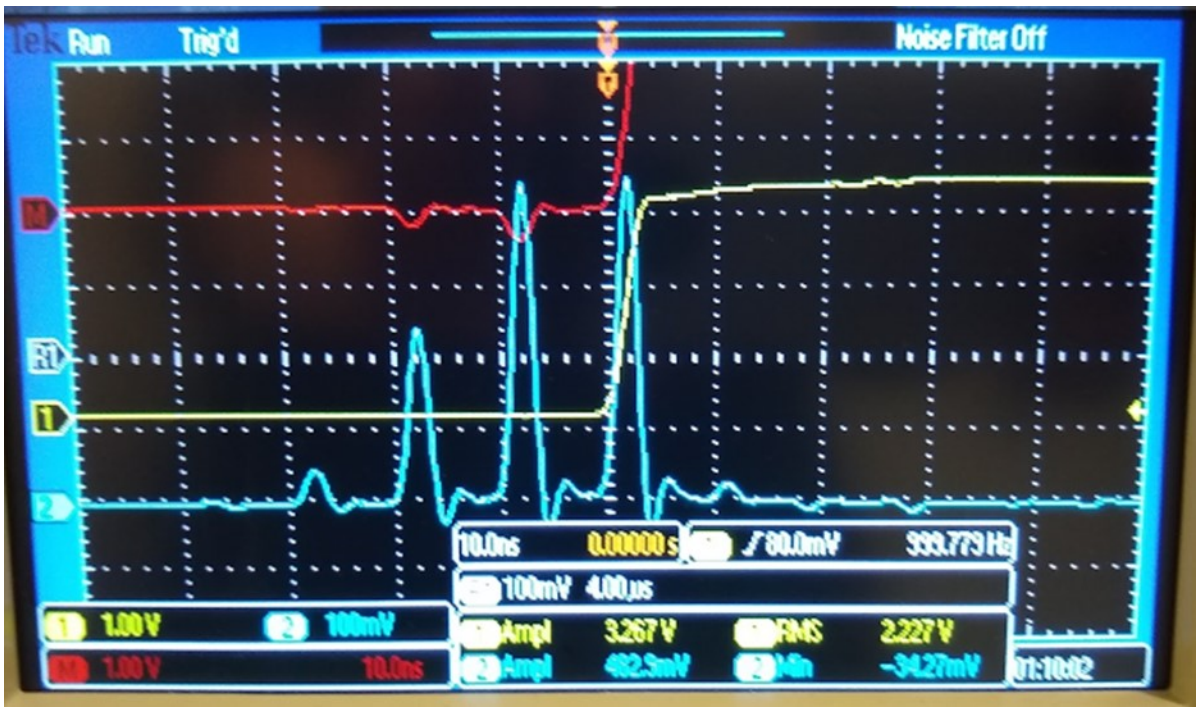

Figure 3.4. Example of the amplification build-up of a well-aligned regenerative amplifier is shown in the blue oscilloscope trace. A photodiode is installed behind one of the cavity mirrors, measuring the leak through of the seed pulse as it travels through the cavity. Only the last 4-5 pulses have sufficient intensity to be measured. Each round trip is separated by ~9 ns.

oscilloscope trace in the figure, the peaks correspond to round trips that the seed is taking through the cavity, with each round trip separated by ~9 ns. The shape/quality of the buildup is important as it reflects on the alignment of the seed into the cavity. A well seeded amplifier corresponds with the most redshifted wavelength in the amplified light, which is necessary for maintaining the 804 nm output.

3.1.3 High Harmonic Generation Source

In this section, first the original HHG design will be presented, followed by specific changes that were implemented to optimize the source for experiments described herein. Full details of the original HHG design driven with NIR are described by Kornilov *et al*. [29]. An overview of the setup is as follows: 2.5-3 mJ of 785 nm driving light focused with a 2 m focal length curved mirror into a 2.5 cm cell filled with 1-5 torr of Kr gas produces 15th -23rd harmonics of the fundamental. A pair of silicon substrates (LEO Si-WR-WM-3”x0.5”x0.25”T) are set at the Brewster's angle for ~800 nm radiation to transmit most of the HHG driving light, which is dumped on a copper block. Due to the wavelength-dependent refractive index of Si, each substrate reflects ~40% of the XUV at the 800 nm Brewster's angle, resulting in a net reflectivity of ~16%. After the silicon dichroics, a thin metal filter, such as 200 nm thick Al or Sn, can be inserted into the beamline to further filter out the residual driving light and for harmonic selectivity. A Mg/SiC multilayer focusing mirror is custom made to reflect low order XUV harmonics. After the silicon substrates, a 100 nm Al filter, and the multilayer, ~20 pJ/pulse are measured in the interaction

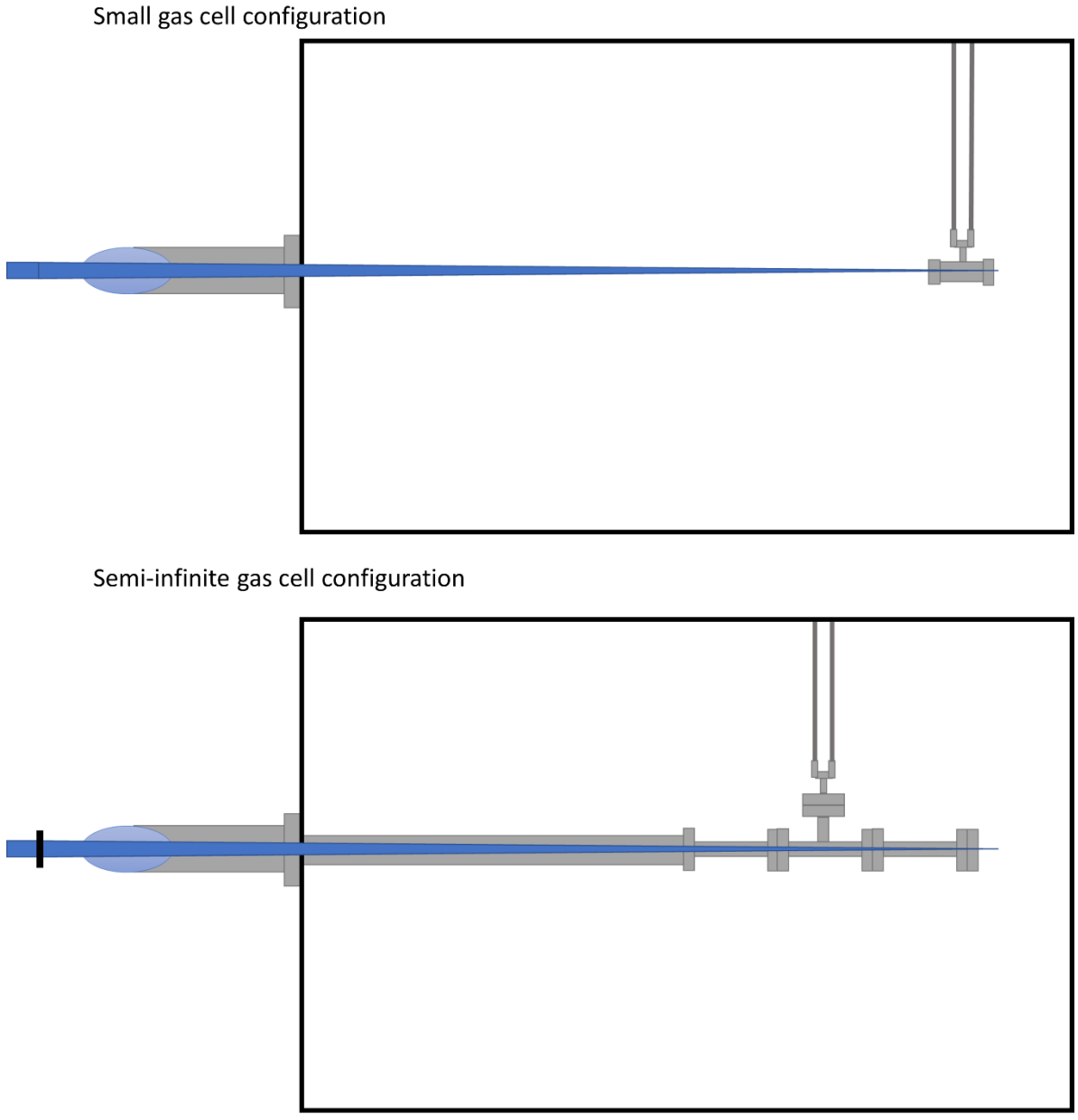

Figure 3.5 Original and current HHG configuration. Key differences include replacing 2.5 cm gas cell with ~ 1 meter semi-infinite cell and switching from a 2 meter focusing mirror to a 1 meter focusing lens.

region distributed across the harmonics. The photon flux in the interaction region is measured with an XUV photodiode mounted just outside the VMI spectrometer and liquid nitrogen cold trap. The photodiode is calibrated such that the number of photons can be determined based on the area of photodiode signal as measured by an oscilloscope. A full description of the measurement can be found in [73]. The XUV spectrum generated via HHG can be observed and optimized using an

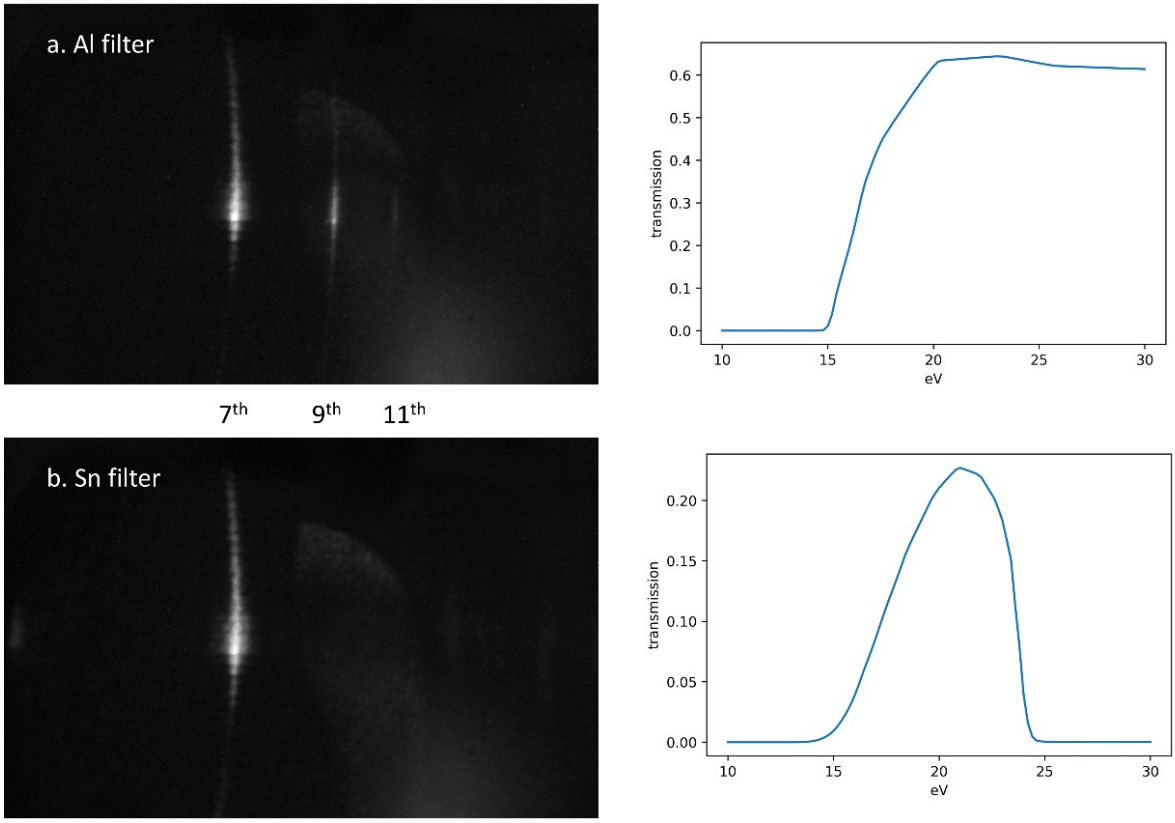

Figure 3.6. 402 nm driven XUV spectrum with a) 200 nm Al filter and b) 200 nm Sn filter. 7^{th}, 9^{th} and 11^{th} harmonics are noted, corresponding to 21.6, 27.7 and 33.9 eV.

in-situ spectrometer, comprising of a slit and a transmissive nanograting followed by an MCP and phosphor screen [74].

Previous experiments with this HHG source were optimized for discrete, low order harmonics (15-17^{th} harmonic), which is optimal for studying the upper absorption feature in helium droplets centered at 23.7 eV (as described in Chapter 1) and just above the ionization potential at 24.6 eV. In this regime, there is very little tunability in shifting the photon energy of the harmonics.

For the present work, the XUV needs to excite the lower droplet absorption feature centered at 21.6 eV. As such, odd order harmonics of a NIR driver do not give access to this lower feature. Extensive work has been done to generate XUV to overlap this helium droplet feature at 21.6 eV. First, 4.5 mJ of 804 nm light is frequency doubled with a 200 µm BBO crystal, resulting in 1.5 mJ of 402 nm (3.2 eV) photons. When used to drive the high harmonic generation, the 7^{th} harmonic of 402 nm (equivalent to 14^{th} harmonic of the fundamental) provides great overlap with the lower droplet absorption feature. Overlap is especially optimized due to the custom redshifted Coherent laser system. With the new laser system centered at 804 nm as compared with the 785 nm output of the original laser system, the 7^{th} harmonic is redshifted from 22.1 eV to 21.6 eV.

With the 402 nm driving light, 5th order and higher order harmonics can be observed with the XUV spectrometer. The 3rd harmonic is too low in energy to be observed on the XUV spectrometer, though this is likely also generated. Initial attempts at generating harmonics with the frequency doubled laser output produced substantial 5th harmonic and some 7th harmonic. Using a 200 nm thick Sn or Al filter, the 5th harmonic can be filtered out, resulting in a mostly isolated 7th harmonic. However, because the initial flux was primarily in the 5th harmonic there was considerable contamination from the 5th harmonic due to its bandwidth and the 7th harmonic was less than ~1 pJ/ pulse in the interaction region. Further work has been done to shift the 402 nm based XUV spectrum towards higher harmonics to increase the 7th harmonic flux and decrease the 5th harmonic flux, with particular emphasis on changes to the geometry of the setup. The differences are summarized in Figure 3.5. First, the focusing conditions were altered. The 2 m focusing mirror was replaced with a 1 m focal length, thin focusing lens (Eksma 110-1245ET). The obvious difference comes from the tighter beam focus due to the shorter focal length. Additionally, in switching to a lens, any astigmatism resulting from using a focusing mirror away from a normal incidence geometry is eliminated. This led to a factor of 2 improvement in the 7th harmonic flux. A more substantial improvement came from a change in the cell geometry. The 2.5 cm HHG gas cell was replaced by an ~1 m long semi-infinite cell [75]. In the original configuration, the first ~ 50 cm of light were focused in air, with the remaining focusing happening in vacuum. With the new configuration, the beam enters the chamber through a Brewster window into the krypton gas filled semi-infinite cell about one centimeter after the focusing lens. In switching to a semi-infinite configuration, the 7th harmonic flux increased to ~25 pJ /pulse in the interaction region. A sample spectrum with an Al filter is shown in Figure 3.6a, with 7th, 9th and 11th harmonic present, as a result of shifting the spectrum to higher order harmonics. Use of a Sn filter fully blocks the 9th and 11th harmonics in addition to the 5th, effectively isolating the 7th harmonic, as seen in Figure 3.6b. Figure 3 also shows the transmission spectra of Al and Sn filters for reference.

3.1.4. Beam Path

Details of the beam path are illustrated in Figure 3.7. The beam path details are presented in the text (and figure) in the following breakdown: first, the beam path out of the laser to the pump arm and before recombination is discussed (Figure 3.7a), followed by details of the probe arm (Figure 3.7b), and last an overview of the recombined pump-probe beam path (Figure 3.7c). Taking into consideration the damage threshold of the BBO and avoiding multiphoton effects from the probe beam, only about half of the output of the laser system is necessary for the helium droplet experiments. Consequently, it is necessary to find ways of attenuating the laser beam without compromising the integrity of the pulse. When working with ultrafast pulses, it is best to minimize the amount of glass through which the pulse travels, thus necessitating thin optics. First attempts included using a thin beam splitter and a thin waveplate + polarizer combo. Both methods proved to warp the thin, transmissive optics under the high intensity of the laser output, affected the focus of the light, second harmonic conversion efficiency and high harmonic efficiency. One option to work around this is to increase the beam size with a telescope, thus decreasing the intensity. A thin lens based telescope is inadvisable for a high intensity pulse (though at more moderate intensities lenses can be a suitable choice, and may be preferable, to avoid astigmatism). While this is a common strategy, reflective focusing optics can introduce astigmatism, and this would necessitate another telescope after the beam has been attenuated to shrink the beam size down for

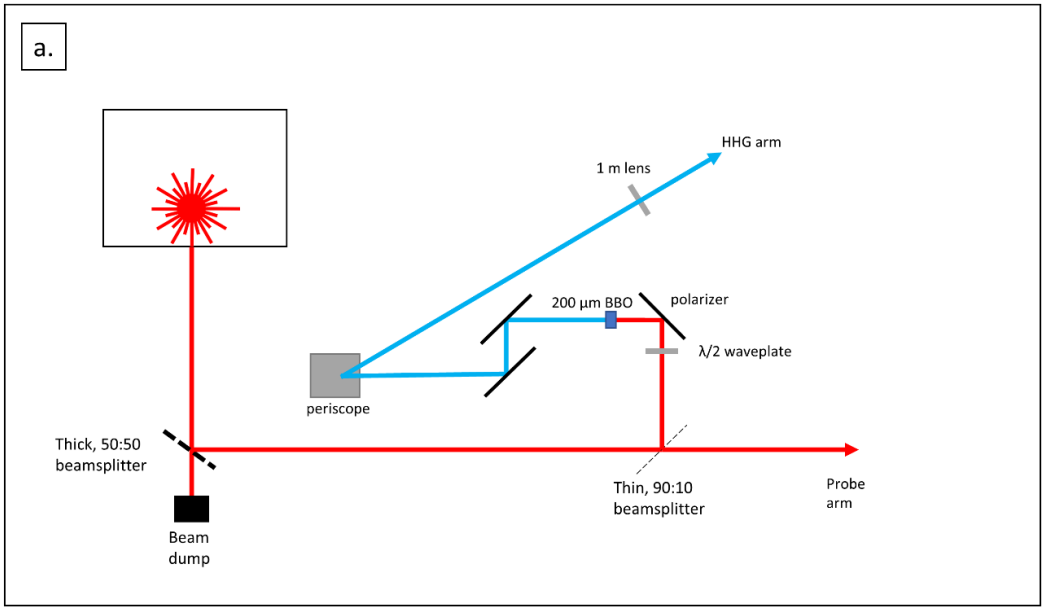

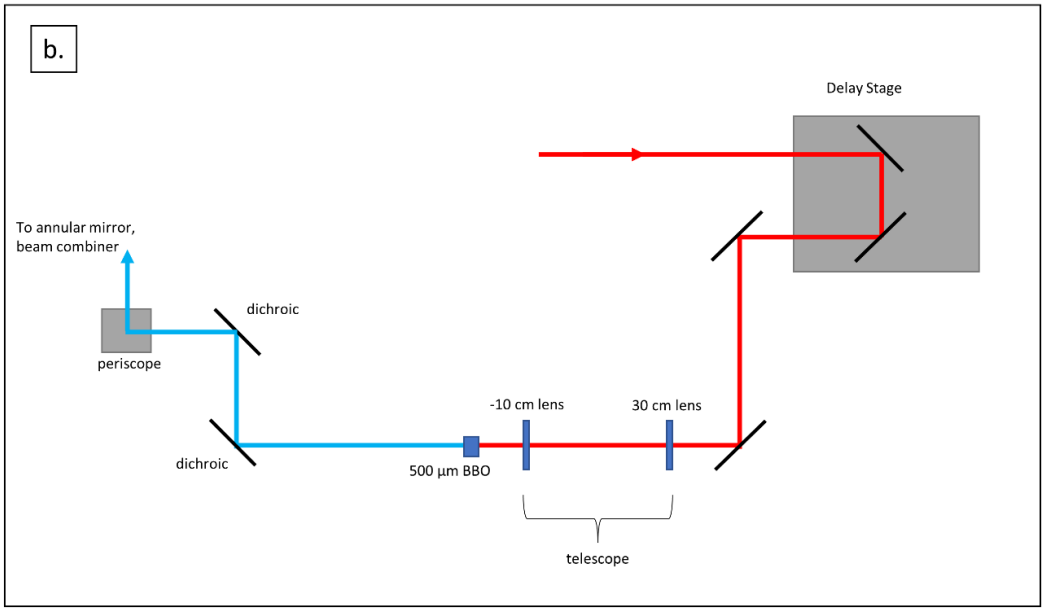

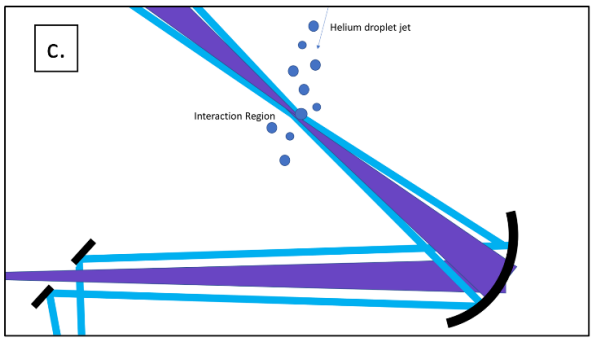

Figure 3.7 a) pump beam path b) probe beam path c) pump probe overlap

use with the BBO. Instead, a simple solution has been implemented. Because the unwanted power is unused, a thick 50:50 BS is used, with the reflected beam directed to the experimental setup and the transmitted beam dumped on beam block. In using a thick optic, its integrity is not compromised by the intensity of the beam.

After the beam has been attenuated, it goes through a 90:10 BS, which separates the light into the pump and probe arms. The pump arm (the reflected beam) undergoes second harmonic generation followed by high harmonic generation, producing XUV used to excite the helium droplets. First, the pump beam fundamental is routed through a thin waveplate in combination with a polarizer, which allows for precise control of the laser power used to pump the BBO and to optimize the intensity driving the HHG. This also selects for vertically polarized light. It is necessary to flip the polarization before SHG, as the BBO flips the polarization. Horizontally polarized light is necessary for compatibility with the orientation of the VMI spectrometer (described in 3.1.5).

Two dichroic mirrors act as high reflectors for the UV light, steering the beam to a periscope while filtering out residual driving NIR light. The light is then focused into the HHG gas cell. Roughly 2 meters after the focus, a pair of silicon substrates are set at the Brewster's angle to transmit 400 nm, while the XUV resulting from HHG is reflected with ~40 % reflectivity per substrate. Subsequently, a filter mount can be slid into the beam path to further filter any remaining driving light, as well as to provide further selectivity of the XUV photon energy. In order to be flexible for harmonic selection, a filter mount on a linear motion device was designed and installed to easily switch between Sn (a bandpass) and Al (a high pass) filters in the XUV regime of interest.

After the 90:10 beamsplitter, the probe arm is routed to a delay stage (Newport GTS-150), allowing for a variable path length difference between the probe arm with respect to the pump arm, therefore changing the time delay between the pump and the probe. Because the pump and probe are focused by the same final focusing mirror, care must be taken to ensure that the two beams focus in the same location in the main chamber. The focus is dictated by the XUV beam following the relation: $\frac{1}{f} = \frac{1}{d_1} + \frac{1}{d_2}$ where f is the focal length of the focusing mirror, d_1 is the distance from the point source in the HHG chamber, and d_2 is the distance from the optic to the XUV focus in the interaction region [76]. Given that the focus in the HHG chamber is fixed, the probe beam path contains a telescope, used to change the effective position of the virtual point source of the probe, so that it is effectively the same as in the HHG arm. The telescope makes use of a diverging and focusing lens to avoid focusing the ultrashort pulse in air, which may lead to deterioration of the pulse characteristics due to nonlinear effects, such as self-focusing and self-phase modulation. After the telescope, the probe is directed into the chamber by a periscope to be recombined with the pump beam.

The pump and probe arms are recombined via an annular mirror. The XUV pump travels through the center of the so-called “holey mirror” and the probe is centered around the hole, such that the outer edges are reflected and can be aligned collinearly with the XUV arm. This is illustrated in Figure 3.7c. The XUV pump and 402 nm probe are then both focused by a 1” Mg/SiC multilayer curved mirror with a one meter radius into the interaction region where they intersect the helium droplet jet. The multilayer works to reflect the XUV as a result of the difference in refractive index between alternating layers of two materials (in this case Mg and SiC), such that the XUV reflects according to Bragg’s law [20]. For ease of optimizing spatial overlap between the pump and probe, a motorized mirror is installed in the vacuum chamber after the annular mirror. This can be moved into the beam path to direct the probe and residual HHG driving light

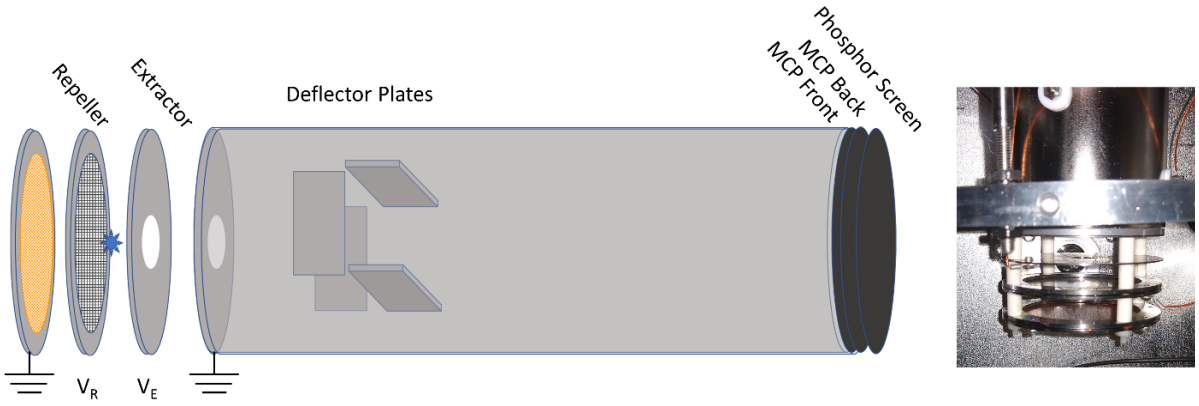

Figure 3.8. Schematic and photo of VMI spectrometer used in lab-based measurements. The interaction region is denoted in blue.

out of the vacuum and onto the optic stable. The beams travel roughly the same distance to a half meter focusing optic on the table, comparable to the path in vacuum. Spatial overlap is tuned around the focus on the optics table with the aid of a beam profiling camera.

3.1.5 Photoelectron Imaging

A schematic of the VMI spectrometer used is shown in Figure 3.8, along with a photo. Per the standard design of a VMI spectrometer, the one used herein consists of a repeller and extractor, followed by a field drift tube. In place of a solid repeller, a mesh grid is used. Additionally, below the repeller, there is a grounded mesh grid. These mesh grids can be seen in the photo in Figure 3.8. These mesh grids were installed for compatibility with an ion time-of-flight spectrometer on the bottom of the chamber, however they also provide advantages for the VMI spectrometer. The decreased surface area of the mesh grid reduces the background signal of stray light striking the electrodes, and the grounded mesh attracts spurious electrons born on the repeller. This effect was tested when the repeller mesh needed replacement. Initially it was replaced by a fine copper mesh, which led to an increase in background signal. In switching back to a coarser mesh, normal imaging conditions were achieved. Voltages used are -5000 V/ -3320 V, nominally allowing for imaging of up 14 eV electrons. In practice, two sets of parallel plate capacitors, or deflection plates, are oriented orthogonally with respect to each other and are used to walk the center of the image towards the edge of the detector so that one quadrant can observe up to ~20 eV electrons.

As was discussed in Chapter 2, VMI records a 2D projection of a 3D distribution of photoelectrons (or ions). This projection is called an Abel transform. So long as the photoelectron distribution has cylindrical symmetry with respect to the axis parallel to the detector, an inverse Abel transform can be performed to reconstruct the original distribution. Then a 2D slice through the center of the distribution can be extracted. Various methods have been developed to achieve this in practice. Most common methods include BASEX, pBASEX, and a maximum entropy method [77]–[79]. BASEX, the basis set expansion, is a computationally inexpensive method in

which well-behaved Gaussian-like functions are fit to the image. This was expanded to a polar coordinate system, rather than cartesian, in the pBASEX implementation.

3.1.6 Diagnostics

Following the installation of the new laser, initial measurements were performed with NIR driven harmonics. This gives a direct comparison to confirm the redshifted laser results in the expected redshifted XUV spectrum. The original laser with a 785 nm central wavelength produces a 15th harmonic at 23.7 eV. This is resonant with the atomic helium $1s^2 \rightarrow$ 1s4p transition. The 15th harmonic of 804 nm, in comparison, is resonant with the $1s^2 \rightarrow$ 1s3p transition with a 23.1 eV photon energy. In both cases, $h\nu_{XUV} + h\nu_{NIR} - IP_{He} > 0$. Figure 3.9 shows the XUV+NIR photoelectron spectrum in atomic helium measured with the old and new laser system. A schematic of the excitation scheme and expected photoelectron kinetic energy is drawn next to the spectra. As can been seen in the figure, the pump-probe in atomic helium yields a different photoelectron spectrum with the new laser system, confirming the redshift in high harmonic generated XUV photon energy.

Atomic Rydberg states are also an ideal system to determine the temporal cross correlation of the pump and probe pulses. For the NIR driven XUV, the atomic helium system described to confirm the redshift in the photon energy is also used for the cross correlation. The pump-probe signal associated with population of the long-lived Rydberg state is approximated as a Heaviside step function convolved with the Gaussian profile resulting from the pump-probe cross correlation. In Figure 3.9c, the intensity of the photoelectron signal is plotted as a function of pump-probe time delay. The data is then fit to an error function corresponding to the convolution of a Gaussian and

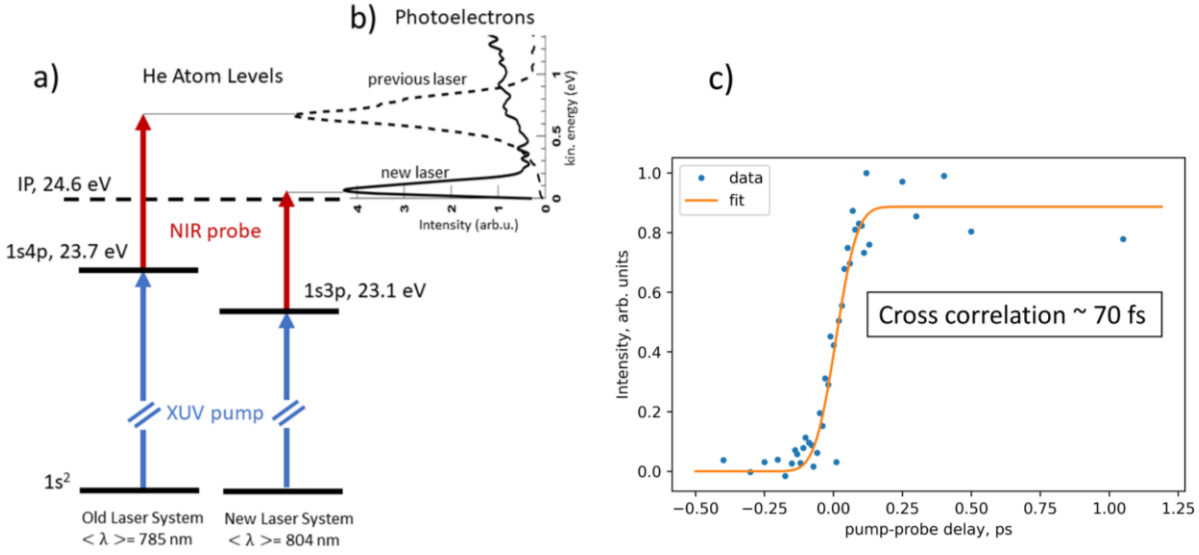

Figure 3.9 a) schematic of XUV+NIR excitation in atomic helium with original and new laser system b) Atomic helium XUV + NIR spectra with old and new laser system to demonstrate redshift. c) cross correlation NIR driven XUV + NIR probe in atomic helium with new laser.

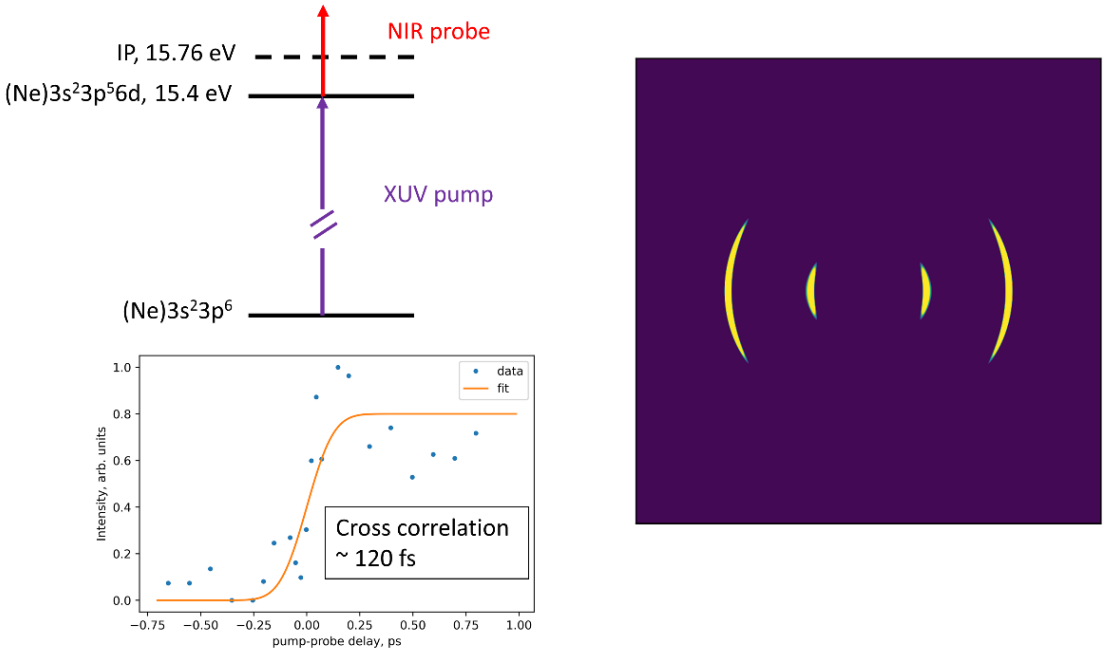

Figure 3.10. Schematic of pump probe in atomic argon. Inverse Abel transformed VMI image with argon. Cross correlation in argon.

step function. The cross correlation indicates an instrument response function with a full-width-at-half-maximum (FWHM) of ~70 fs. For the 402 nm driven HHG, the harmonics are no longer resonant with atomic helium states, as the 2p state is at 21.2 eV as opposed to the center of the droplet absorption at 21.6 eV. Thus, atomic argon is a better system for a cross correlation measurement. The 5th harmonic of 402 nm is at 15.4 eV, which is resonant with the 3p to 6d transition in atomic argon. With a NIR probe, the total photon energy exceeds the argon ionization potential (15.76 eV) (see Figure 3.10). Measurements are performed without a filter so that the 5th harmonic is not blocked. In Figure 3.10, an example VMI image (after the inverse Abel transform is applied) is shown, with the lower energy feature corresponding to 5th harmonic + NIR ionization and the higher energy feature resulting from one-photon ionization by the 7th harmonic. After the VMI images are inverse Abel inverted, each image is integrated over the lower kinetic energy feature as a function of pump-probe delay, as plotted in Figure 3.10, revealing a 120 fs FWHM response function from a cross correlation.

3.2 LCLS

Single shot x-ray scattering images are measured in coincidence with ion TOF spectra for helium droplets exposed to soft x-rays. Experiments are performed at a large-scale user facility at SLAC National Accelerator Laboratory, using the LCLS. X-rays are focused into the interaction region of the vacuum chambers where they intersect the helium droplet jet. An ion time-of-flight

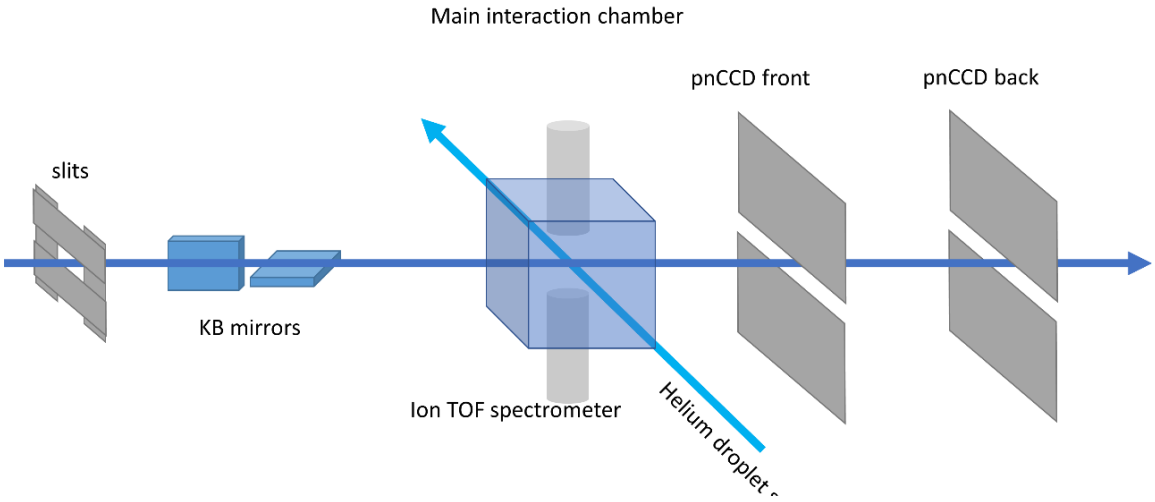

Figure 3.11. Overview of AMO beamline. X-rays travels through a set of slits which can be used to clean up the beam, followed by a pair of KB mirrors, which focus the beam into the interaction region of the main chamber. The main chamber is compatible with various ion and electron spectrometers and atomic and molecular sources. Downstream, two sets of pnCCD detectors are installed to measure small angle x-ray scattering.

spectrometer is used in coincidence with an x-ray scattering detector. The various components of the end station will be discussed in more detail below.

3.2.1 Overview of components at AMO end station

At the LCLS, there are 7 experimental hutches, each with specialized capabilities depending on x-ray photon energy (i.e., soft vs. hard x-rays) and scientific goals (e.g., matter in extreme conditions, crystallography, soft x-ray science). The LCLS was recently upgraded by the addition of the LCLS II, which will ultimately operate at much higher repetition rates (up to ~1 MHz compared to 120 Hz at LCLS I) enabled by a superconducting LINAC to accelerate the electron bunches. However, the experiments described herein were performed with the original LCLS I. The FEL beam can only be directed to one hutch at a time, although typically two experiments are scheduled concurrently at different hutches, with alternating 12 hour shifts with the beam. Experiments performed in our group make use of the Atomic, Molecular, and Optical (AMO) sciences hutch [80] (which has since been renamed TMO, time-resolved molecular and optical sciences, with the FEL upgrade). An overview is seen in Figure 3.11. At the AMO hutch, the Laser Applications in Materials Processing (LAMP) end station is designed to accommodate a variety of experiments [81]. The LAMP end station is modular with flexibility in both detection schemes and the sources used for the system of interest. Detector capabilities include electron time-of-flight spectroscopy, ion time-of-flight spectroscopy, ion imaging, ion momentum spectroscopy and x-ray scattering. Relevant AMO instrument and LAMP end station parameters

are summarized in Table 3.1. Other capabilities include coupling in an ultrafast NIR laser beam, as well as x-ray pump x-ray probe measurements. The chamber is compatible with a variety of atomic, molecular, and cluster sample sources, including custom sources provided by the user.

Energy Range (eV)	280-2000
Focused beam size (um)	1.5
Flux (photons/pulse)	$\lesssim 10^{13*}$
Pulse length (fs)	5-200
Repetition Rate (Hz)	120, 60, 30, 10, 5, 1
Standard photon detectors	Two pnCCDs
Standard spectrometers	Ion/electron VMI/reaction microscope, electron TOF, ion TOF, ion momentum TOF, VMI

Table 3.1 Summary of AMO capabilities.

For the work described further in Chapter 5, the photon energy is 838 eV, with a pulse duration of 65 fs, delivered at a 120 Hz repetition rate. A few key beamline components are presented in the following. Upstream of the main interaction chamber, there is a pair of slits that can be adjusted to reduce stray light. A pair of Kirkpatrick-Baez (KB) mirrors is used to focus the x-ray beam. KB mirrors are ellipsoidal, grazing incidence optics used in a pair, perpendicular to one another, with each mirror focusing the x-rays long the axis which they reflect off the mirror [20]. A nominal 2.5 μm^2 focal spot size can be achieved in the interaction region. Based on the LCLS operating parameters and previous beamline transmission measurements, in our measurements, the average pulse flux is expected to be on the order of $\sim 10^{16}$ W/cm^2 ($\sim 10^{23}$ photons/m^2) in the interaction region.

On the main chamber, the gas and cluster atomic and molecular sources can be mounted perpendicular to the x-ray beam. For the experiments herein, a helium droplet source chamber provided by the Vilesov group is used. This source operates on the same principles as the one described in 3.1.1, with a different liquid helium compressor to cool the nozzle and a slightly different nozzle design, which achieves colder temperatures. Thus, a lower nozzle backing pressure is needed in comparison with the lab-based experiment to generate the same droplet sizes. With a 5 μm nozzle cooled to 5.8 K, a 20 bar backing pressure is used, typically resulting in an average droplet size of 10^9 atoms/droplet. The distance between the helium droplet source and x-ray focus is ≈700 mm (approximately 4 ms travel time). Across from the helium droplet source, a residual gas analyzer is mounted for diagnostics as mentioned in 3.1.1. The entire setup, including the experimental chamber and the droplet source, is mounted on a motorized stand such that the cluster beam can be walked vertically with respect to the x-rays and along the x-ray beam propagation direction, to optimize the x-ray—droplet overlap and the x-ray focus position. Mounted vertically on the chamber around the interaction region, perpendicular to both the droplet and the x-ray beams, a variety of ion and electron detection schemes can be implemented. Details of the various detectors are described in [81]. We use the double-sided combination of an ion time of flight spectrometer and electron velocity map imaging detector; however, measurements are

exclusively recorded with the ion TOF spectrometer. The spectrometer can be installed so that the x-ray beam is not obstructed, thus allowing for downstream measurements concurrently.

Downstream of the interaction region, two pairs ("front" and "back") of pnCCD detectors are installed to measure x-ray diffraction. These are installed with a variable gap to allow the x-ray beam (and other laser beams if present) to pass through, without destroying the detectors. Having two sets of detectors, one closer and one farther from the interaction region, allows for a wider range of scattering angles to be measured, with the front detector better suited for larger scattering angles and the back detector better for smaller angles. Also downstream of the interaction region, a variety of other x-ray diagnostics exist, beyond the pnCCD detectors, such as a time-tool for pump-probe measurements and x-ray beam imaging on a YAG crystal for x-ray alignment.

Individual x-ray scattering images and ion time of flight spectra are recorded for each x-ray pulse. For optimization of our experiment the x-ray beam is first aligned through the beamline. YAG crystals, which fluoresce when irradiated with x-rays, and cameras for viewing are installed and utilized as part of the x-ray alignment. Once the x-rays are aligned, then the main chamber and connected source chamber are vertically walked to ensure maximal overlap between the x-rays and droplets. Alignment of the helium droplet source ensures that droplets intersect the x-ray beam at the focus, along the axis of x-ray beam propagation, i.e., ensuring the droplets are not upstream or downstream of the focus. Not every x-ray pulse interacts with a helium droplet, so the alignment is optimized by maximizing the "hit rate", or frequency of the x-rays interacting with a droplet, as viewed the frequency of x-ray scattering images or appearance of ion TOF spectra. With the 120 Hz repetition rate, not every image/spectrum can be viewed in real time. Thus, it is important both in real time during the experiments and offline for analysis to apply a "hit finder" to the incoming data. This can be done either by setting a threshold on the intensity of scattering images or in corresponding TOF spectra. Then, the images and spectra corresponding to an event in which an x-ray pulse interacts with a droplet can be viewed in real time. The frequency of the interaction can then be optimized and monitored.

3.2.2 Ion TOF Spectroscopy and Analysis

A double-sided ion TOF and electron VMI spectrometer are mounted vertically in the chamber. For the experiments herein, only the ion spectrometer is used. On the ion extraction electrode, a 10 mm × 1 mm slit aperture is mounted and aligned perpendicular to the FEL beam to suppress detection of ionized background gas outside the FEL focus. In Figure 3.12, a schematic and photo of the ion TOF spectrometer are shown. Based on the electrostatic optic numbering scheme used in Figure 12, the corresponding voltages used are summarized in Table 3.2. Because this spectrometer does not conform to Wiley McLarin conditions, while the spectra still encode the kinetic energy information, analysis of the spectra resulting from such spectrometer conditions becomes more complicated and can be aided by simulations. SIMION® is a computer software that can be used to calculate electric fields and the trajectories of charged particles in those fields. Thus, the ion TOF spectrometer can be modelled and the corresponding spectra can be simulated for the different cationic species and kinetic energies of interest assuming an isotropic 3D emission.

For our experimental results (see Chapter 5), many of the TOF features are saturated. We focus analysis on the rising edge of the features in the spectra, which can be determined with high fidelity. A comprehensive study of the relationship between TOF and kinetic energy was

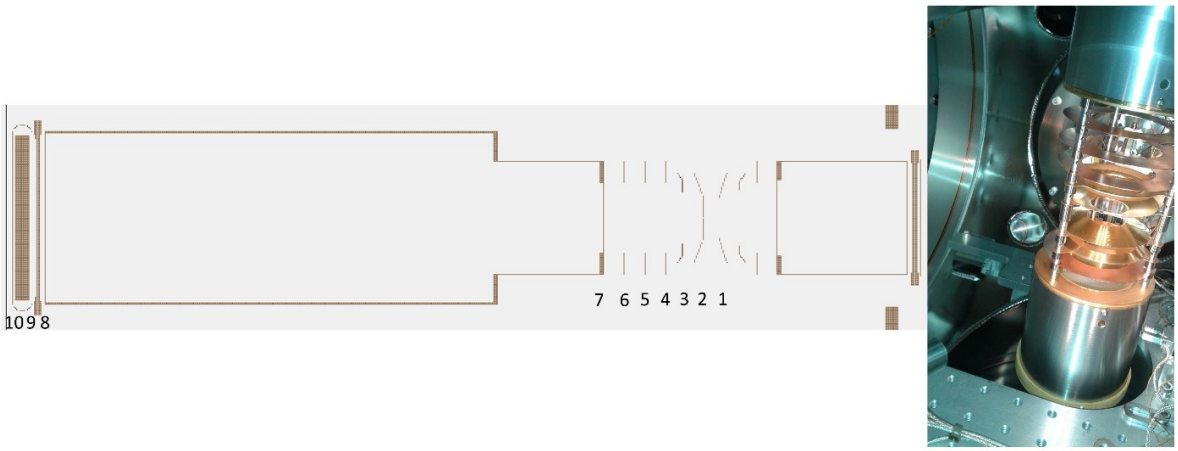

Figure 3.12. Overview and photograph of ion TOF spectrometer. Relevant ion optics and detectors are number with the corresponding voltage in Table 3.2.

performed to confirm that in all cases, although backwards ejected ions can arrive at the detector faster than the zero kinetic energy ions, in all possible conditions, forwards ejected ions always arrive at the detector faster than ions of the same kinetic energy with a different initial direction. Thus, the shortest time of flight uniquely corresponds to the maximum ion kinetic energy (specifically of "forwards" ejected ions, i.e., toward the detector). For our analysis, the shortest time of flight of each peak is determined and then converted to ion kinetic energy. The relationship between time of flight and forwards ejected ion kinetic energy is shown in Figure 3.13 for He^+ cations. The same analysis was also performed for He_n^+ for n = 2-4, covering correspondingly different TOF ranges.

Component	Voltage, V
1, ion optic	500.026
2, ion optic	-923.011
3, ion optic	-1392.992
4, ion optic	-1490.011
5, ion optic	-1564.012
6, ion optic	-1639.025
7, time of flight tube	-1714.647
8, MCP front	-2400
9, MCP back	5
10, phosphor screen	6000.01

Table 3.2 Ion Time of flight spectrometer voltages

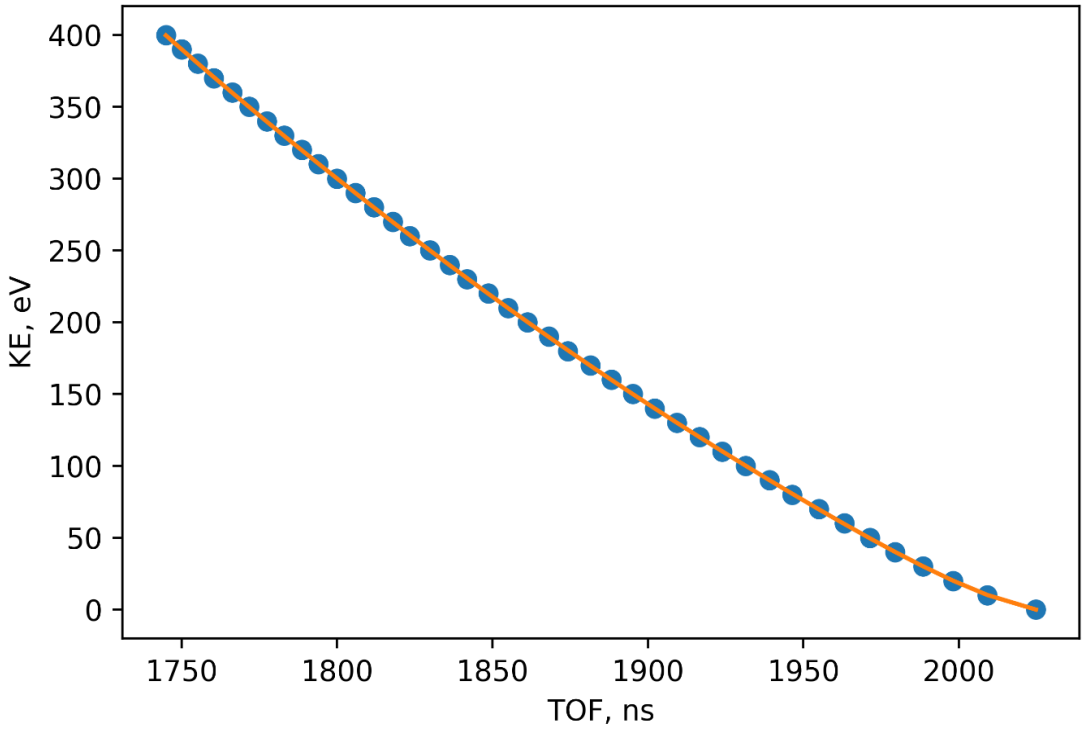

Figure 3.13. Conversion from ion time of flight to ion kinetic energy for forward-ejected He^+ cations.

3.2.3 X-ray Scattering Measurements and Analysis

X-ray scattering is recorded using pn-charge-coupled device (pnCCD) detectors. Specifically, measurements are performed using the back pnCCDs which are 710 mm downstream from the interaction region. Each imaging detector includes two (75×37.5 mm^2) pnCCD panels, with each panel comprising approximately half a million 75×75 μm^2 pixels. The two pnCCD panels are separated vertically by an adjustable gap through which the x-rays can pass. For this experiment, the panels are separated by a gap of 1.5 mm and each panel has a 4.4×1.8 mm^2 central cutout. This allows for the x-ray beam to be measured or viewed downstream, but more importantly it protects the detector from damage induced by the full x-ray beam. The detector records small angle x-ray scattering patterns (($q \sim 2\times10^{-3} - 2\times10^{-2}$ $Å^{-1}$ for the 838 eV photon energy used herein). Careful analysis of the detector images allows for calibration of the single photon response. Subsequently, the absolute number of scattered photons can be deduced from the images. As will be discussed in greater detail in chapter 5, the x-ray fluence experienced by each helium droplet can be determined from the number of scattered photons. Additionally, the scattering image reflects the size of the droplet. Thus, on a shot-by-shot basis, the photon fluence and droplet size are known. This information can be correlated with the ion TOF spectra.

An important aspect of the x-ray scattering images is reduction of stray light as this reduces the fidelity of the image analysis. Any stray light limits the amount of usable scattering images, both in obfuscating the diffraction rings and in count of scattered photons. In addition to slits installed in the beamline upstream of the main chamber, additional slits and apertures can be installed just before the interaction region. These should be installed as close to the interaction region as possible without compromising the ion TOF spectrometer. The slits and apertures are optimized on the pnCCDs by minimizing the amount of light the detector sees, in the absence of scattering images.

Chapter 4

Femtosecond time-resolved photoelectron imaging of ICD in helium nanodroplets

The content and figures of this chapter are reprinted or adapted with permission from C. A. Saladrigas, N. A. Helvy, C. Claudio, D. M. Neumark, and O.Gessner, manuscript in preparation for publication

Resonant interatomic Coulombic Decay (ICD) in multiply excited helium nanodroplets is studied via femtosecond time-resolved extreme ultraviolet (XUV) pump- UV probe photoelectron spectroscopy in conjunction with a series of droplet size and XUV intensity dependent ion yield measurements. Use of a tabletop high harmonic generation source allows us to explore ICD at low excitation densities, near the threshold of multiphoton absorption in helium droplets. In contrast to previous experiments with high intensity XUV free electron lasers, we are in a regime in which interactions between excited helium atoms are limited to two-atom interactions. Time dependent measurements reveal that with ~0.01% of the droplet excited, ICD happens on ~1 ps, which is comparable to the lifetime measured with two order of magnitude higher excitation densities. Complementary intensity dependent ion yield measurements show that the dependence goes from a quadratic to a linear relationship with increasing helium droplet size. These results may be used together to learn about the relationship between ICD and excitation density in the droplet and demonstrate the feasibility of studying multiphoton condensed phase excited state dynamics using a tabletop source.

4.1 Introduction

Helium nanodroplets are an ultracold and optically transparent medium that weakly interacts with dopant species [10]. When exposed to XUV radiation, the droplet is electronically excited and subsequently undergoes a variety of relaxation mechanisms [30]–[33], [82], [83]. In general, understanding photoexcited electron dynamics in condensed phase media applies to a variety of systems, for example gaining a deeper understanding of solvents and solvent-solute interactions and biological systems [84]. Helium droplets make an ideal system for studying relaxation and energy transfer dynamics both experimentally and theoretically. Because the average droplet size can be finely tuned, the physical cross section and therefore the average number of photoabsorption events can be controlled. Additionally, in tuning the size of the droplets, the ratio of bulk to surface can be controlled. Although a full theoretical model of condensed phase systems with thousands to millions of atoms per system is still an active challenge, the electronic simplicity of helium and weak binding energy between helium atoms has advantages in studying interatomic processes and condensed phase dynamics.

Helium droplets have two broad absorption features centered at 21.6 eV and 23.7 eV, arising from n = 2 and n>2 atomic levels, respectively [85]. While the atomic helium ionization potential (IP) is at 24.56 eV, above 23 eV an onset of slow photoelectrons has been observed for droplets, as the result of an autoionization mechanism [14]. The relaxation dynamics have been

the subject of many experimental studies. A variety of time-resolved studies of following an excitation into the upper absorption feature reveal a variety of relaxation mechanisms, including ejection of Rydberg atoms with different properties depending on whether they originate on the outer or inner surface layers of the droplet, formation of He_n^+ clusters, and interband relaxation [31]–[33]. Another experiment investigates time-resolved relaxation following an excitation into the lower absorption feature [83]. Analogous with the upper absorption feature, the delocalized excitation relaxes into atomic Rydberg states, with ultrafast relaxation facilitated by the surrounding droplet medium. Further, the results are consistent with formation of void bubbles surrounding the He* atoms when they originate in the bulk of the droplet, as is confirmed by theoretical calculations.

With the large absorption cross section of the atomic helium 2p state, the lower absorption feature consequently very strongly absorbs at 21.6 eV [13]. A series of experiments have explored multiphoton absorption in the lower absorption feature [86]–[88]. In this case, Interatomic Coulombic Decay, or ICD, arises as a competitive deexcitation pathway. ICD is a relaxation process found in weakly bound systems from dimers to large van der Waals clusters [89]–[92]. Broadly, one of the constituents is ionized or excited, creating an inner-valence or core hole. Then, when the constituent relaxes to fill the hole, the energy released is transferred to a neighbor. The energy transfer results in ionization of the neighboring atom. Because ICD is facilitated by a dipole-dipole interaction, the efficiency depends strongly on the separation distance between the two species. In the regime of multiphoton absorption in helium droplets, when two void bubbles with He* meet and merge, ICD is facilitated by the proximity of the two excited helium atoms [88]. In this case, one of the He* atoms relaxes, transferring its energy to the neighboring He*, which then has sufficient energy to ionize the neighbor. The result is a neutral He, He^+ and the ejection of an ICD electron with kinetic energy equal to twice the single-photon excitation energy less the ionization potential of atomic helium. As the XUV flux increases and the density of excited helium atoms increases, the ICD interaction can happen between multiple helium atoms. This leads to inelastic processes with the freed electrons such as scattering and excitation or ionization of nearby excited atoms. Consequently, there is a decrease in the electron kinetic energy. This multi-atom ICD process is referred to as "collective autoionization" or CAI.

Here, we study the efficiency of ICD as a relaxation mechanism in droplets near the onset of multiple photoabsorption events, revealing that ICD is highly efficient even with a few absorptions in photoexcited droplet (~0.01% excited population), with an ~1 ps lifetime that is relatively insensitive to the density of excitations in the droplet. Time-resolved measurements at higher photon fluxes and 0.1-1% excited population in the droplet measure similar lifetimes from ~900 – 400 fs, with the timescale decreasing with an increasing percentage of atoms in the excited population [88]. We utilize femtosecond time-resolved photoelectron spectroscopy in conjunction with intensity and droplet size dependent ion yield measurements. A tabletop high harmonic generation (HHG) source is optimized specifically to excite the droplet at the center of the absorption feature at 21.6 eV. The results may give insight into the relationship between the initial excitation density and the efficiency of ICD in the helium droplet environment. This study also demonstrates that multiphoton XUV induced dynamics can be explored utilizing a tabletop source rather than a largescale user facility.

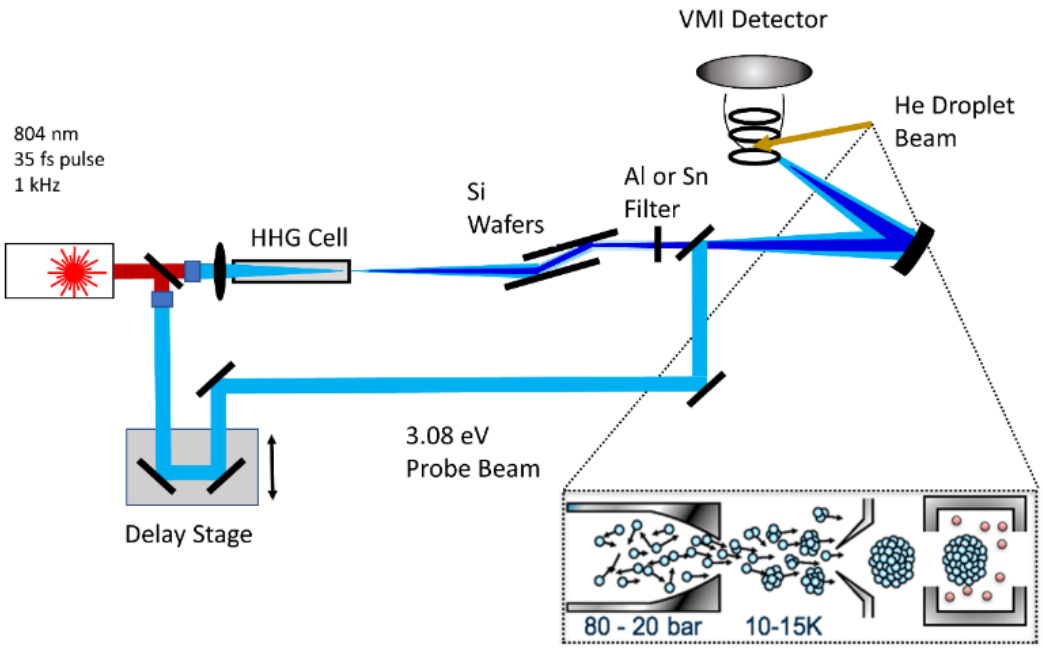

Figure 4.1 Experimental Setup. Helium nanodroplets are excited by a 21.6 eV high harmonic generated XUV pulse and the subsequent photoelectron spectrum or ion yield are measured using a velocity map imaging spectrometer. For time-dependent measurements, a UV probe pulse is used to measure the photoelectron spectrum at various pump-probe time delays.

4.2 Experiment

Resonant ICD in helium nanodroplets is studied via femtosecond XUV pump – UV probe time-resolved photoelectron imaging spectroscopy. An overview is presented in Figure 4.1. Helium droplets are produced in a jet via the expansion of 80 bar of 99.9999% purity helium through a 5 µm diameter, cryogenically cooled nozzle into vacuum. Nozzle temperatures used in the present study range from 13.5 – 16 K, resulting in ~10^4 – 10^6 atoms per droplet, on average. The pump and probe beams are generated using 6 mJ of a Ti:Sapphire laser system with a central wavelength of 804 nm. The laser system is specifically tuned to this wavelength, such that the 7th harmonic of the frequency doubled output is resonant with the center of the lower helium droplet absorption feature. A 90:10 beam splitter is used to split the laser output into the pump and probe arms. The pump arm is frequency-doubled with a 200 µm thick BBO crystal to produce 1.2 mJ of 402 nm light. This light is focused with a 1 m focusing lens into a semi-infinite gas cell to drive high harmonic generation (HHG). The HHG cell is filled with ~5 torr of krypton. The residual driving light is filtered out with a pair of polished silicon substrates aligned at Brewster's angle for the 402 nm fundamental, followed by a 200 nm Sn filter. Additionally, the Sn acts as a band pass filter to isolate the 7th harmonic. The probe arm is routed to a computer-controlled delay stage, which is used to vary the pump-probe temporal delay. A 500 µm thick BBO is used to generate a 402 nm UV probe beam. The pump and probe beams are recombined via an annular mirror and

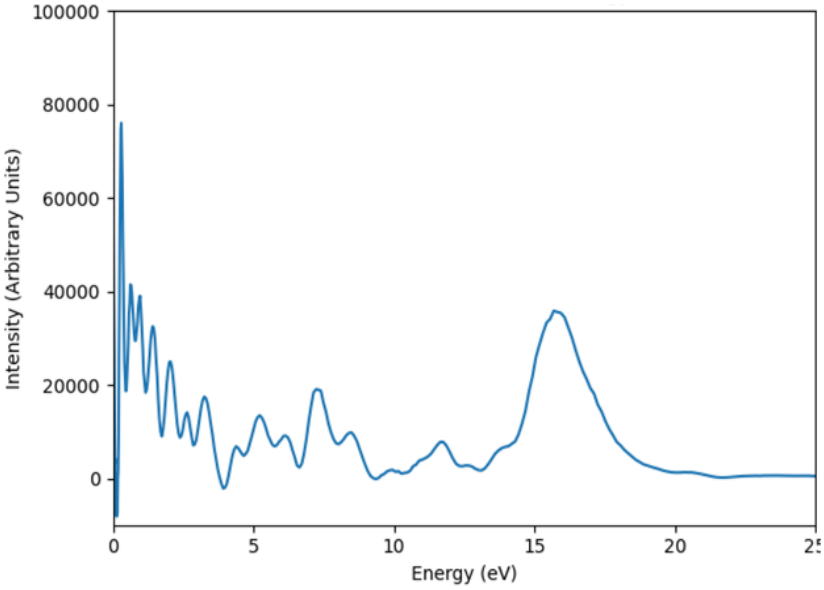

Figure 4.2. Representative static photoelectron spectrum resultant of multiphoton absorption in lower droplet absorption feature, with characteristic resonant ICD signal high electron kinetic energies.

focused into the interaction region with a nominal 0.5 m focal length multilayer mirror, where they intersect the helium droplet jet. The resultant photoelectrons are measured via a velocity map imaging (VMI) spectrometer as a function of pump-probe time delay. For intensity-dependent ion yield measurements, the above setup is utilized excluding the probe beam arm. A waveplate and polarizer are used in the pump beam arm before the BBO to control the intensity of the XUV, which is measured via a XUV photodiode after the interaction region. The polarity of the electrostatic optics is reversed to achieve ion imaging in place of electron imaging.

4.3 Results

4.3.1 Static Photoelectron Spectrum

To analyze the photoelectron images, an implementation of pBASEX is used to perform the inverse Abel transform. In order to measure kinetic energies up to 20 eV, two pairs of deflector plates in the drift tube of the VMI spectrometer are used to walk the center of the VMI image off the center of the detector, allowing for a full quadrant up to 20 eV, which can be used for the inverse Abel transform after complementing the recorded image with 3 copies that are flipped along one or two axes to recreate the complete photoelectron image. Photoelectron spectra of argon and krypton are used to calibrate the detector and to verify that the imaging conditions are preserved. The uncertainty in electron kinetic energy at 20 eV is (± 0.6 eV), based on the calibration.

First, we will look at the static, pump only photoelectron spectrum. An example photoelectron spectrum is shown in Figure 4.2. The XUV photon energy is centered on the lower helium droplet absorption feature at 21.6 eV with a bandwidth of 400 meV. The broad, high

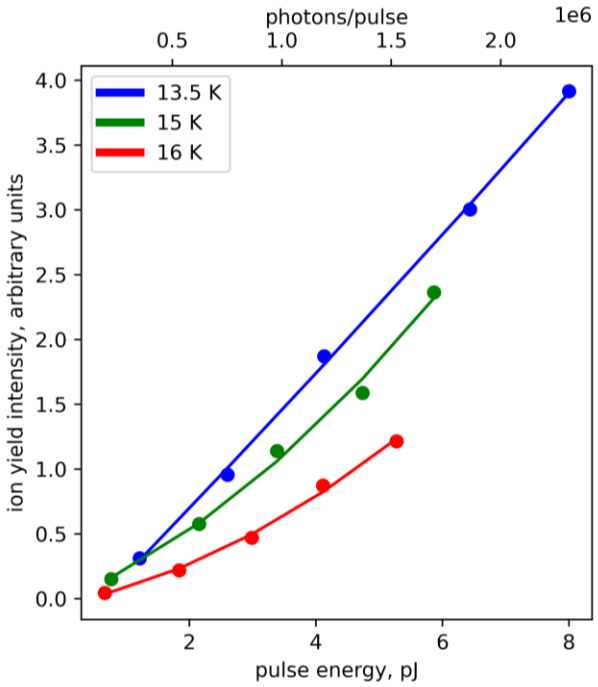

Figure 4.3. Ion yield as a function of XUV intensity for three droplet nozzle temperatures, with blue corresponding to 13.5 K, green corresponding to 15 K, and red corresponding to 16 K.

.

kinetic energy feature spanning ~14-19 eV is consistent with resonant ICD between two excited He* atoms, He* + He* → He + He^+, with the bandwidth of the ICD feature (~ 2.5 eV FWHM) exceeding the XUV bandwidth by a factor of ~ 6. All features below ~14 eV are considered artifacts from the pBASEX transformation. [78].

4.3.2 Intensity Dependent Ion Yield

Relative ion yields are measured as a function of XUV flux, at three different droplet source conditions (Figure 4.3). Normal VMI conditions were used, with all ions produced being measured on the detector. For a fixed 80 bar backing pressure, the nozzle temperature was varied between 16 K (red), 15 K (green), and 13.5 K (blue), resulting in ~10^4, 10^5, and 10^6 atoms/ droplet, respectively. The corresponding droplet radii are ~5, 10 and 20 nm. The XUV pulse energy was varied from 1 to 8 pJ. With decreasing nozzle temperature, the intensity dependence trends from quadratic to linear. The linear and quadratic coefficients for each trend are:

Nozzle T, K	a	b
16	0.027	0.101
15	0.032	0.209
13.5	0.003	0.499

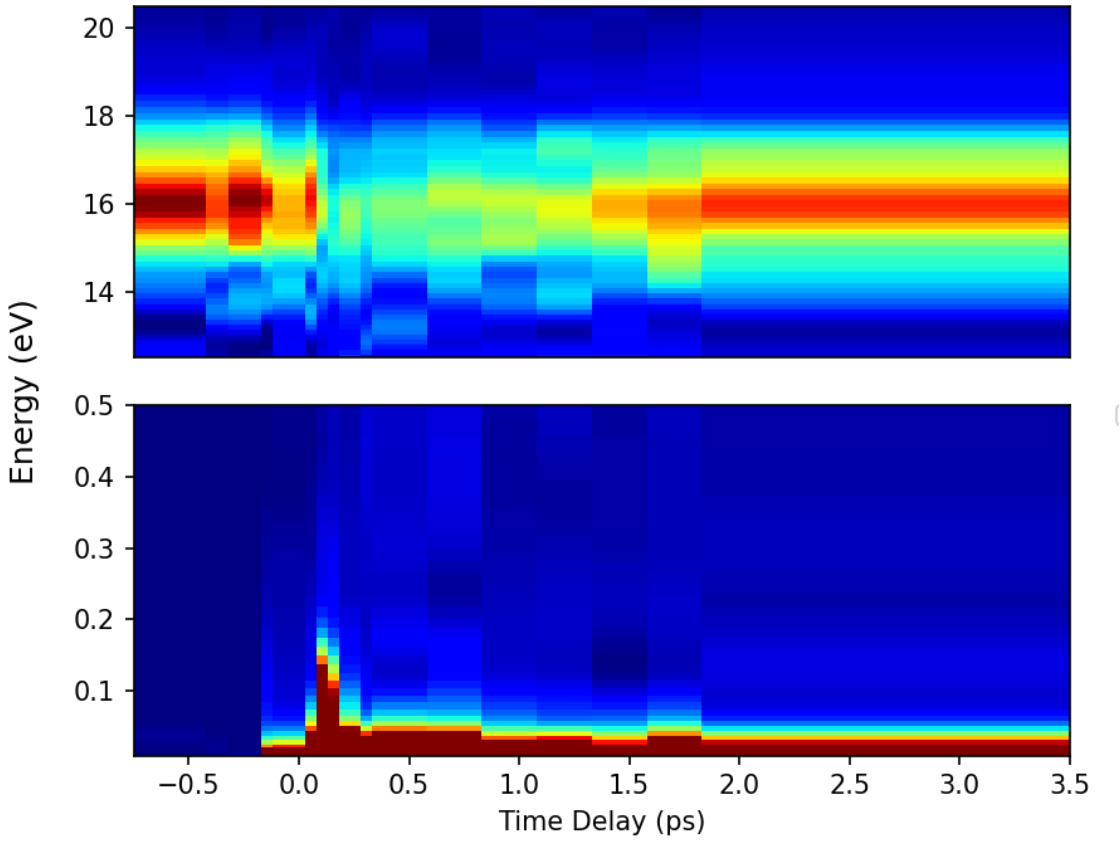

Figure 4.4 Photoelectron spectra as a function of pump -probe time delay. The top panel is centered around the ICD feature and the bottom panel is zoomed in on the low kinetic energy signal produced by the probe pulse. This is for 5 pJ of XUV, with a 14 K droplet source nozzle temperature.

for fits to $I(E) = a \cdot E^2 + b \cdot E + c$, where I is the ion intensity, E the pulse energy in pJ, and a, b, c are free fit parameters. For each XUV intensity, the droplet source was blocked and ion yield from background gases (H_2, N_2 and H_2O) with IPs lower than the photon energy were measured. This background yield was linear with XUV flux, confirming a linear detector response. Given that other droplet relaxation mechanisms in the lower absorption feature do not result in ionization and we exclusively observe the ICD feature in the photoelectron spectra, we attribute the detected ion yield exclusively to He^+ formation from ICD.

4.3.3 Time-Resolved Photoelectron Spectra

Time dependent photoelectron spectra were measured with a 21.6 eV XUV pump pulse, as was described in section 4.3.1, and a UV probe pulse at a droplet nozzle temperature of 14 K. The photoelectron spectra are plotted as a function of pump-probe time delay in a false color plot as show in Figure 4.4. In the figure, the upper panel is centered around the high kinetic energy ICD

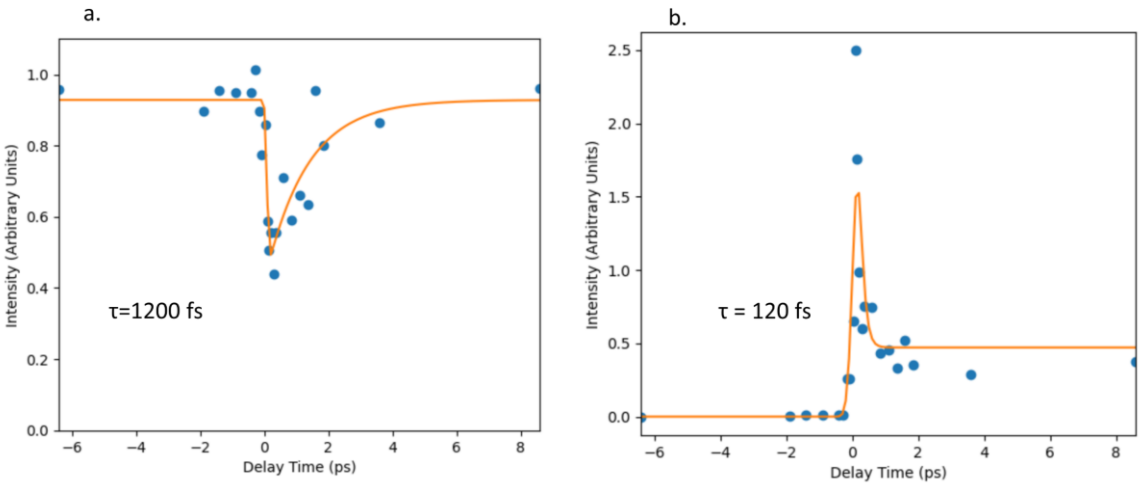

Figure 4.5. Intensity dependence of a) the ICD feature, integrated from 14-18.2 eV and b) the lower absorption feature, integrated from 0-0.2 eV

feature, as was discussed in 4.3.1, while the lower panel zooms in on a low kinetic energy window. At negative times, when the 400 nm probe pulse arrives before the XUV pump pulse, the only feature in the photoelectron spectrum is the ICD feature, as the droplet is transparent to the UV probe, thus it is effectively a pump only signal. Near zero pump-probe delay (t_0), the ICD signal depletes concurrently with the rise of a low kinetic energy feature that peaks at 0.1 eV, spanning from 0 – 0.2 eV. We note that the time-dependent low kinetic energy feature is distinct from the transform induced artifact as it is several orders of magnitude more intense and can be seen in the raw photoelectron images. As the ICD feature recovers with increasing pump-probe delay, the low kinetic feature rapidly relaxes to a lower kinetic energy or ZEKE (zero electron kinetic energy) signal, with the feature maximum less than 0.05 eV. While the ICD intensity ultimately returns to its original intensity, the low kinetic energy signal persists for at least ~600 ps. In Figure 4.5a, the intensity of the ICD feature, integrated from 14 – 18.2 eV, is plotted as a function of pump-probe time delay. The same is done for the low kinetic energy feature, integrated from 0.05 eV, shown in Figure 4.5b. The low kinetic energy feature decays to the plateau more rapidly than the ICD feature recovers.

4.4 Analysis

4.4.1 Estimating absorption in the droplet

To understand the droplet size and XUV intensity dependence of the total ion yield, we consider the photon absorption across the droplet. Because the atomic helium 2p resonance has a large absorption cross section (25 Mb [13]), it is necessary to take beam propagation effects inside the droplet into account. In other words, if the droplet is sufficiently large, the atoms on the front side of the droplet where the XUV beam enters will see a higher light intensity than the ones on back side where the light exits, because the XUV will be appreciably absorbed as it travels through the droplet. To estimate absorption across the droplet, Beer's law absorption is applied to droplet, assuming the droplet is a sphere. The attenuation of the photon flux is dependent on the pathlength through the sphere. To match experimental conditions, the initial photon flux, F_0, is defined as

$N_{photons}/A$ where the number of photons $N_{photons}$ is determined with a photodiode measurement and the area A is approximated to be 10 μm^2. To estimate the focal area, the XUV beam size is measured by imaging the beam upstream of the final focusing mirror, so that the divergence may be calculated. From the divergence, the beam size at the focusing mirror is estimated. Using a Gaussian beam approximation, the focus is then calculated from the 0.5 multilayer focal length. The attenuation $Q(l)=F_0-F(l)$ of the initial photon flux F_0 for a differential interaction area dA (see illustration in Figure 4.6a) can be expressed as:

$$Q(l) \cdot dA = [F_0 - F(l)] \cdot dA = F_0\left[1 - e^{-\sigma_{He,2p} n_{LHe} l}\right] \cdot dA \tag{4.1}$$

where $\sigma_{He,2p}$ is the absorption cross section of 2p in helium, n_{LHe} is the number density of liquid helium (22 nm^{-3} [93]), and $l = 2 \cdot \sqrt{R_0^2 - x^2 - y^2}$ is the pathlength the beam travels through the droplet for a particular entrance point (Fig. 4.5a). The total number of absorbed photons is then estimated by integrating across the entirety of the sphere. This is done by numerical integration using N surface elements that are distributed across the surface such that they provide a homogeneous sampling of the droplet's geometrical cross section within the XUV beam. The results are shown in Figure 4.6b for droplets containing 10^4 (red), 10^5 (green), and 10^6 (blue) atoms. This color size dependent color scheme corresponds with the one used in Figure 4.3. The attenuation of the XUV across the droplet is estimated to be ~30%, ~50%, and ~75% for a droplet with 10^4, 10^5, and 10^6 atoms respectively. Alternatively, in Figure 4.5c, the percentage of excited helium atoms is shown. For the smallest droplet size, 10^4 atoms, the percent excited is approximately equal to the probability of excitation based on the initial flux, i.e., $F_0 \cdot \sigma_{He,2p}$, as indicated by the dashed line in Figure 4.6c. In other words, the photon flux is weakly attenuated across the smallest droplet size. Excitations are likely homogeneously distributed throughout the droplet. As the size increases, for a given flux, the percent excited decreases relative to the initial excitation probability. This would likely mean a higher excitation density on the side of the droplet nearest the incoming XUV pulse, as compared with the far side of the droplet.

4.4.2 Time-Resolved Analysis

The intensities of the high KE feature (14-18.2 eV) and the low kinetic energy feature (0-0.2 eV) are integrated and analyzed as a function of pump-probe delay to extract the characteristic timescales of the feature dynamics. The ICD feature transient can be fit with an exponential decay. As such, we can model this as the product of a Heaviside step function and an exponential decay convolved with a Gaussian corresponding to the cross correlation of the pump and probe:

$$D_x(t) = B \cdot \theta_H(t - t_0) \cdot e^{-(t-t_0)/\tau} * e^{-\frac{(t-t_0)^2}{2\sigma^2}} = C \cdot e^{-(t-t_0)/\tau} \cdot \left(1 + \mathrm{erf}\left(\frac{t-t_0-\sigma^2/\tau}{\sqrt{2}\sigma}\right)\right) \tag{4.2}$$

so that the ICD intensity is described by:

$$I_{ICD}(t) = D_{ICD} \tag{4.3}$$

Because the low kinetic energy feature plateaus at a nonzero baseline, it is necessary to add an additional term. We choose the convolution of a Gaussian with a Heaviside step function, which is expressed as:

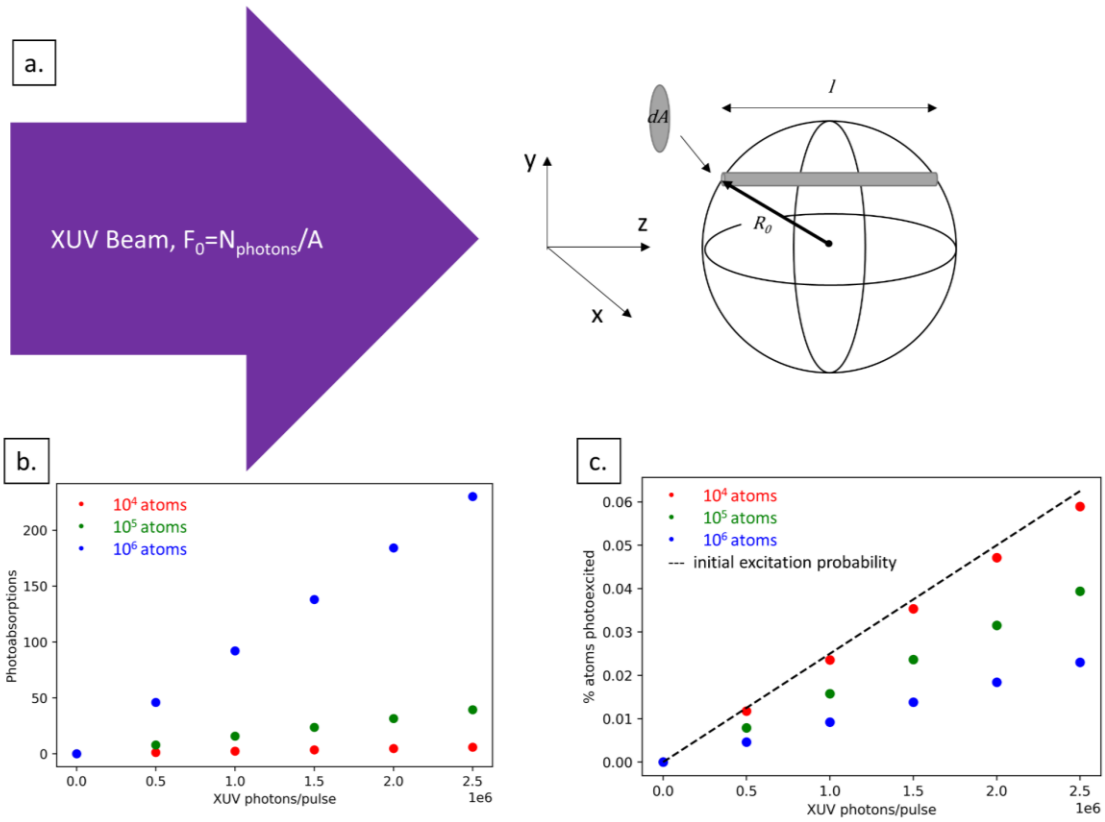

Figure 4.6. Summary of estimation of photoabsorptions based on Beer's Law absorption profile and attenuation of the beam as it travels through the droplet. a) illustrates how the droplet's shape is used to account for absorption b) total number of photoaborptions as a function of XUV photons/ pulse and as a function of droplet size and c) the percentage of atoms excited as across intensity and size conditions, as well as the probability of excitation of a single atom based on the initial flux, across all intensities consider. The data points are colored according to the corresponding number of atoms, based on nozzle conditions from ion yield measurements in Figure 4.3, with the same color scheme used.

$$P_x(t) = A \cdot \theta_H(t - t_0) * \frac{1}{\sigma\sqrt{2\pi}} e^{-\frac{(t-t_0)^2}{2\sigma^2}} = A \cdot \frac{1}{2}\left(1 + \mathrm{erf}\left(\frac{t-t_0}{\sqrt{2}\sigma}\right)\right). \quad (4.4)$$

Thus, the low kinetic energy feature is fit to:

$$I_{LE}(t) = D_{LE}(t) + P_{LE}(t) \quad (4.5)$$

Fits are shown in Figure 4.5. The ICD feature recovers with a characteristic timescale of 1200 ± 400 fs, while the low kinetic energy feature decays to a plateau within 120 ± 60 fs.

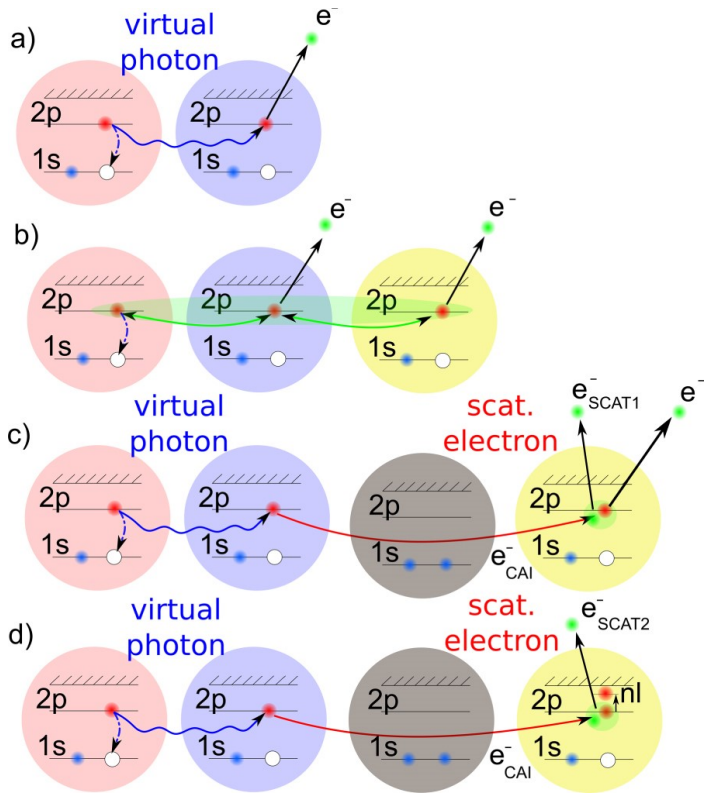

Figure 4.7 a) ICD interaction between 2 excited atoms, b) interaction between 3 excited atoms, c) and d) possible inelastic pathways that happen due to collective autoionization. Reprinted figure with permission from [35].

4.5 Discussion

Previous studies on ICD and CAI following excitation into the lower absorption feature were performed with an FEL light source. Figure 4.7 illustrates the ICD interaction between two excited helium atoms, as well as the inelastic pathways an electron may lose further energy due to the interaction between at least three excited atoms [86]. Measurements include ion yield intensity dependence [87], intensity dependence of the photoelectron spectrum [86], and time dependence of the ICD photoelectron signal [88]. Photoelectron measurements reveal at 5×10^9 W/cm^2 that the photoelectron spectrum has a pronounced high kinetic ICD feature and a low kinetic energy feature resulting from CAI. As the XUV intensity increases to 2.6×10^{10} W/cm^2, the distinct ICD feature is no longer present, with the signal shifting to lower, broader kinetic energy signal. At the highest intensities 8.6×10^{12} W/cm^2, only low kinetic energy electrons are observed. Overall, with increasing excitation density, the inelastic effects from CAI are increasingly dominant. Ion yield intensity dependent measurements are performed in the regime of partial saturation of the 2p absorption feature, in which CAI is expected to occur, revealing that the ion yield in this regime

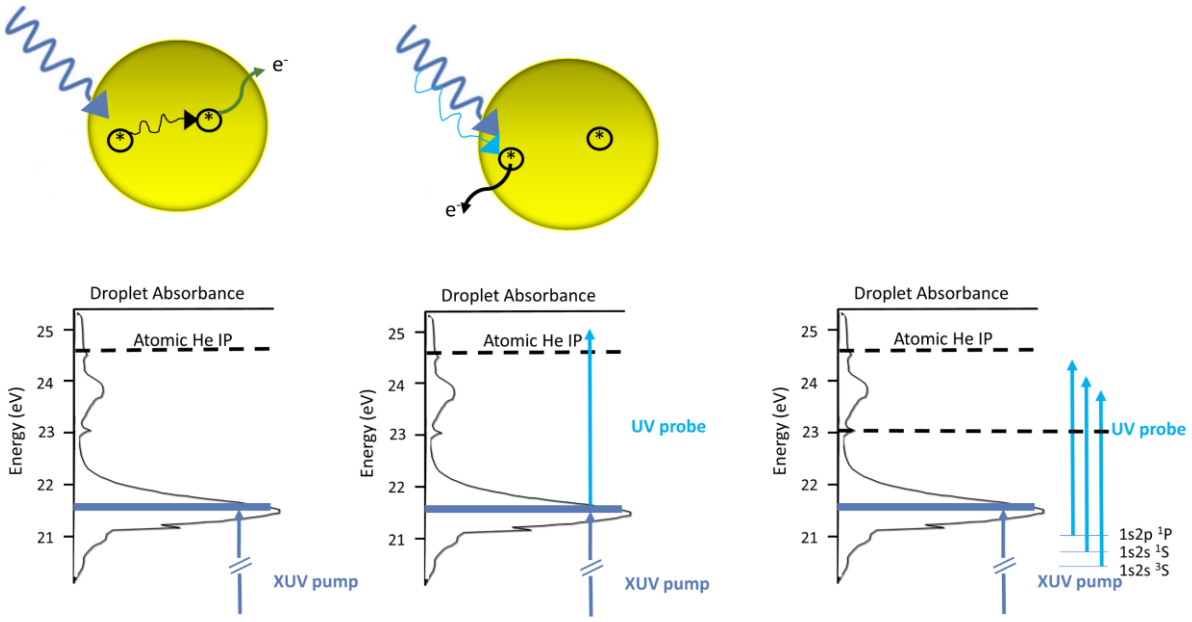

Figure 4.8 Illustration of sequential role of XUV pump and UV probe. Multiphoton absorption into the lower feature leads to ICD between two excited helium atoms. At early times the UV probe serves to ionize out of the delocalized excited state at 21.6 eV. At later times, as the droplet relaxes, the probe prevents ICD by exciting from the lower to the upper absorption feature.

scales with intensity, I, as $I^{0.6}$. Time-dependent photoelectron measurements were performed in the regime of 0.1 – 1% excited atoms in the droplet, so that there is still a distinctive ICD signal. However, static photoelectron spectra in this regime also contain a low kinetic energy feature. ICD lifetimes in the study performed by LaForge *et al.* range from ~900 fs to 400 fs, with increasing excitation density. In that study, aside from the highest flux case, the ICD electron yield does not recover to its baseline intensity, indicating that some excited helium atoms undergo ICD on longer timescales [88].

The measurements presented herein are performed under complementary conditions to these previous studies [88]. Based on the estimates from the absorption model described in section 4.4.1, ion yield measurements are performed over excitation percentages from ~0.01 - 0.1%, depending on the droplet size and XUV flux. Time dependent results presented herein are performed on droplets that are estimated to be ~ 0.01% excited, two orders of magnitude lower than the previous time-dependent studies. As a consequence of the lower XUV intensities, excitation densities are sufficiently low such that we exclusively induce resonant ICD, with no evidence of CAI (indicated by a lack of low kinetic energy electron feature in the static spectra). Thus, our ion yield measurements are, to the best of our knowledge, the first ion yield intensity-dependent measurements that are exclusively sensitive to ICD. Interestingly, in our time-dependent data, we also observe a ~1 ps lifetime, despite 2 orders of magnitude lower excitation density. In contrast to previous measurements, however, we observe the ICD signal fully recovers to its baseline intensity.

The results from the time-resolved photoelectron spectra will be explored in the following. The XUV pump leads to multiphoton absorption in the 2p band of the droplet. The high kinetic energy electron feature is the result of ICD between two excited He* atoms. The dynamic trends in the photoelectron spectra are consistent with the following role of the UV probe. Initially, at t_0, the probe can ionize from the delocalized excited state of the droplet, removing excited population from the lower absorption feature. The resulting contrast kinetic energy of $h\nu_{XUV} + h\nu_{UV} - IP_{helium}$ = 0.1 eV is consistent with the low-energy photoelectron feature at early times (see Figure 4.3). However, as seen in Figures 4.3 and 4.4b, the low kinetic energy feature relaxes faster than the ICD rises back in. The ultrafast relaxation to ZEKE with very little bandwidth, is consistent with ultrafast relaxation within the droplet 2p band, potentially resulting in the previously observed atomic 2p and 2s states, which lie lower than the initial excitation energy. The UV probe has insufficient energy to exceed the atomic IP from these states. However, the UV probe may act to promote excitation from states in the lower to those in the upper absorption feature. Droplet excitations above 23 eV result in the production of ZEKE electrons, as has been observed in numerous experimental studies [[14], [29]]. Furthermore, Kornilov *et al.* observed that is possible to excite from the lower to the upper droplet absorption feature with a 785 nm NIR probe. We propose a similar mechanism to explain the persistent ZEKE signal. The role of the XUV pump and UV probe are illustrated in Figure 4.8.

An important observation in the time-resolved measurements is that the ZEKE signal persists on timescales up to at least 600 ps, while the ICD signal returns to its original intensity within ~1 ps. This indicates that a nonzero portion of the excited population does not relax via ICD and thus that it is not perfectly efficient. This is comparable to the timescales observed in previous work with substantially higher photon fluxes and excitation densities. While building a comprehensive model to explain our results is ongoing, preliminary thoughts will be presented. It is established that void bubbles can form around He* atoms in the bulk droplet environment. LaForge *et. al.* have shown that the merging of two bubbles brings two He* in close proximity, greatly increasing the efficiency of ICD as a decay mechanism [88]. It's possible that in this low excitation density regime, initially, the excitation density is sufficiently high so that a fraction of the excited atoms are close enough to merge into a single bubble and undergo ICD. However, as this occurs, the density of excited atoms decreases and below some threshold, ICD will no longer occur, and the remaining excited atoms behave according to the relaxation dynamics observed in the single photon absorption regime. In other words, those excited atoms that are, coincidentally, close enough to one another that their voids merge, decay by ICD, but at some point, the remaining excited atoms are, on average, too far away from each other to meet and undergo ICD. Eventually, the bubbles containing these remaining excited atoms may eventually travel to the surface of the droplet and the excited atoms will be ejected from the droplet. This picture may have increased complexity due to the nonlinear excitation density profile, as described in section 4.4. With a 14 K nozzle, the droplets will be sufficiently large, so that front side of the droplet where the XUV beam enters will experience a higher flux than on the back side.

The ICD ion yield intensity dependence offers complementary information and may be useful in understanding the relationship between ICD efficiency and excitation density. The ion yield has either a quadratic or linear relationship, depending on the average droplet size. Smaller droplets, in which the XUV beam is weakly attenuated, should have an approximately homogenous excitation distribution. In this case, we observe a quadratic relationship between XUV intensity and ion yield. In contrast, in larger droplets, with non-negligible attenuation (~75 %) and non-

homogeneous excitation densities, the relationship is linear. Another aspect of size dependence arises from the ratio of bulk to surface, which increases with increasing droplet size. Bubble formation around excited atoms in the droplet is expected to occur in the bulk of the droplet, while bubbles collapse if they try to form on the surface consequently ejecting the excited atom. Because ICD is expected to be facilitated by two bubbles merging, the distribution of excitations near the surface vs. in the bulk may be an important factor. Ongoing analysis includes accounting for the nonhomogeneous density of excitations across the droplet, as the XUV beam in attenuated, accounting for surface vs. bulk excitations, and modeling the competition between ICD and excited atom ejection.

4.6 Conclusion

In conclusion, we report on the timescale and intensity dependence of resonant ICD in helium nanodroplets, near the threshold of multiphoton absorption. This is a competitive relaxation mechanism even at relatively low excitation densities. The measured ICD lifetime with ~0.01% of the atoms in the droplet is comparable to lifetimes measured with 2 orders of magnitude higher excitation density. The full recovery of the ICD signal presents an interesting result. Complementary intensity and size dependent ion yield measurements reveal a quadratic intensity dependence in small droplets and a linear relationship in larger droplets. These results may be used to elucidate the relationship between droplet excitation density and the efficiency of resonant ICD between two excited helium atoms in the droplet.

Chapter 5

Charging and Ion Ejection Dynamics of Large Helium Nanodroplets Exposed to Intense Femtosecond Soft X-Ray Pulses

Reprinted by permission from Springer Nature Customer Service Centre GmbH: Springer Nature, Eur. Phys. J. Spec. Top., "Charging and ion ejection dynamics of large helium nanodroplets exposed to intense femtosecond soft X-ray pulses," C.A. Saladrigas, A. J. Feinberg, M. P. Ziemkiewicz, C. Bacellar, M. Bucher, C. Bernando, S. Carron, A. S. Chatterley, F.-J. Decker, K. R. Ferguson, L. Gomez, T. Gorkhover, N. A. Helvy, C. F. Jones, J. J. Kwok, A. Lutman, D. Rupp, R. M. P. Tanyag, T. Möller, D. M. Neumark, C. Bostedt, A. F. Vilesov, and O. Gessner (2021). https://doi.org/10.1140/epjs/s11734-021-00280-0
With kind permission of The European Physical Journal (EPJ).

Ion ejection from charged helium nanodroplets exposed to intense femtosecond soft x-ray (838 eV, λ = 1.48 nm) pulses is studied by single-pulse ion time-of-flight (TOF) spectroscopy in coincidence with small-angle x-ray scattering. Scattering images encode the droplet size and absolute photon flux incident on each droplet, while ion TOF spectra are used to determine the maximum ion kinetic energy, E_{kin}, of He_j^+ fragments (j= 1-4). Measurements span He_N droplet sizes between N~10^7 and 10^{10} (radii R_0 = 78-578 nm), and droplet charges between ~9×10^{-5} and ~3×10^{-3} e/atom. Conditions encompass a wide range of ionization and expansion regimes, from conditions where there is departure of all photoelectrons from the cluster, leading to pure Coulomb explosion, to substantial electron trapping by the electrostatic potential of the charged droplet, indicating the onset of hydrodynamic expansion. The unique combination of absolute x-ray intensities, droplet sizes, and ion E_{kin} on an event-by-event basis reveals a detailed picture of the correlations between the ionization conditions and the ejection dynamics of the ionic fragments. The maximum E_{kin} of He^+ is found to be governed by Coulomb repulsion from unscreened cations across all expansion regimes. The impact of ion-atom interactions resulting from the relatively low charge densities is increasingly relevant with less electron trapping. The findings are consistent with the emergence of a charged spherical shell around a quasineutral plasma core as the degree of ionization increases. The results demonstrate a complex relationship between measured ion E_{kin} and droplet ionization conditions that can only be disentangled through the use of coincident single-pulse TOF and scattering data.

5.1 Introduction

X-ray free electron lasers (FELs) generate extremely intense, coherent, ultrashort pulses that have enabled single-pulse imaging of nanoscale systems, such as clusters, viruses and quantum vortices [7], [64], [94], [95]. Interpretation of these experiments often relies on the conjecture that the pulses are sufficiently short such that the x-rays diffract before destroying the sample due to extensive ionization [58]. However, intense light—matter interactions lead to a host of complex physical processes, which can play an important role in interpretation of these experiments [94], [96]. Isolated and self-bound noble gas clusters are an excellent model system to study these processes via x-ray diffraction and the energetics of the ionization products [97]. Here, we study the charging and ion ejection dynamics in large helium nanodroplets irradiated by intense soft x-ray pulses, exploring the relationship between the degree of ionization, charge density, and maximum ion kinetic energies.

When an atomic cluster is exposed to an intense x-ray pulse, electrons are initially "outer ionized," i.e., electrons escape the cluster following photoionization [36]–[38]. The evolution of the charging process during the continued x-ray – cluster interaction depends strongly on x-ray intensity and cluster size. In one extreme, all photoionization results in outer ionization and thus, all freed electrons escape the cluster. The charged cluster then expands via Coulomb explosion as a result of the repulsion between unscreened ions [36], [37]. In the other extreme, with sufficient x-ray intensity and cluster size, the collective Coulomb potential of the cations becomes deep enough, such that the kinetic energy of photoelectrons is insufficient to escape, i.e., outer ionization is frustrated. The subsequent photoionization events result in "inner ionization", i.e., the creation of quasi-free electrons that are trapped by the Coulomb potential of the charged cluster. An early description of this process was provided by Saalmann and Rost [98]. Assuming a homogeneous charge distribution, the Coulomb potential is deepest near the cluster center and becomes shallower toward the surface. Thus, electron trapping is expected to originate at the center of the droplet and to move outwards as ionization progresses. The result is a quasineutral plasma core that grows to encompass more of the cluster as inner ionization proceeds [99]. The hot, trapped electrons begin to thermalize with the ionic cores, and the quasineutral nanoplasma expands hydrodynamically.

In reality, the expansion of charged clusters may proceed by a combination of hydrodynamic expansion and Coulomb explosion, depending on the cluster size [100], atomic species [101], and the intensity [102] and wavelength [103] of the incident radiation [104]. While an extensive body of literature exists describing strong near-infrared (NIR) light– cluster interactions [99], [101], [103], [105]–[107], x-ray– cluster interactions have only more recently been investigated, motivated by the availability of short, intense x-ray pulses provided by FELs. The evolution of large xenon clusters (~30-600 nm) exposed to FEL pulses ($h\nu$ = 91 – 850 eV) with typical intensities of ~10^{14}-10^{16} W/cm^2 has been described in terms of hydrodynamic expansion and indicate that three-body recombination plays an important role in the nanoplasma dynamics [64], [108]. Other studies on smaller xenon and argon clusters, as well as Xe-Ar mixed clusters, reveal a more complex situation in which the outer shell of a cluster may undergo Coulomb explosion, while the core forms a quasineutral nanoplasma, followed by hydrodynamic expansion [109]–[111]. Theoretical calculations predict that Ar_{923} clusters exposed to VUV (20 eV), XUV (38 eV), and soft x-ray (90 eV) pulses with the same total energy deposition exhibit a smooth transition in expansion behavior [37]. It ranges from a Coulomb explosion for soft x-rays, to hydrodynamic expansion after VUV irradiation, while the XUV-induced dynamics fall in between the two limiting cases.

Early experiments on charged clusters provided quantities, such as ion mass and/or electron energy spectra, accumulated over many pulses, and averaged over laser fluences and cluster sizes [99], [101], [105], [107]. Using ultrashort, intense light sources, measurements, such as ion TOF spectra, can be acquired on a shot-by-shot basis. Although, if only ion TOF spectra are acquired, the analysis still relies on average photon fluxes and cluster sizes. More detailed information can be obtained via coincidence measurements at X-FELs, in which both the TOF spectrum and the x-ray scattering pattern are collected for each registered event. These simultaneous measurements have previously been demonstrated on highly ionized Xe clusters in the hydrodynamic expansion regime [64], [108]. Here, we apply the same concept to study the transition between Coulomb explosion and hydrodynamic expansion regimes in more moderately ionized He nanodroplets. Helium atoms have only two electrons, both in the 1s shell. The x-ray photon energies (838 eV) used in this work are well above both the single and double ionization potential (IP) of helium (24.6 eV and 79 eV, respectively [112], [113]) and, thus, also far from any resonances. The resulting x-ray scattering patterns can be analyzed in a straightforward fashion using the Rayleigh-Gans approximation [7], [21] to determine the droplet size and the absolute single-pulse photon flux incident on the droplet. The validity of this approximation and the simplicity of the helium atom electronic structure enable an accurate determination of the incident photon flux and a relatively simple theoretical description of the charging process by photoionization, devoid of both high charge states and Auger cascades.

In this work, we monitor the interaction of single intense x-ray pulses ($h\nu$ = 838 eV, ~10^{11} photons/pulse) with individual large helium droplets (radius R_0 = 78 – 578 nm) via coincident single-pulse coherent x-ray scattering and ion TOF spectroscopy. The unique event-by-event measurements provide detailed access to droplet charging and ion ejection dynamics across a large range of ionization regimes, from nominally pure Coulomb explosion conditions well into the quasineutral nanoplasma regime. Simultaneous measurements of the absorbed number of photons, the droplet size, and the ion TOF spectrum for each event provides unprecedented detail on the degree of ionization and corresponding ion kinetic energy release of each individual droplet. Measurements span He_N droplet sizes between $N \approx 10^7$ and 10^{10}, and droplet charges between ~9×10^{-5} and ~3×10^{-3} *e*/atom. In terms of the dimensionless frustration parameter α (see below) [37], ionization conditions cover a range of α = 0.23-44.

In all ionization regimes accessible in this experiment, the observed maximum ion kinetic energy (KE_{max}) values are consistent with a theoretical model in which the ion kinetic energies are governed by a combination of Coulomb repulsion in the collective cluster potential from unscreened ions and ion-atom interactions during the expansion. In the predominantly Coulomb explosion regime (small α), screening by trapped electrons is negligible and unscreened charges are homogeneously distributed throughout the cluster. The resulting ion TOF spectra are heavily impacted by interactions of ions with neutral atoms during the expansion process, due to the relatively low overall charge density in this study. In the predominantly hydrodynamic expansion regime (large α), frustrated ionization is initiated at the droplet center and expands outward, leading to increased localization of unscreened charges near the surface of the nanoplasma with increasing α. In this regime, the fastest ions contained in the TOF spectra predominantly reflect ions originating from the surface, and their kinetic energies are well captured by a model of an expanding thin, charged spherical shell, driven by Coulomb repulsion.

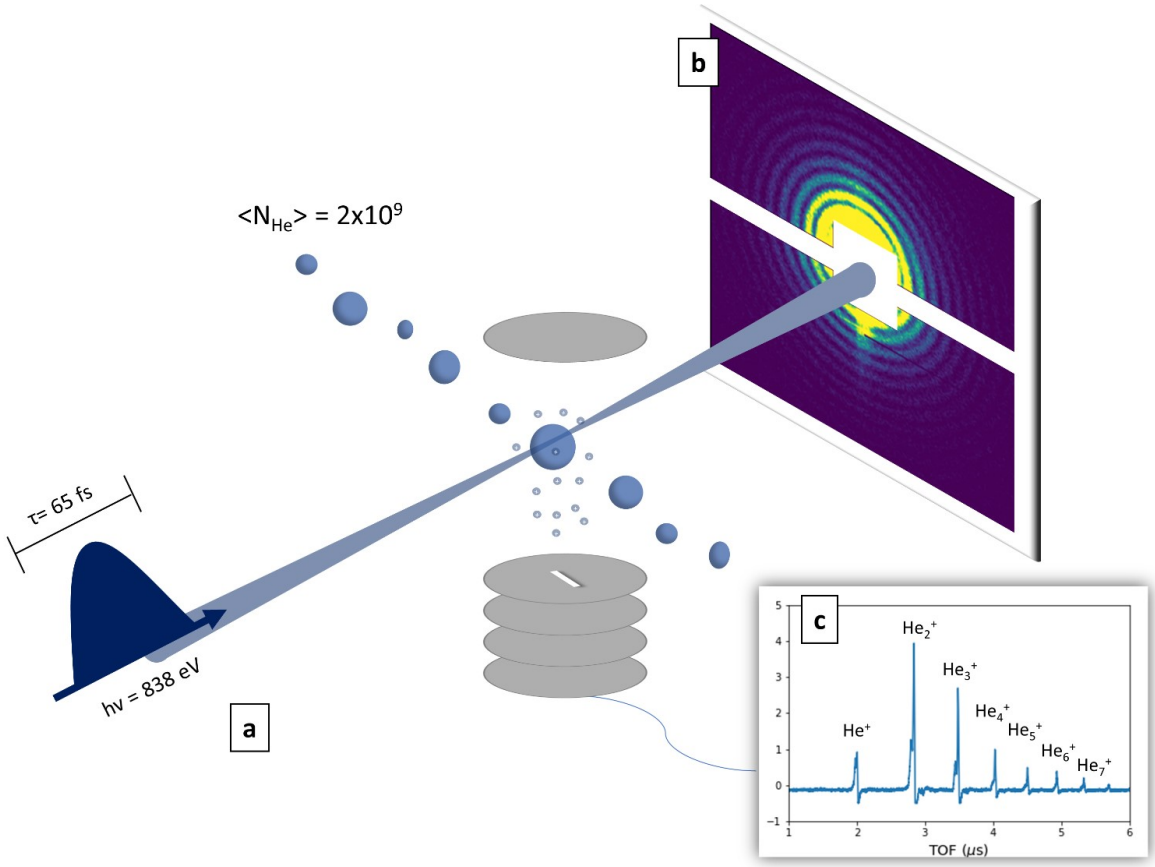

Figure 5.1. a) Diagram of experimental setup. b) Sample diffraction image. c) Coincident ion TOF spectrum.

5.2 Experiment

The experiment is conducted using the LAMP chamber at the AMO instrument of the Linac Coherent Light Source (LCLS) [80], [81], [114]. A schematic of the experiment is illustrated in Figure 5.1. A beam of helium droplets is produced upon the expansion of 99.9999% purity liquid helium into vacuum through a 5 μm nozzle cooled to 5.8 K at a backing pressure of 20 bar. The measured average He_N droplet size is $\langle N \rangle \sim 2\times10^9$, which is very close to the expectation value of $\langle N \rangle \sim 1\times10^9$ from previous measurements at same conditions [72]. The droplet beam is intersected by short x-ray pulses (~65 fs FWHM, $h\nu$ = 838 eV) that are delivered at a 120 Hz repetition rate. The x-rays are focused using a pair of KB mirrors to a nominal 2.5 μm^2 spot size in the interaction region. Based on the LCLS operating parameters and previous beamline transmission measurements, average pulse fluxes on the order of ~10^{16} W/cm^2 (~10^{23} photons/m^2) are expected in the interaction region. As described in the following, the exact values for each x-ray–cluster interaction are determined from the single-pulse scattering patterns. Scattered x-ray photons are detected with a two-panel pnCCD detector, 710 mm downstream from the x-ray focus. The active regions of the detector panels are separated by a gap of 1.5 mm and each panel has a

4.4×1.8 mm^2 gap to let the primary x-ray beam pass through. The detector records small angle x-ray scattering patterns ((q~ 2×10^{-3} – 2×10^{-2} Å^{-1}). About the interaction region, an ion TOF spectrometer [81] is aligned perpendicular to both the helium droplet and x-ray beams, detecting cations produced upon x-ray absorption. A 10 mm × 1 mm slit aperture is mounted on the ion extraction electrode and aligned perpendicular to the FEL beam to suppress detection of ionized background gas outside the FEL focus. The aperture also provides more direct access to the E_{kin} distribution of ejected cations, as TOF averaging effects due to ion emission angular distributions are greatly reduced. X-ray diffraction images (Figure 5.1b) and ion TOF spectra (Figure 5.1c) are recorded in coincidence for each detectable scattering event from a single droplet.

5.3 Results

5.3.1. Individual droplet sizes and absolute on-target photon fluxes

Over 30 minutes of data acquisition, 47 scattering images with sufficient signal for post-analysis were recorded. A typical scattering pattern is shown in Figure 5.1b. Quantitative analysis of the single-pulse x-ray scattering patterns using the Rayleigh-Gans approximation for optically thin targets [7], [21] provides direct access to both the size of individual droplets as well as the photon flux interacting with them. For small angle scattering in the Rayleigh-Gans regime, the ring spacing in scattering patterns such as in Figure 5.1b can be approximated by $\Delta\Theta \approx \frac{\lambda}{2R_0}$, where λ is the x-ray wavelength, R_0 the droplet radius and $\Delta\Theta$ is the difference in scattering angles between rings. Fits to an analytic expression for the diffraction intensity, as described in Gomez *et al.,* [7] are used to derive the droplet radius. Based on the number density of liquid ^{4}He at a temperature of 0.4 K, $n_{LHe} = 2.18\times10^{28}$ m^{-3} [93], the number of atoms in the droplet, N, is determined from the radius by $N = \frac{4}{3}\pi R_0^3 n_{LHe}$ [115]. It has previously been observed that a fraction of droplets in beam expansions have spheroidal shapes due to centrifugal distortion [26], [116]. However, consistent with previous measurements in comparable size regimes [26], droplets studied here have an average aspect ratio of 1.05 and, for the purpose of this work, are approximated as spheres.

The flux F (photons/m^2) of the x-ray pulse interacting with the droplet is obtained from the total number of scattered photons, which is given by

$$I_{total} = \frac{8\pi^3 R_0^4 |n-1|^2}{\lambda^2} F \tag{5.1}$$

where n is the complex refractive index of liquid helium, $n = 1-4.32\times10^{-5}+1.75\times10^{-7}i$ [7], [20]. The value of n is obtained from the atomic scattering factors for He atoms [117] of $f_1^0 = 2.02$ and $f_2^0 = 8.16\times10^{-3}$ at 838 eV (λ = 1.5 nm), the number density of liquid helium of n_{LHe}, and the classical electron radius $r_e = 2.818\times10^{-15}$ m according to [20]:

$$n = 1 - \frac{n_{LHe} r_e \lambda^2 (f_1^0 - i f_2^0)}{2\pi} \tag{5.2}$$

The value of I_{total} is obtained by scaling the total scattering intensity from a droplet with radius R_0 to the range of observable scattering vectors, which excludes the central hole in the detector and the gap between the CCD plates. The scattered intensity is expressed in photon units

using the calibrated detector single photon response. The number of absorbed photons is obtained as follows [20]:

$$N_{abs} = 2r_e\lambda \times f_2^0 \frac{4\pi R_0^3}{3} n_{LHe} F \tag{5.3}$$

In this work, droplet radii range from R_0=78 nm – 578 nm, and the photon flux ranges from F=1.3×10^{21} to 5.7×10^{22} photons/m^2. The droplet radius is determined within ~5% and the photon flux is accurate within ~20% with the uncertainty arising from approximating the droplets as spheres, the detector noise subtraction, and from using a nominal detector signal-to-photon count conversion factor. This so-called analog-to-digital unit (ADU) is affected by parameters such as the detector gain and quantum efficiency and may principally vary over the detector lifetime. The variation in photon flux mostly results from the spatial distribution of the detected droplets with respect to the FEL beam axis. Some additional variation originates from the pulse-to-pulse intensity fluctuations of the FEL.

At a photon energy of 838 eV, photoabsorption leads to photoionization with the number of absorption events given by Equation (5.3). We neglect single-photon double ionization events in these estimates, since the relative cross section for double vs. single ionization at 838 eV photon energy is less than 3% [113]. As such, the number of ions resulting from photoionization, N_{ion}, is equal to N_{abs}. Note that N_{ion} does not necessarily correspond to the number of electrons leaving the droplet. Additionally, N_{ion} does not include ions resulting from secondary ionization.

5.3.2. Helium cation TOF spectra

Cation TOF spectra provide information about the relative abundance of different cation species produced in the x- ray – cluster interaction, as well as the ion kinetic energies. An example cation cluster spectrum is shown in Figure 5.1c. The leftmost (i.e., shortest TOF) feature corresponds to the singly charged He^+ atomic ions, with the features following at longer times of flight corresponding to He_j^+ clusters with j>1. Numerical ion trajectory simulations (SIMION®) are used to convert from TOF to initial ion kinetic energy in the interaction region. The analysis is focused on the short-TOF edge of the peaks, corresponding to the maximum ion kinetic energy, since many peaks exhibit strong saturation effects at longer TOF. Additionally, the particular layout and operating voltages of the TOF spectrometer leads to the unusual situation where almost all ions with nonzero initial kinetic energy, independent of their emission direction, arrive at the detector before the zero kinetic energy ions. Even most ions originally ejected away from the detector are accelerated such that they overtake the zero kinetic energy ions in the drift region of the spectrometer and their TOF signals overlap with ions emitted toward the detector. Thus, the recorded TOF spectra were calibrated by using the longest TOFs of the He_j^+, j=1,2,...,8 signals to identify the E_{kin} = 0 positions of the different mass peaks. The precision of this method was maximized by using the weakest intensity hits that contained the required mass peaks, which circumvents potential issues with signal modulations at the long-TOF peak edges in the more intense hits caused by electronic ringing. Due to the overlap of signals from ions ejected both toward and away from the detector, it is rather challenging to recover the complete ion kinetic energy distribution from the TOF signals. However, ions ejected toward the detector with the highest kinetic energies are always the first to arrive at the detector. Therefore, E_{kin}^{max} can be faithfully recovered from the shortest TOF.

Uncertainty in determining E_{kin}^{max} arising from electronic signal noise dominates for weaker hits (and correspondingly for ion features with smaller E_{kin}^{max}). Systematic uncertainties arising from the limited precision in locating the interaction region with respect to the center of the ion TOF spectrometer dominate for strong hits and higher E_{kin}^{max}. In particular, for He^+, which will be the focus of the discussion, the smallest E_{kin}^{max} values are determined within 20% and the largest within 6% uncertainty. E_{kin}^{max} is determined for He^+, as well as He_2^+, He_3^+ and He_4^+ when present. For example, the E_{kin}^{max} corresponding to the TOF spectrum in Figure 5.1c are 103, 123, 24, and 8 eV, respectively, for the four ion species.

5.3.3. Size- and Charge-Dependent TOF spectra

Figure 5.2 illustrates some of the information revealed by the coincidence measurements of single-pulse TOF spectra and scattering images. The ion TOF spectra in Figure 5.2 are grouped into four panels according to the droplet size (horizontal axis). Panels a, b, c, d correspond to droplets consisting of ~10^7, ~10^8, ~10^9 and ~10^{10} atoms, respectively. The respective color codes of black, blue, green, and red, are also used in Figure 5.3-5.8 to identify droplet sizes associated with the data points. In each panel, the TOF spectra are offset corresponding to the number of ionization events per atom of the droplet, N_{ion}/N (vertical axis). In each spectrum, the peak with the smallest TOF (~2 μs) corresponds to He^+ ions, followed by He_j^+ fragments with j=2,3,4... with increasing TOF. All spectra in Figure 5.2 are plotted using the same scale.

Several trends are readily apparent in Figure 5.2. As the droplet size increases for a given average charge per atom (i.e., for constant photon flux), the corresponding TOF spectra extend to increasingly larger helium cation clusters. For example, for $N_{ion}/N \approx 2-3 \times 10^{-4}$, the largest detected He_j^+ cluster size increases from j=3 for N~10^7 to j=8 for N~10^{10}. Conversely, within a given size regime, the He_j^+ size distribution shifts from larger to smaller values of n with increasing average charge. In particular, at $N_{ion}/N \gtrsim 1.8 \times 10^{-3}$ e/atom no $He_{j\geq 3}^+$ features are observed whereas the monomer peak becomes the most intense spectral feature for all droplet sizes. Additionally, a further increase in N_{ion}/N leads to a broadening of the $He_{j=1,2}^+$ peaks towards shorter times of flight, corresponding to an increase in the ion kinetic energy. Note that we do not observe any signatures of He^{++} fragments in the TOF spectra, which would be expected at TOF ~1.4 μs.

5.4. Analysis

5.4.1. Cluster charging and degree of frustrated ionization

As an intense x-ray pulse passes through the target, the series of ionization events leads to a concomitant increase of the collective Coulomb potential of all ions in the droplet. Assuming a homogeneous distribution of ionization events [104], the cluster Coulomb potential experienced by an electron can be described by

$$V_{Coul} = \begin{cases} -\frac{e}{4\pi\varepsilon_0}\frac{N_{eff}}{2R_0}\left(3-\frac{r^2}{R_0^2}\right), & r < R_0 \\ -\frac{e}{4\pi\varepsilon_0}\frac{N_{eff}}{r}, & r \geq R_0 \end{cases} . \tag{5.4}$$

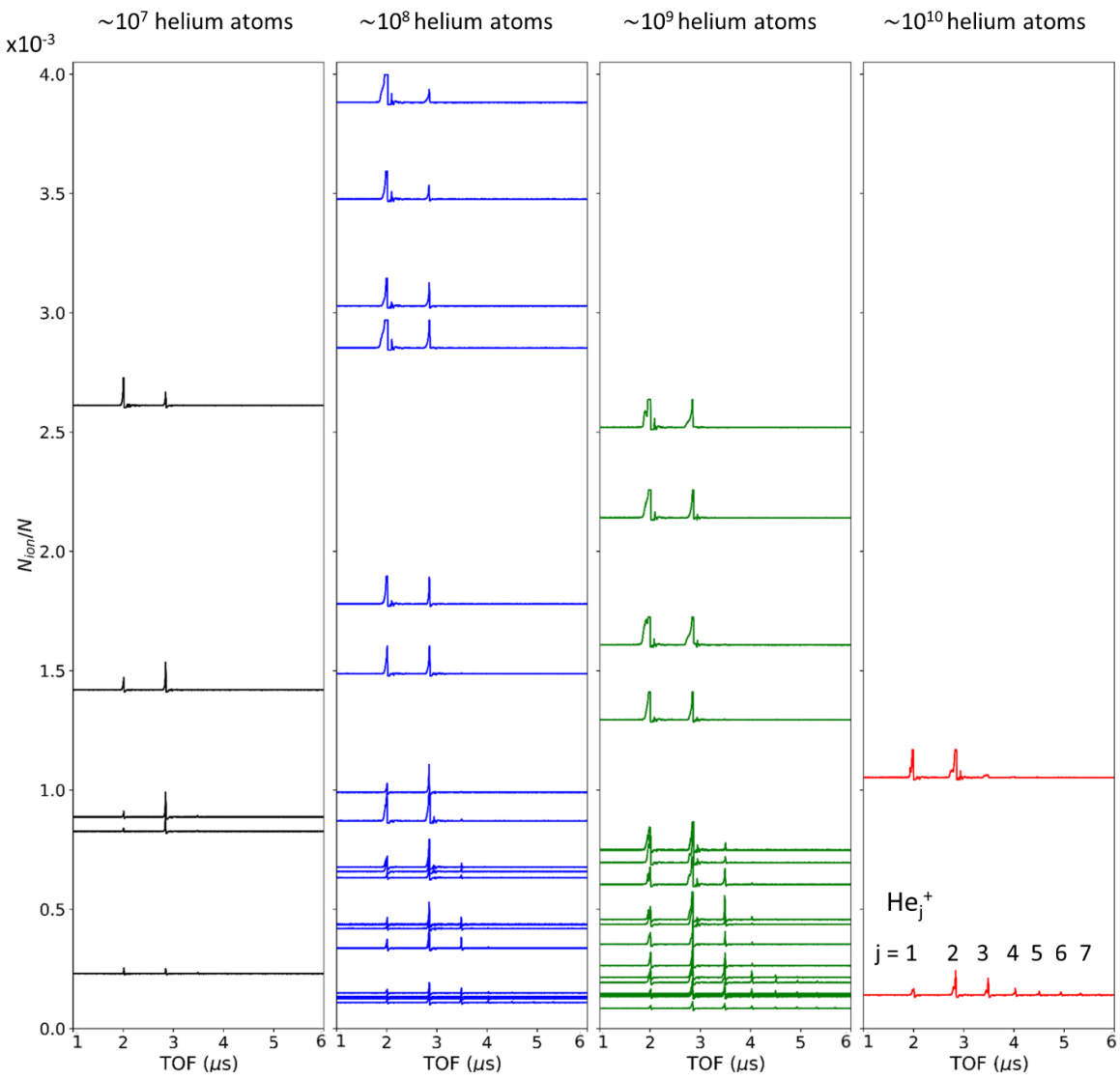

Figure 5.2. Helium droplet ion TOF spectra are vertically sorted by the number of photo-generated ions, normalized to the number of helium atoms. Panels a-d feature TOF spectra obtained in droplets of different sizes (~10^7, 10^8, 10^9 and 10^{10} atoms). The size regimes are further indicated by the colors of the TOF spectra, and the same color code is used in all subsequent figures.

Here, e is the elementary charge, ε_0 is the permittivity of free space, and r corresponds to the distance from the droplet's center. N_{eff} is the net number of charges contributing to the Coulomb potential as described in the following. According to Equation (5.4), the kinetic energy of the primary photoelectrons, $E_{kin}(e^-)=h\nu\text{-IP} \lesssim 813.4$ eV (IP: atomic ionization potential), will be insufficient to overcome the cluster Coulomb potential if the droplet's charge reaches a critical value. At this point, the locally freed electrons will be trapped as quasi-free electrons and begin to

form a nanoplasma. The potential in Equation (5.4) is deepest at $r = 0$. Thus, frustration of ionization is expected to commence at the droplet center and expand outward with increasing degree of ionization during the passage of a sufficiently intense x-ray pulse through the target. With the onset of photoelectron trapping, the effective number of ions contributing to the Coulomb potential, i.e., the net droplet charge, is smaller than the total number of created ions, $N_{eff} < N_{ion}$, due to partial screening of the ionic background by trapped electrons. Note that the term for $r < R_0$ in Equation (5.4) is nominally only valid for conditions before the onset of frustration, as trapped electrons will move towards the center of the charged droplet and therefore the net charge distribution is no longer homogeneous [104]. In addition, this discussion neglects any secondary ionization events.

The degree of ionization frustration is quantified by the dimensionless frustration parameter [37]

$$\alpha = \frac{N_{ion}}{N_{frust}}\,, \tag{5.5}$$

whereby N_{frust} is the effective number of droplet charges needed to completely frustrate outer ionization across the entire droplet. N_{frust} can be determined by equating the maximum kinetic energy $E_{kin}(e^-) = 813.4$ eV of an electron to its Coulomb energy at the surface of a cluster with radius R_0, according to Equation (5.4) leading to

$$N_{frust} = \frac{4\pi\varepsilon_0}{e^2} E_{kin}(e^-) R_0 \approx 565 \cdot R_0(nm)\ . \tag{5.6}$$

From equations. (5.4) -(5.6) it follows that frustrated ionization sets in for $\alpha = 2/3$ and full frustration is reached at $\alpha \gtrsim 1$, after which all additional photon absorption leads to inner ionization. Note that α needs to be somewhat larger than 1 to reach full frustration as electron trapping from the core outwards leads to partial screening of ions and thus, not all N_{ion} ions created by photoionization contribute to the droplet charge, with the exact value depending on the conditions of the given system. The degree of frustration has direct impact on the droplet expansion dynamics following ionization, with Coulomb explosion dominating for $\alpha \lesssim 1$ and hydrodynamic expansion of the nanoplasma for $\alpha \gg 1$. At intermediate values with α on the order of ~10, the expansion does not clearly fall into either of these limiting categories. We emphasize that the frustration parameter is a measure of frustration based on photoionization alone. Taking into account the secondary electron impact ionization, the number of produced ions may be larger by up to a factor of ~30, based on the ratio between the photon energy and the He atom IP. However, with increasing charge density and the emergence of lower E_{kin} electrons, there is also an increased likelihood of electron-ion recombination. As such, the total number of ions evolves with time in a complex fashion that is beyond the scope of this work. We therefore resort to define the frustration parameter based on the primary photoionization alone, which are directly accessible within our experiment.

From $N_{ion} \propto FR_0^3$ it follows that $\alpha \propto FR_0^2$, elucidating the relationship between x-ray flux, droplet size, and expansion regime. Note, in particular, that both the x-ray flux and the droplet size contribute independently to the degree of ionization frustration. Thus, both need to be determined on an event-by-event basis in order to evaluate the regime of ionization for every x-ray–droplet interaction. The results presented herein are associated with frustration parameters

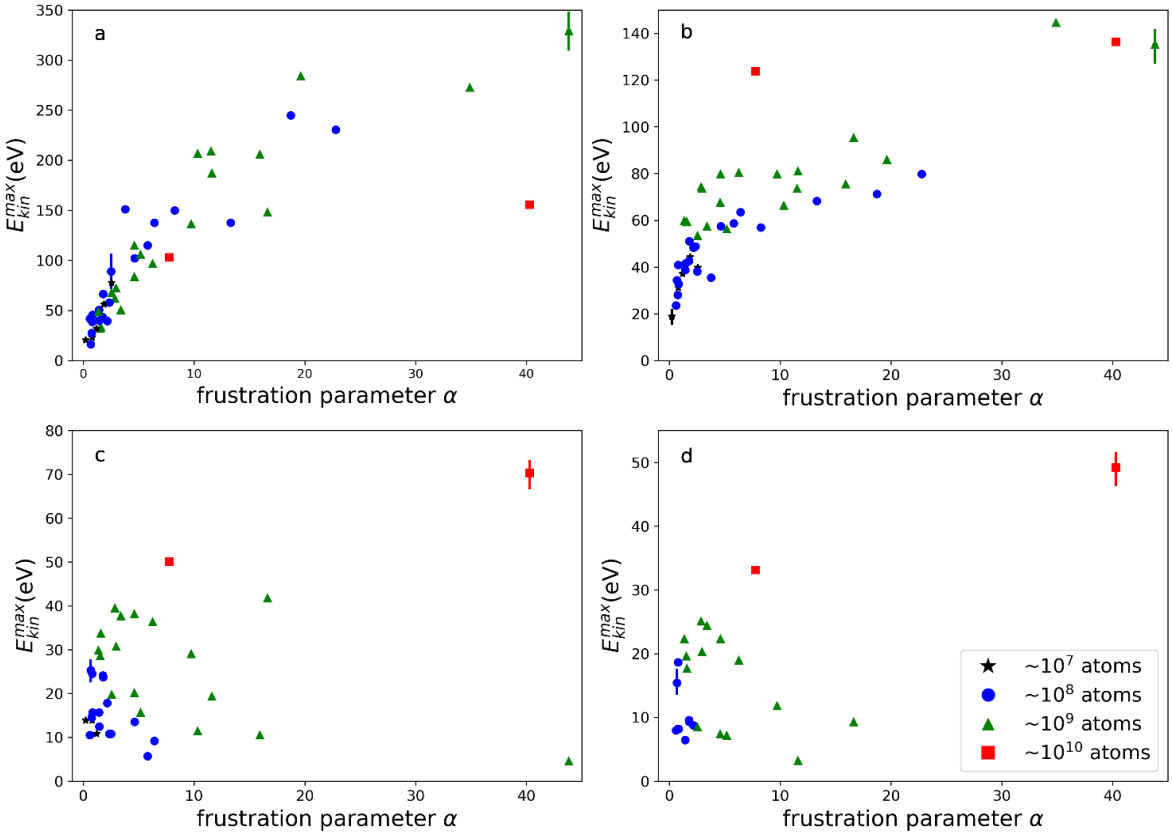

Figure 5.3. Maximum ion kinetic energies, E_{kin}^{max} derived from the shortest flight times in the ion TOF spectra and plotted as a function of the frustration parameter α for a) monomer, b) dimer, c) trimer, and d) tetramer cations.

between $\alpha = 0.23$ and $\alpha = 44$, spanning the entire range from pure Coulomb explosion to significant ionization frustration, expected to lead predominantly to hydrodynamic expansion.

5.4.2. Relation between maximum kinetic energy release and degree of frustration

Different cluster disintegration mechanisms typically give rise to different kinetic energies of the ions [105], [118], [119]. Thus, it is instructive to plot the maximum detected ion kinetic energy E_{kin}^{max} against the frustration parameter α. This relation is shown for He^+, He_2^+, He_3^+ and He_4^+ ions in Figure 5.3 a, b, c, and d, respectively. For monomer and dimer cations, a clear trend emerges, whereby E_{kin}^{max} increases continuously with increasing α for α≲20 and appears to saturate for larger degrees of frustration. For trimers and tetramers, no clear trend emerges. However, the characteristic kinetic energies decrease with increasing size n of the He_j^+ fragments. Representative error bars are included in all panels, which are estimated based on systematic

uncertainty for the high E_{kin}^{max} and electronic signal noise for small E_{kin}^{max}, as described in section 5.3.2

Note that the monomer and dimer cation trends, while qualitatively similar, differ on a quantitative level. The maximum kinetic energies of the monomer cations in the plateau region exceed those of the dimer cations by approximately a factor of two. We speculate that this effect may be the result of a combination of two underlying phenomena. With increasing fluence and therefore a higher degree of frustration, we observe a decrease in cationic cluster compared to monomer fragment yield (see Figure 5.2). One can infer that fragments larger than monomers are less likely to survive the most energetic expansion conditions that produce the fastest He^+ ions. Consequently, the fastest He_j^+ ions may be formed and ejected during different phases of the expansion compared to the He^+ fragments. Other works [109]–[111] suggest contributions from different expansion stages to detected ion mass and kinetic energy distributions, whereby the outer shell of unscreened ions undergo a Coulomb explosion while the remaining plasma core undergoes a hydrodynamic expansion. If the $He_{j\geq2}^+$ products formed in the later stages of the shell explosion and/or in the plasma core, this could lead to lower ion kinetic energies.

In the following discussion, we will use the results for He^+ ions in Figure 5.3a to derive a quantitative model for explaining the observed kinetic energy dependences based on Coulomb repulsion and ion-atom scattering effects. Results for He_j^+ clusters are not included in the discussion. Such clusters are formed upon attachment of one or more He atoms to He^+ ions, with complex dynamics that are beyond the scope of this work.

5.4.3. Simulation of cluster charge for partially frustrated ionization

As described in section 5.4.1, once the Coulomb potential (equation (5.4)) around $r = 0$ becomes sufficiently deep (i.e., the potential energy reaches about 813 eV) at some time $t = t_0$ during the x-ray – pulse, photoelectrons start to get trapped near the droplet center [104]. For $t > t_0$, continued ionization further deepens the potential and extends the range of frustrated ionization to larger radii $r_{frust}(t) > 0$. At any time $t = t_i > t_0$ during the x-ray pulse, electron trapping within the region $r \leq r_{frust}(t_i)$ leads to partial screening of the ionic background, which in turn affects the trapping potential for the remainder of the pulse, i.e, for all $t > t_i$. This mutual dependence and dynamic evolution of the droplet charge state and electron trapping potential requires a time-dependent modeling of the charging/trapping dynamics to estimate the total number of trapped electrons as a result of partial frustration. To this end, an iterative, finite time step algorithm is implemented to track the evolution of the Coulomb potential within the droplet as ionization proceeds. In this model, it is assumed that trapped electrons concentrate in the deepest part of the Coulomb potential near the droplet center and efficiently screen ions generated in this region throughout the x-ray pulse. This description leads to charge distribution corresponding to a homogeneously charged spherical shell surrounding a quasi-neutral core [104]. As such, with the onset of frustration, it becomes more accurate to model the cluster Coulomb potential as that of a charged spherical shell of finite thickness:

$$V(r) = \begin{cases} \frac{\rho_{He^+}}{2\varepsilon_0}(R_0^2 - R_{el}^2), & r \leq R_{el} \\ \frac{\rho_{He^+}}{2\varepsilon_0}\left(R_0^2 - \frac{2 \cdot R_{el}^3}{3r} - \frac{r^2}{3}\right), & R_{el} < r < R_0 \\ -\frac{e}{4\pi\varepsilon_0}\frac{N_{eff}}{r}, & r > R_0 \end{cases} \tag{5.7}$$

Here, e is the elementary charge, ε_0 is the permittivity of free space, r corresponds to the distance from the droplet's center, R_0 and R_{el} are the radius of the droplet and quasineutral core, respectively, ρ_{He+} is the charge density of ions in the charged spherical shell, and N_{eff} is the net cluster charge. Since we assume a homogeneous distribution of ionization events, the ion charge density is taken to be $\rho_{He^+} = e \cdot N_{ion}/(\frac{4}{3}\pi R_0^3)$. With continued frustrated ionization, the quasi-neutral core region expands while the thickness of the charged shell is reduced.

At the start of the simulation, the total charge is set such that the Coulomb potential is sufficiently deep to trap ionized electrons at the center of the droplet. At each step, the total charge of the droplet is increased by $+1e$, ρ_{He+}, R_{el} and N_{eff} are updated, and the Coulomb potential is calculated as described in equation (5.7) in order to calculate the trapping threshold radius, $r_{frust}(t_i)$. The corresponding (fractional) increase in the trapped electrons at each step, ΔN_{trap}, is taken to be the product of the added charge density, ρ_+, and the volume within the trapping threshold radius:

$$\Delta N_{trap}(t_i) = \rho_+ \frac{4}{3}\pi r_{frust}^3(t_i) \tag{5.8}$$

The simulation progresses until the total charge equals N_{ion}, and the total number of trapped electrons is obtained by summing over the trapped electrons of all steps, leading to:
$N_{eff} = N_{ion} - N_{trap} = N_{ion} - \sum_i \Delta N_{trap}(t_i)$.

The results of the simulation are also used to determine at which value of α full frustration is achieved. Note that α corresponds to the ratio of all photogenerated ions, N_{ion}, including both screened and unscreened ions, to the net charge N_{frust} of unscreened ions needed for full frustration. Thus, full frustration does not correspond to α = 1. Instead, N_{ion} must be greater than $N_{frust,}$ so that $N_{eff} = N_{frust}$. Using the simulation, the net charge and surface Coulomb potential is calculated for each hit, based on the size and flux extracted from the corresponding scattering image. Within the dataset herein, α ~ 2.5 is the threshold at which the surface Coulomb potential reaches 813.4 eV, the threshold for electron trapping throughout the droplet.

5.5. Discussion

Figure 5.3a indicates a close relationship between the degree of frustration reached during the x-ray – cluster interaction and the maximum kinetic energy of ejected He^+ ions. The physical origin of the observed trend, however, is not readily apparent and requires additional analysis and modeling. Both Coulomb explosion and hydrodynamic expansion may contribute to ion kinetic energy distributions across the range of α values studied here. E_{kin}^{max}, however, is expected to be defined by Coulomb repulsion effects, as indicated by the following estimates. The average ion kinetic energy in a hydrodynamic expansion is described by [120]

$$\langle E_{kin}^{hyd} \rangle = \frac{3}{2} k_b T_e \frac{N_{ion}}{N}, \tag{5.9}$$

where N_{ion}/N is the average charge state per atom, k_b is the Boltzmann constant, and T_e is the initial electron temperature of the nanoplasma. N_{ion}/N is derived from the scattering images as described above, and the remainder of the right-hand term in Equation (5.9) is estimated by the kinetic energy of the trapped photoelectrons: $\frac{3}{2} k_b T_e \simeq 813.4\, eV$. With N_{ion}/N varying between ~9×10-

^{5} and ~3×10^{-3}, $\langle E_{kin}^{hyd}\rangle$ ranges from ~0.07 – 3 eV. These values are ~2 orders of magnitude smaller than the observed E_{kin}^{max} (Figure 5.3). The inclusion of electron impact ionization would bring $\langle E_{kin}^{hyd}\rangle$ at most to within one order of magnitude of E_{kin}^{max}. Thus, we proceed by comparing E_{kin}^{max} to the Coulomb potential energy experienced by an ion at the surface of the charged droplet.

5.5.1. Surface Coulomb Potential Energy

The potential energy of an ion at the droplet's surface ($r = R_0$) is $U_{Coul}(r = R_0) = \frac{e^2}{4\pi\epsilon_0}\frac{N_{eff}}{R_0}$, taking into account the screening of ions by trapped electrons. The effective number of unscreened charges, N_{eff}, contributing to the Coulomb potential is approximated by the difference between the total number of ions and the number of trapped electrons: $N_{eff} = N_{ion} - N_{trap}$. The underlying assumption is that, on average, each trapped electron screens one cationic charge. N_{eff} is estimated for three distinct frustration regimes: (i) $\alpha < 0.67$, (ii) $0.67 \leq \alpha \lesssim 2.5$, and (iii) $\alpha \gtrsim 2.5$. See section 5.4.3 for a more detailed discussion of the underlying frustration regimes.

(i) For $\alpha < 0.67$, the Coulomb potential according to Equation (5.4) is insufficient for electron trapping throughout the entire droplet. Thus, the number of unscreened charges is equivalent to the total number of ions, i.e., $N_{eff} = N_{ion}$.

(ii) The range $0.67 \leq \alpha \lesssim 2.5$ corresponds to partial frustration, in which electron trapping is achieved within a radius, $0 < r_{frust} < R_0$, as governed by the potential in Equation (5.4). A finite step simulation is implemented, as described in section 5.4.3 to determine the number of trapped electrons, $N_{trap,}$ in this regime. N_{eff} is then estimated as $N_{eff} = N_{ion} - N_{trap}$.

(iii) For $\alpha \gtrsim 2.5$, full frustration is achieved at time t_f, with $r_{frust}(t_f) = R_0$. All additional ionization at times $t > t_f$ is subject to electron trapping and does not contribute to the effective number of charges. Thus, N_{eff} can be estimated by $N_{eff} = N_{frust}$.

Figure 5.4 shows the ratio of the measured E_{kin}^{max} and the surface Coulomb potential energy, U_{Coul}, based on the effective number of unscreened charges N_{eff} as described above. The color codes of the data points indicate the same size regimes as in Figures 5.2 and 5.3. A continuous trend emerges, in which E_{kin}^{max} is always smaller than the Coulomb energy of a He^+ ion at the outermost cluster surface ($r = R_0$), and E_{kin}^{max} / U_{Coul} varies between ~ 0.03 and ~ 0.4 across different frustration regimes. The similarities in Figure 5.3a and Figure 5.4 arises from the fact that the surface potential is constant for $\alpha \gtrsim 2.5$.

We note that these estimates neglect electron-electron collisions, which other studies have observed contribute to outer ionization in dense nanoplasmas, thus leading to a higher net charge [121]. However, as this effect is strongly dependent on the density of trapped electrons, it is not expected to play an important role in the study herein, with electron densities ~3 orders of magnitude smaller than $n_{LHe.}$

PresentingE_{kin}^{max}/U_{Coul} plotted against α with log–log scaling elucidates a linear trend, with a slope 0.47, as shown in Figure 5.5. This indicates that $E_{kin}^{max}/U_{Coul} \propto \sqrt{\alpha}$. As such, we use this scaling to plot a trend line in Figure 5.4 of the main text. Analysis of this relationship is beyond the scope of this work.

5.5.2. E_{kin}^{max} in the highly frustrated regime

As shown by Figure 5.4, as α exceeds ~20, E_{kin}^{max}/U_{Coul} begins to plateau, approaching a ratio of ~0.4. In this highly frustrated regime, due to substantial electron trapping, unscreened ions

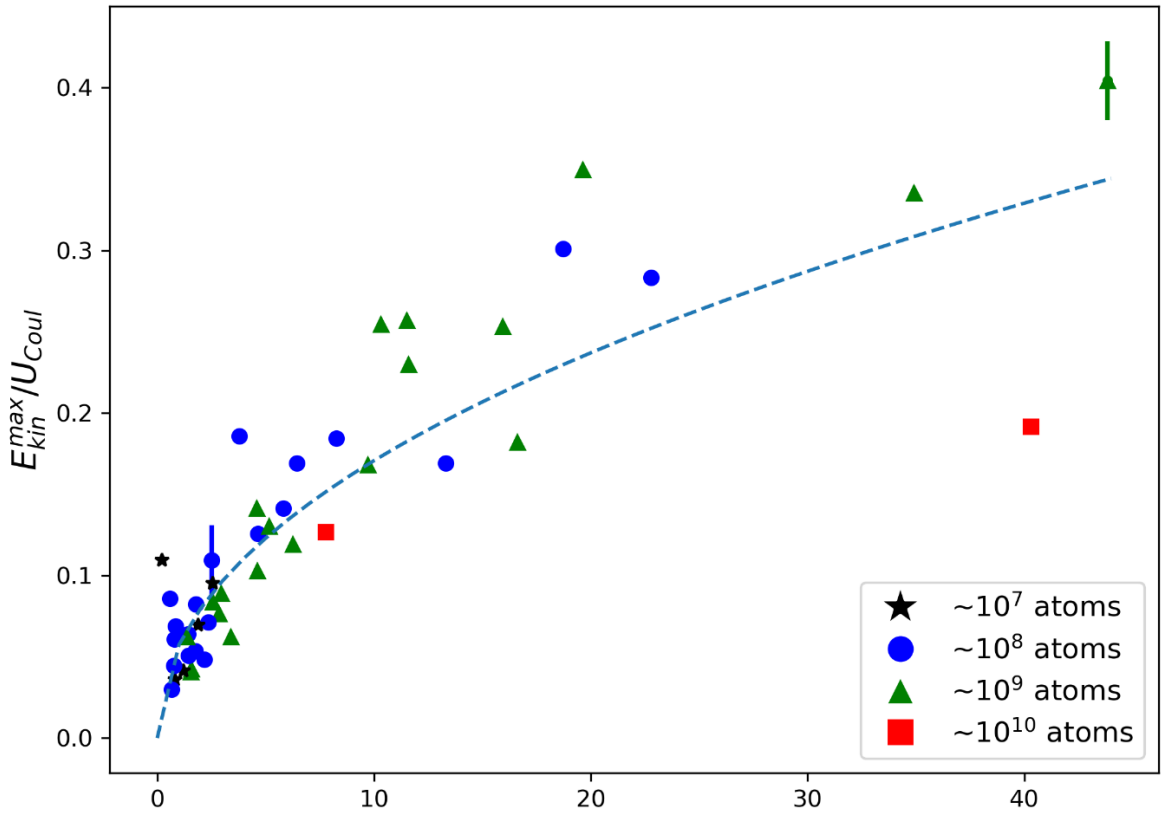

Figure 5.4. Ratio of the maximum He^+ kinetic energy and the Coulomb energy of singly charged ions at the droplet surface.

occupy less than 4 nm (see section 5.5.4) of the outermost shell of the charged droplet, with the remainder of the droplet comprising of a quasineutral core. The range of radii corresponds to less than 2% of the droplet radius. As such, we model the ion ejection in this regime as the expulsion of a thin spherical shell of N_{eff} unscreened ions. Within this model, the average ion kinetic energy KE_{shell} corresponds to the stored energy per ion of a spherical shell:

$$E_{kin}^{shell} = E_{shell}/N_{eff} = \frac{1}{2}\frac{e^2}{4\pi\epsilon_0}\frac{N_{eff}}{R_0} = \frac{1}{2}U_{Coul}\ . \tag{5.10}$$

The ratio of 1/2 between the average E_{kin} per ion and the Coulomb potential is very close to the observed value of ~0.4 in the highly frustrated regime, supporting the picture that a thin spherical shell expansion captures the dominant physics for $\alpha \gtrsim 20$.

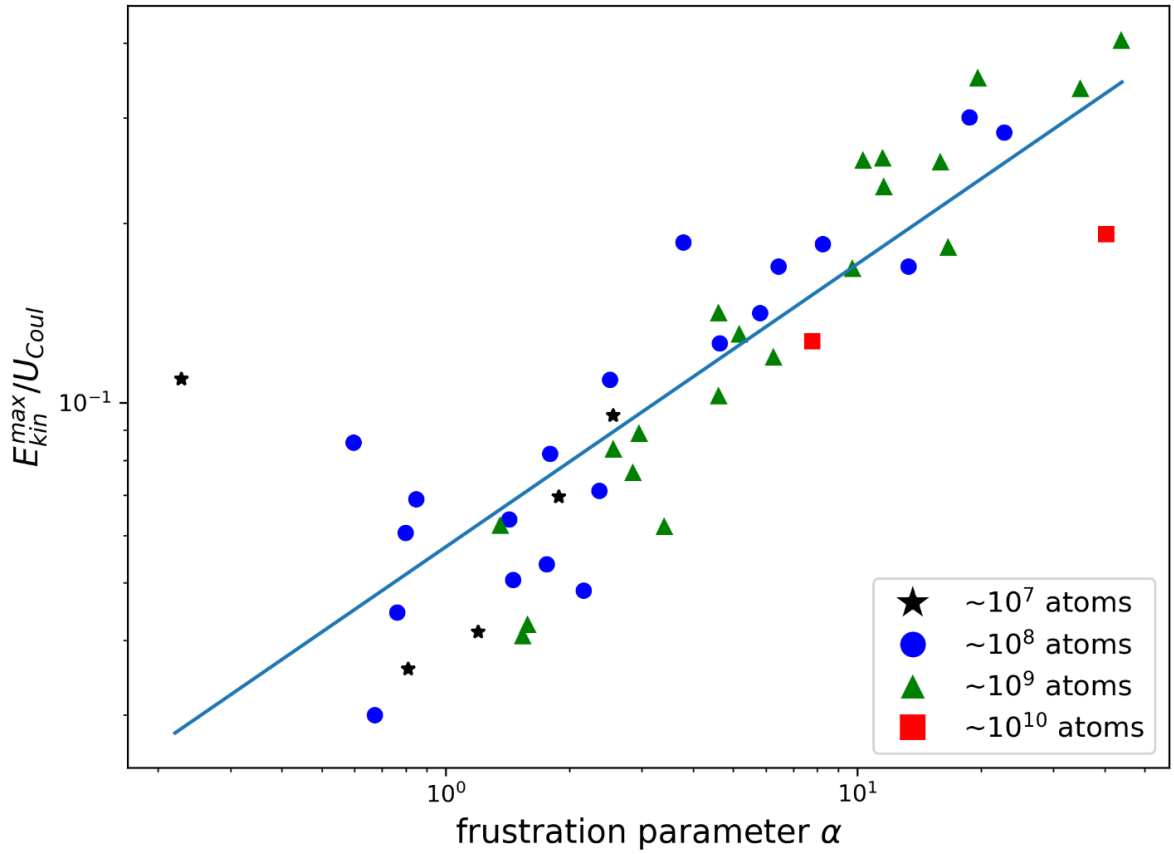

Figure 5.5 Results from figure 5.4 in a log-log representation. The slope of a linear fit indicated by the blue line is 0.47, indicating that E_{kin}^{max} / U_{Coul} scales with $\sqrt{\alpha}$.

5.5.3. E_{kin}^{max} in the weakly frustrated regime

The expected maximum ion E_{kin} for a Coulomb explosion of a homogeneously charged sphere is equivalent to U_{Coul} [122]. However, for $\alpha < 20$, the measured maximum ion kinetic energies are significantly smaller, with E_{kin}^{max}/U_{Coul} reaching values as small as ~1/30 in the non-frustrated regime, where pure Coulomb explosion is expected (Figure 5.4). We propose that this, at first glance, counterintuitive trend is the result of ion-atom interactions throughout the expansion process. Due to the relatively low charge densities herein, ionization of the droplets initiates a Coulomb explosion of unscreened ions within a dense medium of neutral atoms. Ion-atom interactions within the charged droplet impart energy on the neutral atoms and, thus, the expansion will likely be marked by a more collective motion of neutral atoms and ions than in the highly frustrated regime. While a detailed modeling of this motion is beyond the scope of this work, it is instructive to analyze the ratio of the observed E_{kin}^{max} and the surface Coulomb potential U_{Coul} within a picture of a number of (hypothetical) ion-neutral collisions that would be required for ions with initial kinetic energy of U_{Coul} to decelerate to the observed E_{kin}^{max}.

The effect of each collision in this picture on the asymptotic ion kinetic energy depends on the ion's distance from the cluster surface upon colliding with another atom. At short distances,

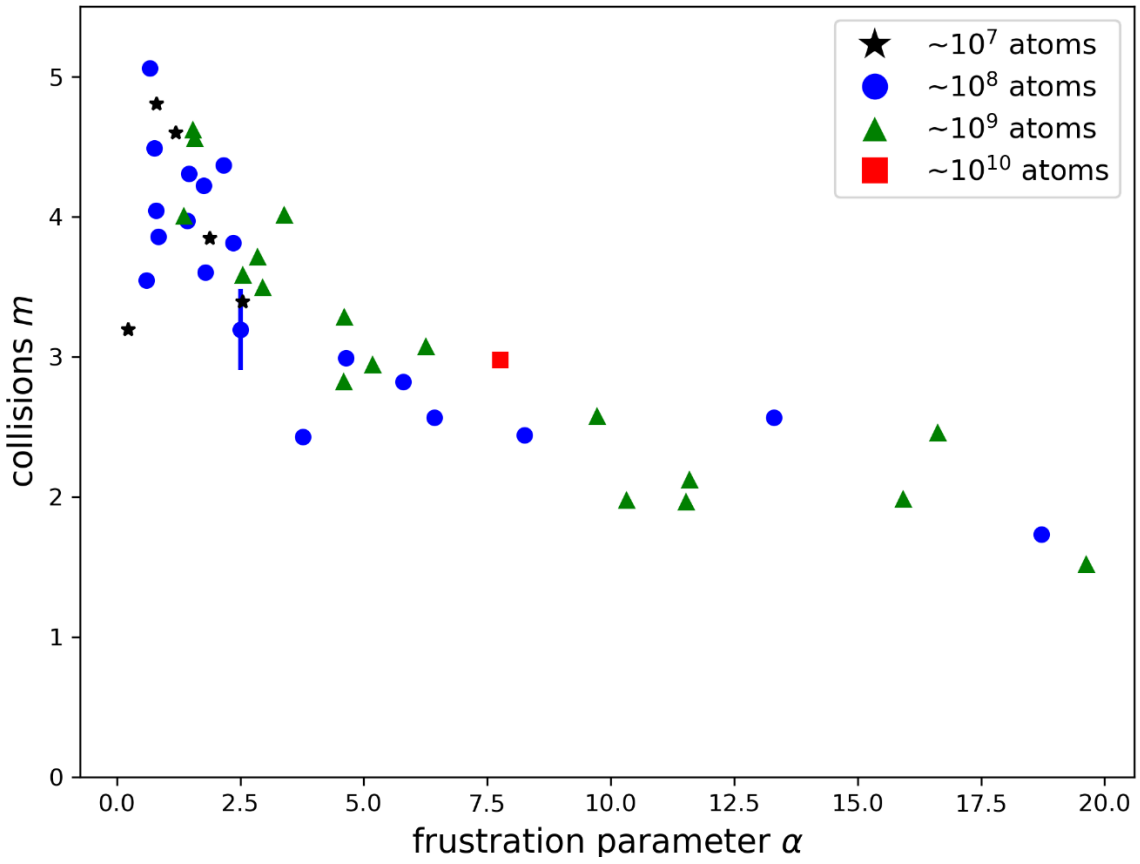

Figure 5.6. Minimum number of ion-atom collisions required to decelerate the ion from the value of the Coulomb energy at the cluster surface to the measured maximum kinetic energy.

the absolute E_{kin} loss will be small, while it is at a maximum in the limit of large distances. We choose to estimate the minimum number of collisions required to account for the observed differences between the cluster surface Coulomb potential and the observed maximum ion kinetic energy. We treat ion-atom collisions within a hard spheres model with equal mass and size of the collision partners, He^+ and He. The average He^+ kinetic energy loss per collision is estimated by assuming elastic collisions of an ion with a He atom at rest. With the probability of a given impact parameter scaling linearly with impact parameter [123], averaging over all collision geometries yields a mean kinetic energy loss per collision of 50%.

Upon undergoing m collisions, the ion kinetic energy, $E_{kin}^{m,th}$, is:

$$E_{kin}^{m,th} = U_{Coul} \cdot 0.5^m \,. \tag{5.11}$$

By equating $E_{kin}^{m,th}$ with the measured values E_{kin}^{max}, the minimum number of collisions can be estimated, as is plotted in Figure 5.6. We observe a decrease in the minimum number of collisions, with a continuous trend that ranges from $m \gtrsim 5$ at small α to $m \gtrsim 1.5$ as we approach α~20. This decrease in number collisions correlates with the increasing plasma core, as the frustration

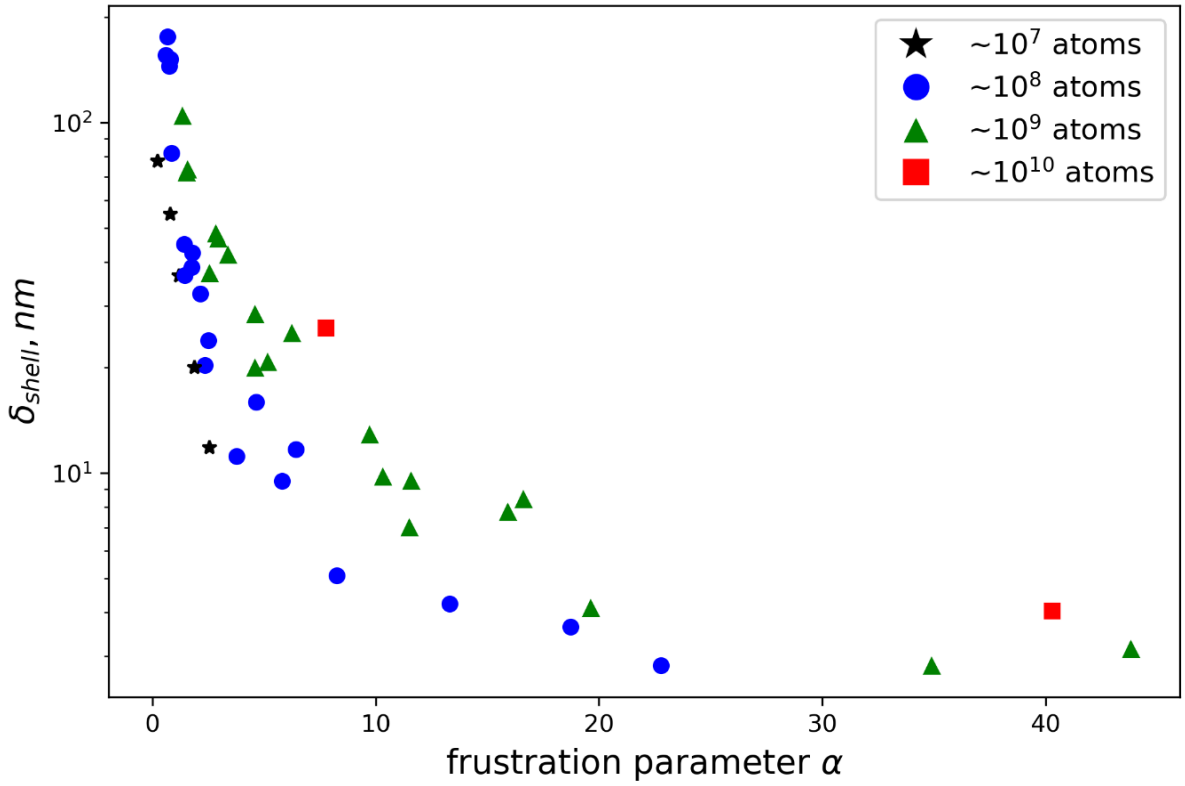

Figure 5.7 Thickness of the shell of unscreened ions as a function of the frustration parameter.

parameter increases. Note that m is representative of the net likelihood for unscreened ions to interact with neutral atoms and does not refer to the individual probability of an ion–atom collision. Furthermore, we note that the underlying physics governing ionic motion is not encompassed in this heuristic model, as this is presently unknown and beyond the scope of this work.

5.5.4 Illustration of Droplet Charge Distributions

In order to visualize the relationship between frustration and shell thickness within the model of a homogeneously charged spherical shell, we derive a mathematical relationship between δ_{shell}, R_0, N_{eff}, and N_{ion}. The thickness of the shell of unscreened ions, δ_{shell}, is calculated from the number of unscreened ions, N_{eff}, from section 5.5.1, and the overall cation charge density $\rho_{He^+} = N_{ion}/\frac{4}{3}\pi R_0^3$ assuming a sharp boundary between the screened and unscreened ions. The shell thickness, δ_{shell}, is related to N_{eff} and ρ_{He+} by:

$$N_{eff} = \frac{4}{3}\pi[R_0^3 - (R_0 - \delta_{shell})^3]\rho_{He^+} \tag{5.12}$$

From this, we derive the following relationship:

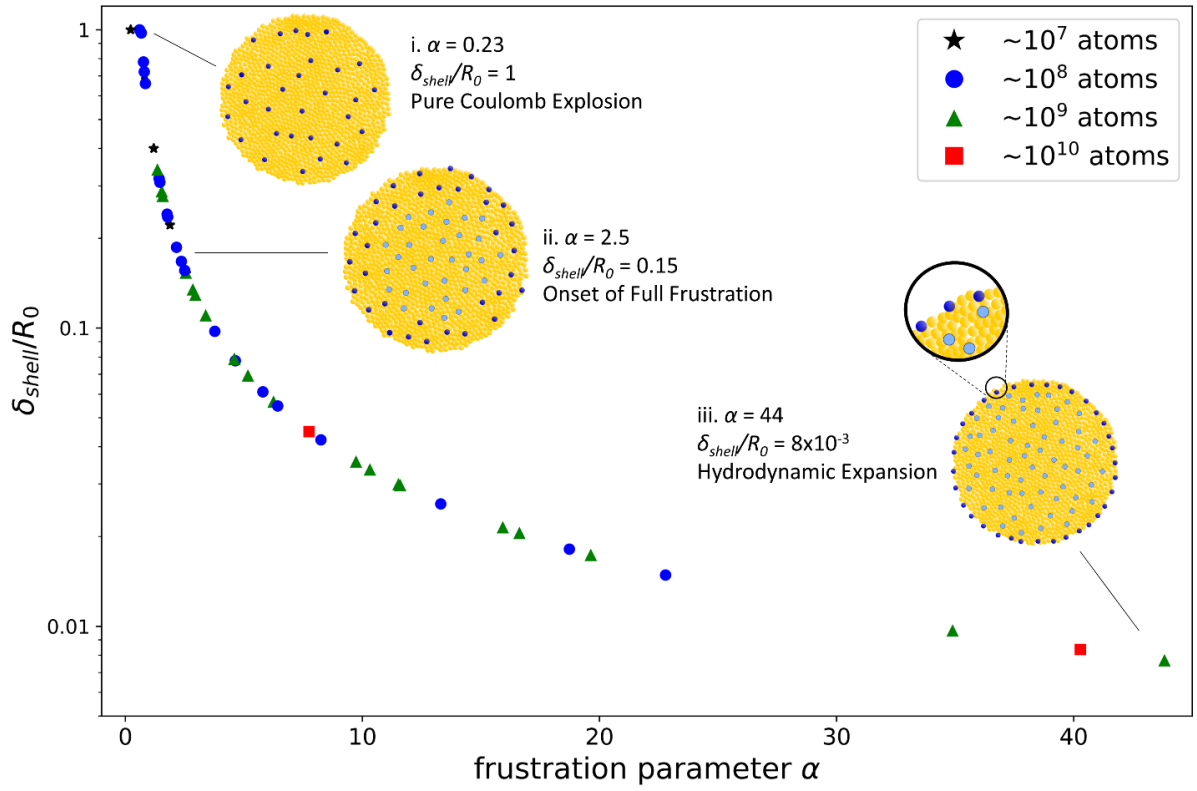

Figure 5.8. Thickness of the shell of unscreened ions normalized to the droplet radius versus the frustration parameter. Pictograms indicate the structure of the charged droplets, which are modeled by charged shells of unscreened ions (dark blue) surrounding a quasineutral plasma core (light blue), interspersed amongst neutral helium atoms (yellow). The three illustrations correspond to different ionization/expansion regimes: (i) no frustration, (ii) onset of full frustration, and (iii) highest observed degree of frustration.

$$\delta_{shell}/R_0 = 1 - \left(1 - \frac{N_{eff}}{N_{ion}}\right)^{\frac{1}{3}}. \tag{5.13}$$

Note that N_{eff}=N_{frust} for α≳2.5, and thus $N_{eff}/N_{ion} = 1/\alpha$.
Furthermore, the shell thickness δ_{shell} can be derived from Equation 5.12 and can be expressed as

$$\delta_{shell} = R_0\left[1 - \left(1 - \frac{N_{eff}}{N_{ion}}\right)^{\frac{1}{3}}\right] \tag{5.14}$$

where R_0 is the droplet radius, N_{ion} is the number of ions from photoionization, and N_{eff} is the net cluster charge as derived in 5.5.1. In Figure 5.7, the shell thickness occupied by unscreened ions is plotted as a function of the frustration parameter α.

Figure 5.8 shows the ratio of the thickness of the shell of unscreened ions and the droplet radius R_0 as a function of the degree of frustration in semilogarithmic scale. The relationship according to Equation 5.13 projects all data points onto a smooth curve, with their distribution along the curve given by the measured α values. The insets provide visualizations of three specific cases corresponding to (i) the limit of no frustration/pure Coulomb explosion, (ii) the onset of full frustration, and (iii) the highest degree of frustration detected in the experiment. In the insets, screened and unscreened ions are depicted as light and dark blue spheres, respectively, and neutral helium atoms are depicted as yellow.

For the smallest values of α, no electron trapping occurs, and unscreened ions are distributed homogeneously throughout the cluster ($\delta_{shell} = R_0$). However, once frustration sets in, the normalized shell thickness, δ_{shell}/R_0, decreases rapidly from 1 to 0.15 over the range $0.67 < \alpha \lesssim 2.5$, corresponding to the transition from no to full frustration. The normalized shell thickness continues to decrease with increasing frustration, reaching a mere 0.8% of the droplet radius at $\alpha = 44$. We note that for $\alpha > 20$, the absolute shell thickness saturates at ~ 3 nm (see figure 5.7). This region corresponds to the plateau observed in the α−dependence of the E_{kin}^{max} in Fig. 3a. Taking into account that the Coulomb potential at the cluster surface already saturates for much smaller values of $\alpha \approx 2.5$, the "delayed" saturation of E_{kin}^{max} in Fig. 3a and the correspondence of the plateau regions for the E_{kin}^{max} and the absolute thickness of the unscreened ion shell lends further support to the concept that both Coulomb repulsion and ion-atom collisions play important roles for determining the maximum ion E_{kin}.

The clusters studied here in a single experiment, under nominally identical experimental conditions, cover the entire range of charging conditions, from a homogeneous distribution of ions subject to mutual Coulomb repulsion to quasineutral nanoplasmas extending across > 99% of the droplet diameter. Differentiating these charged cluster varieties has only become possible through the single-pulse measurement capabilities developed at X-FELs. At the same time, they illustrate the importance of complete characterizations of light– matter interactions on a pulse-by-pulse basis in order to understand the underlying physics.

5.6. Conclusions

Charging and disintegration of helium nanodroplets exposed to intense soft x-ray pulses is studied by single pulse coincident ion TOF spectroscopy and small-angle x-ray scattering. Experimental conditions span from pure Coulomb explosion to a regime of deeply frustrated ionization. The low ion density due to the small x-ray absorption cross section of He leads to a complex relationship between measured ion kinetic energies and cluster ionization conditions that can only be disentangled through the coincident single-pulse measurement capability. Maximum ion kinetic energies are modeled by a combination of Coulomb repulsion from unscreened cluster ions and ion-atom interactions during the expansion. We find that the measured kinetic energies reflect on ions created deeper inside the droplet in the Coulomb explosion limit and on ions originating from the surface in the deeply frustrated, hydrodynamic limit. The results demonstrate the need for quantitative single pulse information to derive physical insight from interpreting ion TOF spectra in intense x-ray—cluster interactions.

Acknowledgments

This work was supported by the Atomic, Molecular, and Optical Sciences Program of the US Department of Energy, Office of Science, Office of Basic Energy Sciences, Chemical Sciences, Geosciences and Biosciences Division, through Contract No. DE-AC02-05CH11231 (C.A.S., M.P.Z., C.Ba., A.S.C., D.M.N., O.G.) and Contract No DE-AC02-06CH11357 (MB, C.Bo.). A.J.F., C.Be., L.G., C.F.J., J.J.K., R.M.P.T, and A.F.V. were supported by the National Science Foundation under Grants No. CHE-1664990 and DMR-1701077. T.M. was supported by DFG grant Mo 718/14-2. C.Bo. acknowledges the Swiss National Science Foundation via the National Center of Competence in Research – Molecular Ultrafast Science and Technology NCCR - MUST.Portions of this research were carried out at the LCLS, a national user facility operated by Stanford University on behalf of the U.S. DOE, OBES under beam-time Grant No. LA12: Time-Resolved Imaging of X-ray Induced Dynamics in Clusters. Use of the Linac Coherent Light Source (LCLS), SLAC National Accelerator Laboratory, is supported by the U.S. Department of Energy, Office of Science, Office of Basic Energy Sciences under Contract No. DE-AC02-76SF00515.

Bibliography

[1] R. L. Johnston, *Atomic and Molecular Clusters*. Taylor & Francis, 2002.

[2] J. S. Brooks and R. J. Donnelly, "The calculated thermodynamic properties of superfluid helium-4," *Journal of Physical and Chemical Reference Data*, vol. 6, no. 1, pp. 51–104, 1977, doi: 10.1063/1.555549.

[3] T. Lindenau, M. L. Ristig, J. W. Clark, and K. A. Gernoth, "Bose-Einstein Condensation and the l Transition in Liquid Helium," 2002.

[4] J. P. Toennies, "Helium Nanodroplets: Formation, Physical Properties and Superfluidity," in *Molecules in Superfluid Helium Nanodroplets*, J. P. Toennies and A. Slenczka, Eds. Springer, 2022, pp. 1–40.

[5] M. Hartmann, R. E. Miller, J. P. Toennies, and A. Vilesov, "Rotationally Resolved Spectroscopy of SF6 in Liquid Helium Clusters: A Molecular Probe of Cluster Temperature," 1995.

[6] O. Gessner and A. F. Vilesov, "Imaging Quantum Vortices in Superfluid Helium Droplets," *Annual Review of Physical Chemistry Annu. Rev. Phys. Chem*, vol. 70, pp. 173–198, 2019, doi: 10.1146/annurev-physchem-042018.

[7] L. F. Gomez *et al.*, "Shapes and vorticities of superfluid helium nanodroplets," *Science (1979)*, vol. 345, no. 6199, pp. 906–909, 2014, doi: 10.1126/science.1252395.

[8] P. Kapitza, "Viscosity of Liquid Helium below the λ-Point," *Nature*, vol. 141, p. 74, 1938.

[9] W. H. Keesom and M. A. P. Keesom, "On the Heat Conductivity of Liquid Helium," *Physica*, vol. III, no. 5, pp. 359–360, 1936.

[10] J. P. Toennies and A. F. Vilesov, "Superfluid helium droplets: A uniquely cold nanomatrix for molecules and molecular complexes," *Angewandte Chemie - International Edition*, vol. 43, no. 20. pp. 2622–2648, May 10, 2004. doi: 10.1002/anie.200300611.

[11] A. J. Feinberg *et al.*, "Aggregation of solutes in bosonic versus fermionic quantum fluids," *Sci. Adv*, vol. 7, p. 2247, 2021, [Online]. Available: https://www.science.org

[12] M. Joppien, R. Karnbach, and T. Möller, "Electronic Excitations in Liquid Helium: The Evolution from Small Clusters to Large Droplets," *Physical Review Letters*, vol. 71, no. 16, pp. 2654–2657, 1993.

[13] W. F. Chan, G. Cooper, and C. E. Brion, "Absolute optical oscillator strengths for the electronic excitation of atoms at high resolution: Experimental methods and measurements for helium," *Physical Review A*, vol. 44, no. 1, pp. 186–204, Jul. 1991.

[14] D. S. Peterka, A. Lindinger, L. Poisson, M. Ahmed, and D. M. Neumark, “Photoelectron Imaging of Helium Droplets,” *Physical Review Letters*, vol. 91, no. 4, Jul. 2003, doi: 10.1103/PhysRevLett.91.043401.

[15] J. W. Cooper, “Total photon attenuation cross sections of helium at energies below 10 keV. An assessment of the accuracy of measured and calculated cross sections,” *Radiation Physics and Chemistry*, vol. 47, no. 6, pp. 927–934, 1996, doi: 10.1016/0969-806X(95)00339-Y.

[16] R. M. P. Tanyag, C. F. Jones, C. Bernando, S. M. O. O’Connell, D. Verma, and A. F. Vilesov, “Experiments with Large Superfluid Helium Nanodroplets,” in *Cold Chemistry: Molecular Scattering and Reactivity Near Absolute Zero*, A. Osterwalder and O. Dulieu, Eds. Cambridge: Royal Society of Chemistry, 2017, pp. 389–443.

[17] M. P. Ziemkiewicz, D. M. Neumark, and O. Gessner, “Ultrafast electronic dynamics in helium nanodroplets,” *International Reviews in Physical Chemistry*, vol. 34, no. 2, pp. 239–267, Apr. 2015, doi: 10.1080/0144235X.2015.1051353.

[18] D. Verma, S. Erukala, and A. F. Vilesov, “Infrared Spectroscopy of Water and Zundel Cations in Helium Nanodroplets,” *Journal of Physical Chemistry A*, vol. 124, no. 30, pp. 6207–6213, Jul. 2020, doi: 10.1021/acs.jpca.0c05897.

[19] A. S. Chatterley, B. Shepperson, and H. Stapelfeldt, “Three-Dimensional Molecular Alignment Inside Helium Nanodroplets,” *Physical Review Letters*, vol. 119, no. 7, Aug. 2017, doi: 10.1103/PhysRevLett.119.073202.

[20] D. Attwood and A. Sakdinawat, *X-rays and Extreme Ultraviolet Radiation: Principles and Applications*, 2nd ed. Cambridge, UK: Cambridge University Press, 2016.

[21] R. M. P. Tanyag *et al.*, “Communication: X-ray coherent diffractive imaging by immersion in nanodroplets,” *Structural Dynamics*, vol. 2, no. 051102, p. 051102, Sep. 2015, doi: 10.1063/1.4933297.

[22] R. M. P. Tanyag, B. Langbehn, T. Möller, and D. Rupp, “X-Ray and XUV Imaging of Helium Nanodroplets,” in *Molecules in Superfluid Helium Nanodroplets*, A. Slenczka and J. P. Toennis, Eds. 2022, pp. 281–342.

[23] D. Rupp *et al.*, “Coherent diffractive imaging of single helium nanodroplets with a high harmonic generation source,” *Nature Communications*, vol. 8, no. 1, Dec. 2017, doi: 10.1038/s41467-017-00287-z.

[24] A. J. Feinberg *et al.*, “X-ray diffractive imaging of highly ionized helium nanodroplets,” *Physical Review Research*, vol. 4, no. 2, Jun. 2022, doi: 10.1103/physrevresearch.4.l022063.

[25] S. M. O. O’Connell *et al.*, “Angular Momentum in Rotating Superfluid Droplets,” *Physical Review Letters*, vol. 124, no. 21, p. 215301, 2020, doi: 10.1103/PhysRevLett.124.215301.

[26] D. Verma *et al.*, “Shapes of rotating normal fluid He 3 versus superfluid He 4 droplets in molecular beams,” *Physical Review B*, vol. 102, no. 1, pp. 22–30, 2020, doi: 10.1103/PhysRevB.102.014504.

[27] L. Bruder, M. Koch, M. Mudrich, and F. Stienkemeier, “Ultrafast Dynamics in Helium Droplets,” in *Molecules in Superfluid Helium Nanodroplets*, A. Slenckz and J. P. Toennies, Eds. Springer, 2022, pp. 447–511.

[28] C. Bacellar *et al.*, “Anisotropic surface broadening and core depletion during the evolution of a strong-field induced nanoplasma,” *Physical Review Letters*, vol. accepted.

[29] O. Kornilov *et al.*, “Ultrafast dynamics in helium nanodroplets probed by femtosecond time-resolved EUV photoelectron imaging,” *Journal of Physical Chemistry A*, vol. 114, no. 3, pp. 1437–1445, 2010, doi: 10.1021/jp907312t.

[30] O. Bünermann, O. Kornilov, S. R. Leone, D. M. Neumark, and O. Gessner, “Femtosecond extreme ultraviolet ion imaging of ultrafast dynamics in electronically excited helium nanodroplets,” *IEEE Journal on Selected Topics in Quantum Electronics*, vol. 18, no. 1, pp. 308–317, 2012, doi: 10.1109/JSTQE.2011.2109054.

[31] O. Kornilov, O. Bünermann, D. J. Haxton, S. R. Leone, D. M. Neumark, and O. Gessner, “Femtosecond photoelectron imaging of transient electronic states and rydberg atom emission from electronically excited he droplets,” *Journal of Physical Chemistry A*, vol. 115, no. 27, pp. 7891–7900, Jul. 2011, doi: 10.1021/jp2004216.

[32] O. Bünermann, O. Kornilov, D. J. Haxton, S. R. Leone, D. M. Neumark, and O. Gessner, “Ultrafast probing of ejection dynamics of Rydberg atoms and molecular fragments from electronically excited helium nanodroplets,” *Journal of Chemical Physics*, vol. 137, no. 21, Dec. 2012, doi: 10.1063/1.4768422.

[33] M. P. Ziemkiewicz, C. Bacellar, K. R. Siefermann, S. R. Leone, D. M. Neumark, and O. Gessner, “Femtosecond time-resolved XUV + UV photoelectron imaging of pure helium nanodroplets,” *Journal of Chemical Physics*, vol. 141, no. 17, Nov. 2014, doi: 10.1063/1.4900503.

[34] M. L. Ginter and R. Battino, “ Potential-Energy Curves for the He 2 Molecule ,” *The Journal of Chemical Physics*, vol. 52, no. 9, pp. 4469–4474, May 1970, doi: 10.1063/1.1673675.

[35] Y. Ovcharenko *et al.*, “Novel collective autoionization process observed in electron spectra of He clusters,” *Physical Review Letters*, vol. 112, no. 7, Feb. 2014, doi: 10.1103/PhysRevLett.112.073401.

[36] C. Bostedt *et al.*, “Multistep ionization of argon clusters in intense femtosecond extreme ultraviolet pulses,” *Physical Review Letters*, vol. 100, no. 133401, p. 133401, 2008, doi: 10.1103/PhysRevLett.100.133401.

[37] M. Arbeiter and T. Fennel, “Rare-gas clusters in intense VUV, XUV and soft x-ray pulses: Signatures of the transition from nanoplasma-driven cluster expansion to Coulomb explosion in ion and electron spectra,” *New Journal of Physics*, vol. 13, no. 053022, p. 053022, 2011, doi: 10.1088/1367-2630/13/5/053022.

[38] I. Last and J. Jortner, “Dynamics of the Coulomb explosion of large clusters in a strong laser field,” *Physical Review A - Atomic, Molecular, and Optical Physics*, vol. 62, p. 013201, 2000, doi: 10.1103/PhysRevA.62.013201.

[39] H. Buchenau, E. L. Knuth, J. Northby, J. P. Toennies, and C. Winkler, “Mass spectra and time-of-flight distributions of helium cluster beams,” *The Journal of Chemical Physics*, vol. 92, no. 11, pp. 6875–6889, 1990, doi: 10.1063/1.458275.

[40] A. Wall, K F Sanchez, “TItanium Sapphire Lasers,” vol. 3, no. 3, pp. 447–462, 1990.

[41] D. Strickland, “Nobel Lecture: Generating high-intensity ultrashort optical pulses,” *Reviews of Modern Physics*, vol. 91, no. 3, p. 30502, 2019, doi: 10.1103/RevModPhys.91.030502.

[42] D. Strickland and G. Mourou, “Compression of amplified chirped optical pulses,” *Optical Communications*, vol. 55, no. 6, pp. 447–449, 1985.

[43] D. Strickland, “Chirped Pulse Amplifcation,” in *Handbook of Laser Technology and Applications*, 2nd ed., vol. 1, C. Guo and S. C. Singh, Eds. CRC Press, 2021, pp. 321–330.

[44] W. H. Lowdermilk and J. E. Murray, “The multipass amplifier: Theory and numerical analysis,” *Journal of Applied Physics*, vol. 51, no. 5, pp. 2436–2444, 1980, doi: 10.1063/1.328014.

[45] J. v Rudd, G. Korn, S. Kane, J. Squier, G. Mourou, and P. Bado, “Chirped-pulse amplification of 55-fs pulses at a 1-kHz repetition rate in a Ti:A1 2 0 3 regenerative amplifier,” 1993.

[46] K. Wynne, G. D. Reid, and R. M. Hochstrasser, “Regenerative amplification of 30-fs pulses in Ti:sapphire at 5 kHz,” 1994.

[47] J.-C. Diels and W. Rudolph, *Ultrashort Laser Pulse Phenomena*, Second. Academic Press, 2006.

[48] J. D. Pickering, *Ultrafast Lasers and Optics for Experimentalists*. Bristol: IOP Publishing, 2021.

[49] Robert W. Boyd, *Nonlinear Optics*, Third. Academic Press, 2008.

[50] T. Pfeifer, C. Spielmann, and G. Gerber, “Femtosecond x-ray science,” *Reports on Progress in Physics*, vol. 69, no. 2, pp. 443–505, 2006, doi: 10.1088/0034-4885/69/2/R04.

[51] C. M. Heyl, C. L. Arnold, A. Couairon, and A. L’Huillier, “Introduction to macroscopic power scaling principles for high-order harmonic generation,” *Journal of Physics B:*

Atomic, Molecular and Optical Physics, vol. 50, no. 1, Jan. 2017, doi: 10.1088/1361-6455/50/1/013001.

[52] P. B. Corkum, "Plasma Perspective on Strong-Field Multiphoton Ionization," 1993.

[53] K. J. Schafer, B. Yang, L. F. DiMauro, and K. C. Kulander, "Above Threshold Ionization Beyond the High Harmonic Cutoff'," *Physical Review Letters*, vol. 70, no. 11, pp. 1599–1602, 1993.

[54] C. Marceau, T. J. Hammond, A. Y. Naumov, P. B. Corkum, and D. M. Villeneuve, "Wavelength scaling of high harmonic generation for 267 nm, 400nm and 800nm driving laser pulses," *Journal of Physics Communications*, vol. 1, no. 1, Aug. 2017, doi: 10.1088/2399-6528/aa74f6.

[55] M. C. Kohler, T. Pfeifer, K. Z. Hatsagortsyan, and C. H. Keitel, "Frontiers of Atomic High-Harmonic Generation," in *Advances in Atomic, Molecular and Optical Physics*, vol. 61, Academic Press Inc., 2012, pp. 159–208. doi: 10.1016/B978-0-12-396482-3.00004-1.

[56] K. F. Chang *et al.*, "Conical intersection and coherent vibrational dynamics in alkyl iodides captured by attosecond transient absorption spectroscopy," *Journal of Chemical Physics*, vol. 156, no. 11, Mar. 2022, doi: 10.1063/5.0086775.

[57] K. F. Chang, H. Wang, S. M. Poullain, D. Prendergast, D. M. Neumark, and S. R. Leone, "Mapping wave packet bifurcation at a conical intersection in CH3I by attosecond XUV transient absorption spectroscopy," *Journal of Chemical Physics*, vol. 154, no. 23, p. 1ENG, Jun. 2021, doi: 10.1063/5.0056299.

[58] R. Neutze, R. Wouts, D. van der Spoel, E. Weckert, and J. Hajdu, "Potential for biomolecular imaging with femtosecond X-ray pulses," *Nature*, vol. 406, pp. 752–757, 2000.

[59] Z. Huang and K. J. Kim, "Review of x-ray free-electron laser theory," *Physical Review Special Topics - Accelerators and Beams*, vol. 10, no. 3. Mar. 12, 2007. doi: 10.1103/PhysRevSTAB.10.034801.

[60] O. Y. Gorobtsov *et al.*, "Seeded X-ray free-electron laser generating radiation with laser statistical properties," *Nature Communications*, vol. 9, no. 1, Dec. 2018, doi: 10.1038/s41467-018-06743-8.

[61] I. A. Vartanyants *et al.*, "Coherence properties of individual femtosecond pulses of an x-ray free-electron laser," *Physical Review Letters*, vol. 107, no. 14, Sep. 2011, doi: 10.1103/PhysRevLett.107.144801.

[62] E. A. Seddon *et al.*, "Short-wavelength free-electron laser sources and science: A review," *Reports on Progress in Physics*, vol. 80, no. 11. Institute of Physics Publishing, Oct. 23, 2017. doi: 10.1088/1361-6633/aa7cca.

[63] M. Hoener *et al.*, "Ultraintense x-ray induced ionization, dissociation, and frustrated absorption in molecular nitrogen," *Physical Review Letters*, vol. 104, no. 25, Jun. 2010, doi: 10.1103/PhysRevLett.104.253002.

[64] T. Gorkhover *et al.*, "Nanoplasma dynamics of single large xenon clusters irradiated with superintense X-ray pulses from the linac coherent light source free-electron laser," *Physical Review Letters*, vol. 108, no. 245005, p. 245005, 2012, doi: 10.1103/PhysRevLett.108.245005.

[65] J. Berkowitz, *Photoabsorption, Photoionization, and Photoelectron Spectroscopy*. Academic Press, 1979.

[66] W. C. Wiley and I. H. McLaren, "Time-of-flight mass spectrometer with improved resolution," *Review of Scientific Instruments*, vol. 26, no. 12, pp. 1150–1157, 1955, doi: 10.1063/1.1715212.

[67] A. T. J. B. Eppink and D. H. Parker, "Velocity map imaging of ions and electrons using electrostatic lenses: Application in photoelectron and photofragment ion imaging of molecular oxygen," *Review of Scientific Instruments*, vol. 68, no. 9, pp. 3477–3484, 1997, doi: 10.1063/1.1148310.

[68] M. M. Harb, S. Cohen, E. Papalazarou, F. Lépine, and C. Bordas, "Transfer-matrix-based method for an analytical description of velocity-map-imaging spectrometers," *Review of Scientific Instruments*, vol. 81, no. 12, Dec. 2010, doi: 10.1063/1.3505799.

[69] M. Kerker, *The Scattering of Light and Other Electromagnetic Radiation* . New York: Academic Press, 1969.

[70] Darcy S. Peterka, "Imaging Chemical Dynamics with the Vacuum Ultraviolet," University of California, Berkeley, Berkeley, 2005.

[71] S. A. Chin and E. Krotscheck, "Systematics of pure and doped 4He clusters," *PHYSICAL REVIEW B*, vol. 52, no. 14, pp. 10405–10428, 1995.

[72] L. F. Gomez, E. Loginov, R. Sliter, and A. F. Vilesov, "Sizes of large He droplets," *Journal of Chemical Physics*, vol. 135, no. 154201, p. 154201, 2011, doi: 10.1063/1.3650235.

[73] C. B. C. Silveira, "Ultrafast dynamics in helium nanodroplets probed by XUV spectroscopy and x-ray imaging," University of California, Berkeley, Berkeley, 2017.

[74] O. Kornilov, R. Wilcox, and O. Gessner, "Nanograting-based compact vacuum ultraviolet spectrometer and beam profiler for in situ characterization of high-order harmonic generation light sources," *Review of Scientific Instruments*, vol. 81, no. 6, Jun. 2010, doi: 10.1063/1.3443575.

[75] J. P. Brichta, M. C. H. Wong, J. B. Bertrand, H. C. Bandulet, D. M. Rayner, and V. R. Bhardwaj, "Comparison and real-time monitoring of high-order harmonic generation in

different sources," *Physical Review A - Atomic, Molecular, and Optical Physics*, vol. 79, no. 3, Mar. 2009, doi: 10.1103/PhysRevA.79.033404.

[76] E. Hecht, *Optics*, 4th ed. Pearson, 2002.

[77] B. Dick, "Inverting ion images without Abel inversion: Maximum entropy reconstruction of velocity maps," *Physical Chemistry Chemical Physics*, vol. 16, no. 2, pp. 570–580, 2014, doi: 10.1039/c3cp53673d.

[78] G. A. Garcia, L. Nahon, and I. Powis, "Two-dimensional charged particle image inversion using a polar basis function expansion," *Review of Scientific Instruments*, vol. 75, no. 11, pp. 4989–4996, Nov. 2004, doi: 10.1063/1.1807578.

[79] V. Dribinski, A. Ossadtchi, V. A. Mandelshtam, and H. Reisler, "Reconstruction of Abel-transformable images: The Gaussian basis-set expansion Abel transform method," *Review of Scientific Instruments*, vol. 73, no. 7, p. 2634, Jul. 2002, doi: 10.1063/1.1482156.

[80] K. R. Ferguson *et al.*, "The Atomic, Molecular and Optical Science instrument at the Linac Coherent Light Source," *Journal of Synchrotron Radiation*, vol. 22, pp. 492–497, 2015, doi: 10.1107/S1600577515004646.

[81] T. Osipov *et al.*, "The LAMP instrument at the Linac Coherent Light Source free-electron laser," *Review of Scientific Instruments*, vol. 89, no. 035112, p. 035112, 2018, doi: 10.1063/1.5017727.

[82] R. Michiels *et al.*, "Enhancement of above Threshold Ionization in Resonantly Excited Helium Nanodroplets," *Physical Review Letters*, vol. 127, no. 9, Aug. 2021, doi: 10.1103/PhysRevLett.127.093201.

[83] M. Mudrich *et al.*, "Ultrafast relaxation of photoexcited superfluid He nanodroplets," *Nature Communications*, vol. 11, no. 1, Dec. 2020, doi: 10.1038/s41467-019-13681-6.

[84] X. Ren, E. Wang, A. D. Skitnevskaya, A. B. Trofimov, K. Gokhberg, and A. Dorn, "Experimental evidence for ultrafast intermolecular relaxation processes in hydrated biomolecules," *Nature Physics*, vol. 14, no. 10, pp. 1062–1066, Oct. 2018, doi: 10.1038/s41567-018-0214-9.

[85] M. Joppien, ' R Karnbach, T. Moiler, and H. Synchrotronstrahlungslabor, "Electronic Excitations in Liquid Helium: The Evolution from Small Clusters to Large Droplets," 1993.

[86] Y. Ovcharenko *et al.*, "Autoionization dynamics of helium nanodroplets resonantly excited by intense XUV laser pulses," *New Journal of Physics*, vol. 22, no. 8, Aug. 2020, doi: 10.1088/1367-2630/ab9554.

[87] A. C. Laforge *et al.*, "Collective autoionization in multiply-excited systems: A novel ionization process observed in Helium Nanodroplets," *Scientific Reports*, vol. 4, Jan. 2014, doi: 10.1038/srep03621.

[88] A. C. Laforge *et al.*, “Ultrafast Resonant Interatomic Coulombic Decay Induced by Quantum Fluid Dynamics,” *Physical Review X*, vol. 11, no. 2, Apr. 2021, doi: 10.1103/PhysRevX.11.021011.

[89] T. Jahnke, “Interatomic and intermolecular Coulombic decay: The coming of age story,” *Journal of Physics B: Atomic, Molecular and Optical Physics*, vol. 48, no. 8. Institute of Physics Publishing, Apr. 28, 2015. doi: 10.1088/0953-4075/48/8/082001.

[90] T. Jahnke *et al.*, “Interatomic and intermolecular coulombic decay,” *Chemical Reviews*, vol. 120, no. 20. American Chemical Society, pp. 11295–11369, Oct. 28, 2020. doi: 10.1021/acs.chemrev.0c00106.

[91] V. Averbukh, I. B. Müller, and L. S. Cederbaum, “Mechanism of interatomic coulombic decay in clusters,” *Physical Review Letters*, vol. 93, no. 26 I, Dec. 2004, doi: 10.1103/PhysRevLett.93.263002.

[92] S. Marburger, O. Kugeler, U. Hergenhahn, and T. Möller, “Experimental Evidence for Interatomic Coulombic Decay in Ne Clusters,” *Physical Review Letters*, vol. 90, no. 20, p. 4, 2003, doi: 10.1103/PhysRevLett.90.203401.

[93] R. J. Donnelly and C. F. Barenghi, “The observed properties of liquid helium at the saturated vapor pressure,” *Journal of Physical and Chemical Reference Data*, vol. 27, no. 6, pp. 1217–1274, 1998, doi: 10.1063/1.556028.

[94] C. Bostedt *et al.*, “Ultrafast x-ray scattering of xenon nanoparticles: Imaging transient states of matter,” *Physical Review Letters*, vol. 108, no. 093401, p. 093401, 2012, doi: 10.1103/PhysRevLett.108.093401.

[95] M. M. Seibert *et al.*, “Single mimivirus particles intercepted and imaged with an X-ray laser,” *Nature*, vol. 470, pp. 78–81, 2011, doi: 10.1038/nature09748.

[96] P. J. Ho *et al.*, “The role of transient resonances for ultra-fast imaging of single sucrose nanoclusters,” *Nature Communications*, vol. 11, p. 167, 2020, doi: 10.1038/s41467-019-13905-9.

[97] D. Rupp *et al.*, “Imaging plasma formation in isolated nanoparticles with ultrafast resonant scattering,” *Structural Dynamics*, vol. 7, no. 034303, p. 034303, 2020, doi: 10.1063/4.0000006.

[98] U. Saalmann and J. M. Rost, “Ionization of Clusters in Strong X-Ray Laser Pulses,” *Physical Review Letters*, vol. 89, no. 14, p. 143401, 2002, doi: 10.1103/PhysRevLett.89.143401.

[99] T. Ditmire, T. Donnelly, A. Rubenchik, R. Falcone, and M. Perry, “Interaction of intense laser pulses with atomic clusters,” *Physical Review A*, vol. 53, no. 5, pp. 3379–3402, 1996, doi: 10.1103/PhysRevA.53.3379.

[100] S. Schorb *et al.*, "Size-dependent ultrafast ionization dynamics of nanoscale samples in intense femtosecond x-ray free-electron-laser pulses," *Physical Review Letters*, vol. 108, no. 233401, p. 233401, 2012, doi: 10.1103/PhysRevLett.108.233401.

[101] M. Lezius *et al.*, "Explosion Dynamics of Rare Gas Clusters in Strong Laser Fields," *Physical Review Letters*, vol. 80, no. 2, pp. 261–264, 1998.

[102] M. Arbeiter and T. Fennel, "Ionization heating in rare-gas clusters under intense XUV laser pulses," *Physical Review A*, vol. 82, no. 013201, p. 013201, 2010, doi: 10.1103/PhysRevA.82.013201.

[103] U. Saalmann, C. Siedschlag, and J. M. Rost, "Mechanisms of cluster ionization in strong laser pulses," *Journal of Physics B: Atomic, Molecular and Optical Physics*, vol. 39, no. 4, pp. R39–R77, 2006, doi: 10.1088/0953-4075/39/4/R01.

[104] U. Saalmann, "Cluster nanoplasmas in strong FLASH pulses : formation, excitation and relaxation," *Journal of Physics B: Atomic, Molecular and Optical Physics*, vol. 43, no. 194012, p. 194012, 2010, doi: 10.1088/0953-4075/43/19/194012.

[105] T. Ditmire *et al.*, "High energy Ion explosion of atomic clusters: Transition from molecular to plasma behavior," *Physical Review Letters*, vol. 78, no. 14, pp. 2732–2735, 1997, doi: 10.1103/PhysRevLett.78.2732.

[106] T. Fennel, K. H. Meiwes-Broer, J. Tiggesbäumker, P. G. Reinhard, P. M. Dinh, and E. Suraud, "Laser-driven nonlinear cluster dynamics," *Reviews of Modern Physics*, vol. 82, no. 2, pp. 1793–1842, 2010, doi: 10.1103/RevModPhys.82.1793.

[107] T. Ditmire *et al.*, "High-energy ions produced in explosions of superheated atomic clusters," *Nature*, vol. 386, pp. 54–56, 1997, doi: 10.1038/255243a0.

[108] D. Rupp *et al.*, "Recombination-Enhanced Surface Expansion of Clusters in Intense Soft X-Ray Laser Pulses," *Physical Review Letters*, vol. 117, no. 153401, p. 153401, 2016, doi: 10.1103/PhysRevLett.117.153401.

[109] H. Thomas *et al.*, "Explosions of xenon clusters in ultraintense femtosecond X-ray pulses from the LCLS free electron laser," *Physical Review Letters*, vol. 108, no. 133401, p. 133401, 2012, doi: 10.1103/PhysRevLett.108.133401.

[110] M. Hoener *et al.*, "Charge recombination in soft x-ray laser produced nanoplasmas," *Journal of Physics B: Atomic, Molecular and Optical Physics*, vol. 41, p. 181001, 2008, doi: 10.1088/0953-4075/41/18/181001.

[111] H. Thomas *et al.*, "Shell explosion and core expansion of xenon clusters irradiated with intense femtosecond soft x-ray pulses," *Journal of Physics B: Atomic, Molecular and Optical Physics*, vol. 42, no. 134018, p. 134018, 2009, doi: 10.1088/0953-4075/42/13/134018.

[112] R. P. Madden and K. Codling, “New autoionizing atomic energy levels in He, Ne, and Ar,” *Physical Review Letters*, vol. 10, no. 12, pp. 516–518, 1963, doi: 10.1103/PhysRevLett.10.516.

[113] J. A. R. Samson, W. C. Stolte, X. H. Z, J. N. Cutler, Y. Lu, and R. J. Bartlett, “Double photoionization of helium,” *Physical Review A*, vol. 57, no. 3, pp. 1906–1911, 1998, doi: 10.1103/PhysRevA.1.586.

[114] Maximilian Jakob Bucher, “Ultrafast Dynamics of Nanoparticles in Highly Intense X-Ray Pulses,” 2017.

[115] P. Reinhard and E. Suraud, “B Gross properties of atoms and solids,” in *Introduction to Cluster Dynamics*, 2004, pp. 259–266.

[116] C. Bernando *et al.*, “Shapes of rotating superfluid helium nanodroplets,” *Physical Review B*, vol. 95, no. 064510, p. 064510, 2017, doi: 10.1103/PhysRevB.95.064510.

[117] L. B. Henke, E. M. Gullikson, and J. C. Davis, “X-ray interactions: photoabsorption, scattering, transmission, and reflection at E=50-30000 eV, Z=1-92,” *Atomic Data and Nuclear Data Tables*, vol. 54, no. 2, pp. 181–342, 1993.

[118] B. Erk, K. Hoffmann, N. Kandadai, A. Helal, J. Keto, and T. Ditmire, “Observation of shells in coulomb explosions of rare-gas clusters,” *Physical Review A - Atomic, Molecular, and Optical Physics*, vol. 83, no. 043201, p. 043201, 2011, doi: 10.1103/PhysRevA.83.043201.

[119] B. F. Murphy, K. Hoffmann, A. Belolipetski, J. Keto, and T. Ditmire, “Explosion of xenon clusters driven by intense femtosecond pulses of extreme ultraviolet light,” *Physical Review Letters*, vol. 101, no. 203401, p. 203401, 2008, doi: 10.1103/PhysRevLett.101.203401.

[120] K. Ishikawa and T. Blenski, “Explosion dynamics of rare-gas clusters in an intense laser field,” *Physical Review A - Atomic, Molecular, and Optical Physics*, vol. 62, no. 063204, p. 063204, 2000, doi: 10.1103/PhysRevA.62.063204.

[121] C. Bostedt *et al.*, “Fast electrons from multi-electron dynamics in xenon clusters induced by inner-shell ionization,” *New Journal of Physics*, vol. 12, Aug. 2010, doi: 10.1088/1367-2630/12/8/083004.

[122] M. Grech *et al.*, “Coulomb explosion of uniformly charged spheroids,” *Physical Review E - Statistical, Nonlinear, and Soft Matter Physics*, vol. 84, p. 056404, 2011, doi: 10.1103/PhysRevE.84.056404.

[123] I. v. Katardjiev, S. Berg, C. Nender, and V. Miteva, “On the impact parameter probability distribution in atomic collisions for Monte Carlo simulations,” *Nuclear Inst. and Methods in Physics Research, B*, vol. 72, pp. 28–32, 1992, doi: 10.1016/0168-583X(92)95276-W.

[124] C. C. Wang, O. Kornilov, O. Gessner, J. H. Kim, D. S. Peterka, and D. M. Neumark, "Photoelectron imaging of helium droplets doped with Xe and Kr atoms," *Journal of Physical Chemistry A*, vol. 112, no. 39, pp. 9356–9365, 2008, doi: 10.1021/jp802332f.